

---

**Title 40 CFR Part 191  
Subparts B and C  
Compliance Recertification Application 2014  
for the  
Waste Isolation Pilot Plant**

**Appendix TFIELD-2014  
Transmissivity Fields**



**United States Department of Energy  
Waste Isolation Pilot Plant**

**Carlsbad Field Office  
Carlsbad, New Mexico**

---

**Compliance Recertification Application 2014**  
**Appendix TFIELD-2014**

## Table of Contents

TFIELD-1.0 Overview of the T-field Development, Calibration, and Mining Modification Process .....	1
TFIELD-2.0 Geologic Data .....	4
TFIELD-2.1 Culebra Hydrogeologic Setting .....	4
TFIELD-2.2 Refinement of Geologic Boundaries .....	5
TFIELD-2.2.1 Rustler Halite Margins .....	6
TFIELD-2.2.2 Salado Dissolution .....	11
TFIELD-2.3 Confinement and Recharge in the Culebra .....	12
TFIELD-2.3.1 Surface Drainage Basins .....	12
TFIELD-2.3.2 Culebra Confinement .....	14
TFIELD-2.3.3 Gypsum Cements in the Culebra .....	16
TFIELD-3.0 T-Field Conceptual Model Refinement .....	20
TFIELD-3.1 Model Domain .....	21
TFIELD-3.2 Overburden Thickness .....	21
TFIELD-3.3 Fracture Interconnection .....	23
TFIELD-3.4 Salado Dissolution .....	25
TFIELD-3.5 Rustler Halite Margins .....	25
TFIELD-3.6 Transmissivity Regression Model .....	26
TFIELD-3.7 Culebra Conceptual Model Peer Review .....	27
TFIELD-4.0 Base T-Field Construction .....	28
TFIELD-4.1 Step 1 – Linear Regression Analysis .....	28
TFIELD-4.2 Step 2 – Creation of Soft Data .....	29
TFIELD-4.2.1 Halite Bounding .....	31
TFIELD-4.2.2 Gypsum Cements .....	31
TFIELD-4.2.3 Diffusivity and Hydraulic Connections .....	34
TFIELD-4.2.4 Combined Soft Data .....	35
TFIELD-4.3 Step 3 – Indicator Variography .....	36
TFIELD-4.4 Step 4 – Conditional Indicator Simulation .....	37
TFIELD-4.5 Step 5 – Construction of Transmissivity Fields .....	40
TFIELD-5.0 T-Field Calibration .....	45
TFIELD-5.1 Model Calibration Targets .....	48
TFIELD-5.2 Step 1 – Calibration Setup and Configuration .....	50
TFIELD-5.2.1 Creation of Parameter Zones .....	50
TFIELD-5.2.2 Selection of Pilot Point Locations .....	57
TFIELD-5.2.3 Transmissivity-Specific Pilot Point Settings .....	57
TFIELD-5.2.4 Anisotropy-Specific Pilot Point Settings .....	59
TFIELD-5.2.5 Storativity-Specific Pilot Point Settings .....	59
TFIELD-5.2.6 Recharge-Specific Pilot Point Settings .....	61
TFIELD-5.2.7 Selection of Initial Values .....	62
TFIELD-5.2.8 Creation of Transmissivity Fields .....	64
TFIELD-5.2.9 Observations and Residuals .....	65
TFIELD-5.2.10 MODFLOW Numerical Model .....	65
TFIELD-5.3 Step 2 – Calibration Process .....	66
TFIELD-5.3.1 PEST Calibration Process .....	66
TFIELD-5.3.2 Calibrated Correction of Steady-State Head Values .....	68

TFIELD-5.3.3 Evaluation of Impact of Multiple Calibration Processes .....	70
TFIELD-5.3.4 Selection of Best-Calibrated Fields.....	70
TFIELD-5.4 Step 3 – Post-Calibration Analysis .....	72
TFIELD-5.4.1 Statistical Analysis of Resulting <i>T</i> , <i>A</i> , and <i>S</i> Fields .....	72
TFIELD-5.4.2 Forward Model Results Using the Calibrated Fields .....	82
TFIELD-6.0 Culebra T-Field Mining Modifications.....	85
TFIELD-6.1 Overview.....	85
TFIELD-6.2 Model Domain, Boundary, and Initial Conditions .....	86
TFIELD-6.2.1 Boundary and Initial Conditions .....	86
TFIELD-6.2.2 Determination of Potential Mining Areas .....	89
TFIELD-6.2.3 Use of Mining Zones in Forward Simulations .....	92
TFIELD-6.2.4 Particle-Tracking Simulations.....	92
TFIELD-6.3 Particle-Tracking Results.....	93
TFIELD-6.3.1 Particle Travel Times .....	93
TFIELD-6.3.2 Flow Directions .....	95
TFIELD-6.3.3 Particle Speeds .....	102
TFIELD-6.3.4 Particle-Tracking Discussion .....	105
TFIELD-6.4 Mining Modification Summary .....	107
TFIELD-7.0 Summary .....	109
TFIELD-8.0 References.....	110

## List of Figures

Figure TFIELD 2-1. Generalized Stratigraphy Near the WIPP.....	5
Figure TFIELD 2-2. WIPP Culebra Dolomite Conceptual Model. Culebra <i>T</i> decreases to the east (increasing overburden and halite) and increases to the west (fracturing due to underlying Salado dissolution). Halite appears both above (H-3) and below (H-2) the Culebra in the east. Primary groundwater flow direction through the Culebra is south. .....	6
Figure TFIELD 2-3. Rustler Formation Stratigraphic Nomenclature .....	7
Figure TFIELD 2-4. M-1/H-1 Halite Margin In the Lower Los Medaños Member .....	9
Figure TFIELD 2-5. M-2/H-2 Halite Margin In the Upper Los Medaños Member.....	9
Figure TFIELD 2-6. M-3/H-3 Halite Margin In the Tamarisk Member .....	9
Figure TFIELD 2-7. M-4/H-4 Halite Margin In the Forty-niner Member .....	9
Figure TFIELD 2-8. Salado Dissolution Margin and Rustler Mudstone/Halite (M/H) Margins. WIPP Culebra wells with high or low transmissivity ( <i>T</i> ) are indicated. WIPP Culebra model extents indicated with large black rectangle. Wells mentioned in text are labeled using larger font. ....	10
Figure TFIELD 2-9. Top Elevation (m Above Mean Sea Level (AMSL)) of the Culebra. WIPP LWB indicated with blue dashed line. Township (T) and Range (R) corners indicated with crosses. ....	11
Figure TFIELD 2-10. Closed Drainage Sub-basins Identified in Southeastern Nash Draw. White areas are either outside Nash Draw or the study area. ....	14
Figure TFIELD 2-11. Culebra Confinement Map for Southern Nash Draw Study Area. White areas are outside the Nash Draw geologic study area. Zones are shown over the entire model area in Figure TFIELD 5-3.....	16
Figure TFIELD 2-12. Areas Where No Gypsum Has Been Found in Core Samples, Corresponding to a Greater Likelihood of Having Higher Culebra <i>T</i> Values.....	18
Figure TFIELD 2-13. Areas Where Wells Have Either No or Low Gypsum Content. The areas not shaded are likely to have high gypsum content and lower <i>T</i> .....	19
Figure TFIELD 3-1. Culebra Overburden Thickness Contours (m). Square is the WIPP LWB; irregular black outline west of WIPP is Nash Draw. ....	22
Figure TFIELD 3-2. Conceptual Model Zones With Indicator Values and Zone Numbers (Equation TFIELD 3.2). Zones 3 and 4 are distributed randomly between the Salado dissolution margin and westernmost M2/H3 or M3/H3 Rustler halite margins. ....	24
Figure TFIELD 3-3. Histogram of $\log_{10}$ Culebra Transmissivity ( <i>T</i> ) Estimates at WIPP Wells from Single-well Tests .....	25
Figure TFIELD 4-1. Regression Lines for Low- <i>T</i> Wells (Blue), High- <i>T</i> and Non-dissolution Wells (Green), and Wells Within the Salado Dissolution Zone (Red). Open diamonds are wells new to	

the CRA-2009 PABC regression analysis (i.e., not included in CRA-2004 PABC).....	29
Figure TFIELD 4-2. Diffusivity Values Calculated Between Wells From Pumping Test Data. Connections where $\log_{10} D > 0.2$ are included as conditioning data with $P_{\text{low}} = 0.25$ .....	33
Figure TFIELD 4-3. Soft Data Points (Open Symbols) Generated During Step 2. Hard data points (filled symbols) are located at wells with single-well estimates of $T$ . The black square is the WIPP LWB. ....	34
Figure TFIELD 4-4. Experimental Variogram (Dots) and Spherical Model (Line) for Indicator Values. $x$ -axis is lag distance [meters], $y$ -axis is the unitless indicator; numbers by dots indicate the number of pairs represented at each lag. ....	37
Figure TFIELD 4-5. Sample Indicator Field for Realization r123. 1 indicates low $T$ and 0 indicates high $T$ .....	38
Figure TFIELD 4-6. Average Indicator Values Across All 1000 Base Realizations. 1 indicates low $T$ and 0 indicates high $T$ .....	39
Figure TFIELD 4-7. Standard Deviation of Indicator Values Across All 1000 Base Realizations .....	40
Figure TFIELD 4-8. Sample $\log_{10} T$ ( $\text{m}^2/\text{s}$ ) Base Field Realization r123 .....	42
Figure TFIELD 4-9. Mean $\log_{10} T$ ( $\text{m}^2/\text{s}$ ) Values Across All 1000 Base Realizations .....	43
Figure TFIELD 4-10. Normalized Standard Deviation of $\log_{10} T$ ( $\text{m}^2/\text{s}$ ) Values Across All 1000 Base Realizations .....	44
Figure TFIELD 5-1. Complete Calibration Process for a Single Realization .....	47
Figure TFIELD 5-2. Transmissivity Zone Map for a Single Realization. Zones 0 and 1 are the stochastic zones created in Hart et al. (2008); Zone 2 is the high- $T$ Salado dissolution area; Zone 3 is the very low- $T$ halite-bounded area; Zone 4 is the northwestern inactive area.....	52
Figure TFIELD 5-3. Storativity Zones. Zone 0 is confined; Zone 1 is a transition between confined and unconfined; Zone 2 is unconfined; Zone 3 is confined and uncalibrated from the initial confined value; Zone 4 is inactive (no flow).....	54
Figure TFIELD 5-4. Zone 1, the Zone of Non-zero Recharge. Zone 1 is the linear feature directed southeast from the center of the west edge of the model domain. The remaining model area has no recharge.....	55
Figure TFIELD 5-5. Flow Zones. The fixed-head zone is green; the no-flow zone is salmon; the white area is normal flow. The fixed-head zone includes one cell along the northern, southern, and western boundaries.....	56
Figure TFIELD 5-6. Transmissivity Pilot Point Locations. Blue points are fixed values and red points are variable parameters. Zones correspond to a single realization.....	58

Figure TFIELD 5-7. Anisotropy Pilot Point Locations. All anisotropy pilot points were variable parameters. Zones correspond to a single realization. ....	60
Figure TFIELD 5-8. Storativity Pilot Point Locations. Only pilot points along lines between wells in transient pumping tests and points in the unconfined zones (zones 1 and 2) were variable (red dots); the remaining pilot points were fixed (blue dots). ....	61
Figure TFIELD 5-9. Recharge Pilot Point Locations. The pilot point along the model domain boundary was fixed, while the other three points were variable.....	62
Figure TFIELD 5-10. Initial Head Values for Use in MODFLOW Steady-state Solution. Brick red head values were fixed at the ground surface elevation (>1,000 m AMSL).....	64
Figure TFIELD 5-11. Flow Chart Showing the Forward Model Used In the Model Calibration. $T$ , $A$ , $S$ , and $R$ are parameter fields. $H$ represents the steady-state flow solution. $DD_1-DD_9$ represent transient drawdown computed for the 9 individual pumping tests from 9 separate forward simulations. ....	66
Figure TFIELD 5-12. Flowchart Illustrating the PEST Calibration Process.....	68
Figure TFIELD 5-13. Recalibration Boundary Shown in Red To the Northeast of the WIPP Site. Recalibration boundary limits are UTM $X$ and $Y$ NAD27 Zone 13 (m). ....	69
Figure TFIELD 5-14. Selection of Best Fields From All Fields by Weighted Sum of Steady-state Errors and Sum of Average Pumping Test Average Errors .....	72
Figure TFIELD 5-15. Mean Effective Transmissivity ( $T_e$ ) for Zones 0-2 Across the 100 Final Selected Fields. All 100 calibrated $T_e$ fields are plotted in Appendix TFIELD Attachment A.....	74
Figure TFIELD 5-16. Standard Deviation of Effective Transmissivity ( $T_e$ ) for All Zones Across the 100 Final Selected Fields. All 100 calibrated $T_e$ fields are plotted in Appendix TFIELD Attachment A. ....	75
Figure TFIELD 5-17. High- $T$ Zone Membership Calculated for the Base 100 $T$ Fields Corresponding to the 100 Selected Calibrated Fields .....	76
Figure TFIELD 5-18. High- $T$ Zone Membership Calculated for the Calibrated $T$ Values.....	77
Figure TFIELD 5-19. Number of $T$ Fields Where Low $T$ Became High $T$ Through PEST Calibration.....	78
Figure TFIELD 5-20. Number of $T$ Fields Where High $T$ Became Low $T$ Through PEST Calibration.....	79
Figure TFIELD 5-21. Mean Storativity Values Across the 100 Final Calibrated Fields. Individual $S$ fields are plotted in Appendix TFIELD Attachment A. ....	80
Figure TFIELD 5-22. Standard Deviation of Storativity Values Across the 100 Final Calibrated Fields. Red oval shows P-14 to WIPP-25	

area of influence. Individual <i>S</i> fields are plotted in Appendix TFIELD Attachment A.....	81
Figure TFIELD 5-23. Recharge as Viewed Through Columns From the South. The initial value was set at $10^{-3.5}$ m/year. The sharp dropoff to the west is the transition to the single fixed-recharge point of $10^{-11.5}$ m/year (interpreted as zero by REAL2MOD).....	82
Figure TFIELD 5-24. Results for 42 Total Steady-state Head Measurements for the 100 Selected Fields (No SNL-6 or SNL-15). Observed heads are red $\times$ 's along the diagonal line. ....	83
Figure TFIELD 5-25. Histogram of Steady-state Head Errors for the 100 Selected Fields (No SNL-6 or SNL-15). Red dashed line is the $\pm 3\sigma$ section of the measurement error PDF. The slight skew to right is an artifact of the binning. ....	84
Figure TFIELD 6-1. Comparison of Minable Potash Area to the Flow and Transport Modeling Domains. Green hatches represent minable potash area (Cranston 2009).....	88
Figure TFIELD 6-2. Stencil Used to Model Cells Affected by Mining-related Subsidence (Blue Cells with A) Due to Mining in Red "M" Cell, Using $45^\circ$ Angle of Draw .....	89
Figure TFIELD 6-3. Definitions of Mining-affected Areas in Full-mining Scenario Between Current and Previous Models. Base image is Figure 3.2 from Lowry and Kanney (2005). CRA-2009 PABC mining area (red stippled area) and model domain (green line) definitions are current definitions used in CRA-2014. ....	90
Figure TFIELD 6-4. Definitions of Partial-mining-affected Areas Between Current and Previous Applications. Base image is Figure 3.3 from Lowry and Kanney (2005). CRA-2009 PABC mining area (red stippled area) and model domain (green line) definitions are current definitions used in CRA-2014.....	91
Figure TFIELD 6-5. Comparison of Minable Potash Distribution Inside the WIPP LWB for CRA-2004 PABC (Dark Gray) and CRA-2009 PABC (Translucent Green). The WIPP repository plan is shown for comparison, from Figure 3.6 of Lowry and Kanney (2005).....	92
Figure TFIELD 6-6. CDF of Advective Particle Travel Times From the Center of the WIPP Waste Panels To the WIPP LWB for Full, Partial, and Non-mining Scenarios .....	94
Figure TFIELD 6-7. Comparison of Advective Particle Travel Time CDFs for Non-mining Scenarios of CRA-2009 PABC, CRA-2004 PABC, and CCA. Travel times are from the center of the WIPP waste panels to the WIPP LWB.....	95
Figure TFIELD 6-8. 100 Particle Tracks for Non-mining Scenario. Black box is the WIPP LWB, green circles are Culebra monitoring well locations.....	96

Figure TFIELD 6-9. 100 Particle Tracks Each for R1 Full and Partial Mining Scenarios. Small magenta squares and blue crosses indicate centers of MODFLOW cells located within potash and mining-affected areas, respectively; thin black line is minable potash.....	97
Figure TFIELD 6-10.100 Particle Tracks Each for R2 Full- and Partial-mining Scenarios. Small magenta squares and blue crosses indicate centers of MODFLOW cells located within potash and mining-affected areas, respectively; thin black line is minable potash.....	98
Figure TFIELD 6-11.100 Particle Tracks Each for R3 Full- and Partial-mining Scenarios. Small magenta squares and blue crosses indicate centers of MODFLOW cells located within potash and mining-affected areas, respectively; thin black line is minable potash.....	99
Figure TFIELD 6-12.Histograms of Particle $x$ -coordinates at Exit Point From LWB. Full- and partial-mining include all three replicates (note different vertical scales between plots; no mining contains 100 particles while mining scenarios each include 300 particles). .....	100
Figure TFIELD 6-13.Particle Counts in Each Cell Across All 100 Selected Realizations for Non-mining Scenario .....	101
Figure TFIELD 6-14.Magnitude of Darcy Flux for a Single Realization (r440) for No, Partial, and Full-mining Scenarios Using Cell-based Coordinates. LWB (black) and SECOTP2D transport model domains (red) shown for reference.....	102
Figure TFIELD 6-15.Particle Speeds for Non-mining Scenario Computed from DTRKMF Results. Open symbols are Culebra well locations.....	104
Figure TFIELD 6-16.Particle Speeds for R1, Computed From DTRKMF Results. Open symbols are Culebra well locations.....	104
Figure TFIELD 6-17.Particle Speeds for R2, Computed From DTRKMF Results. Open symbols are Culebra well locations.....	105
Figure TFIELD 6-18.Particle Speeds for R3, Computed from DTRKMF Results. Open symbols are Culebra well locations.....	105
Figure TFIELD 6-19.Correlation of Mining Factor and Travel Time to the WIPP LWB for Full-mining Scenario (All Replicates).....	106
Figure TFIELD 6-20.Correlation of Mining Factor and Travel Time to the WIPP LWB for Partial-mining Scenario (All Replicates).....	107

## List of Tables

Table TFIELD 4-1. $\beta$ -values for Regression Equation TFIELD 4.1 .....	29
Table TFIELD 4-2. Listing of Coordinates, Culebra Depth, and $\log_{10} T$ Estimates from Single-well Tests (Hard Data) Used in Regression Model (Equation TFIELD 4.1).....	30
Table TFIELD 4-3. Variogram Parameters for Isotropic Fit to Indicator Data Variogram. Omnidirectional variogram calculated with a lag spacing of 500 m. ....	36
Table TFIELD 4-4. Correlation of $\beta$ and $I$ Values from Equation TFIELD 4.1 to $a$ and $b$ Values in Equation TFIELD 4.3 .....	41
Table TFIELD 5-1. Freshwater Head Observations Used as Steady-state Calibration Targets .....	49
Table TFIELD 5-2. Summary of Transient Observations Used as Calibration Targets.....	50
Table TFIELD 5-3. Initial Values of Parameters at Pilot Points .....	59
Table TFIELD 5-4. Parameters for $T$ Model Variogram, Fitted to Transmissivity Data Using an Omnidirectional Variogram with Lag Spacing of 1,500 m.....	65
Table TFIELD 5-5. Summary of Statistics Regarding Average Steady-state and Transient Errors Across Three Calibration Groups.....	70
Table TFIELD 5-6. Cutoff Values for Final Field Selection.....	71
Table TFIELD 5-7. Final Selected Field Identifiers .....	71
Table TFIELD 5-8. Bulk $\log_{10} T_e$ Values Comparison .....	73
Table TFIELD 6-1. Particle-tracking Travel-time Statistics from Center of the WIPP Panels to the WIPP LWB (Years). Global statistics for full and partial mining include 300 realizations, while no mining only includes 100 realizations.....	94

### **Acronyms and Abbreviations**

<i>A</i>	transmissivity anisotropy [dimensionless]
AMSL	above mean sea level
AP	analysis plan
BLM	Bureau of Land Management
CB	Cabin Baby
CCA	Compliance Certification Application
CDF	cumulative distribution function
CFR	Code of Federal Regulations
CRA	Compliance Recertification Application
<i>D</i>	diffusivity [ $\text{m}^2/\text{s}$ ]
DOE	U.S. Department of Energy
EPA	U.S. Environmental Protection Agency
km	kilometer
LWB	Land Withdrawal Boundary
m	meter
$\text{m}^2$	square meters
M/H	mudstone/halite margin
$\text{m}^2/\text{s}$	square meters per second
$\text{m}^3/\text{s}$	cubic meters per second
$\text{m}/\text{yr}$	meters per year
PA	performance assessment
PABC	performance assessment baseline calculation
<i>R</i>	recharge [ $\text{m}/\text{s}$ ]
RMSE	root mean squared error
<i>S</i>	storativity [dimensionless]
SNL	Sandia National Laboratories
SSE	sum of squared errors
SVD	singular value decomposition
<i>T</i>	transmissivity [ $\text{m}^2/\text{s}$ ]
USGS	U.S. Geological Survey
UTM	Universal Transverse Mercator map projection

WIPP

Waste Isolation Pilot Plant

## 1 **TFIELD-1.0 Overview of the T-field Development, Calibration, and** 2 **Mining Modification Process**

3 Modeling the transport of radionuclides through the Culebra Dolomite Member of the Rustler  
4 Formation (hereafter referred to as the Culebra) is one component of the performance assessment  
5 (PA) performed for the U.S. Department of Energy (DOE) Waste Isolation Pilot Plant (WIPP)  
6 2014 Compliance Recertification Application (CRA). Transport modeling in PA requires flow  
7 velocity results from the Culebra groundwater flow model. This Appendix describes the process  
8 used to develop and calibrate the input parameter fields for the Culebra flow model. Calibrated  
9 model parameters are referred to broadly as "T-fields" (transmissivity fields), although more  
10 parameters than just transmissivity ( $T$ ) were calibrated as part of the CRA-2009 Performance  
11 Assessment Baseline Calculation (PABC) model (Clayton et al. 2010). This appendix describes  
12 the process followed for the CRA-2009 (PABC), which was a major change from the process  
13 followed for CRA-2004 PABC (Leigh et al. 2004), and involved a hydrology conceptual model  
14 peer review. The T-fields developed for CRA-2009 PABC were used unchanged in CRA-2014.  
15 Figures illustrating each calibrated T-field are given in Attachment A to this Appendix.

16 The work described in this Appendix was performed under two Sandia National Laboratories  
17 (SNL) analysis plans (APs): AP-114 (Beauheim 2008) and AP-144 (Kuhlman 2009). AP-114  
18 (evaluation and recalibration of Culebra transmissivity fields) dealt with the development and  
19 calibration of the T-fields (including  $T$ , storativity ( $S$ ), horizontal anisotropy ( $A$ ), and vertical  
20 recharge ( $R$ )), in addition to development of T-field acceptance criteria. AP-144 (calculation of  
21 Culebra flow and transport) dealt with the modification of T-fields for the potential future effects  
22 of potash mining for use in the PA Culebra radionuclide transport calculations. The PA Culebra  
23 radionuclide transport calculations are not described in this Appendix, which focuses on the  
24 development and modification of the T-fields.

25 West of the WIPP, Culebra  $T$  is high where the Culebra overlies areas where the Salado  
26 Formation has been removed by dissolution (mostly in Nash Draw). East of the WIPP, Culebra  $T$   
27 is low when the Culebra is bounded either above *or* below by halite in adjoining Rustler units.  
28 Further to the east, Culebra  $T$  is very low when the Culebra is bounded both above *and* below by  
29 halite in the Rustler. At the WIPP, between the high  $T$  in the west and low  $T$  in the east, Culebra  
30  $T$  is observed to change significantly over short distances and is simulated in the WIPP Culebra  
31 flow model using a random mixture (i.e., stochastic patches) of high and low  $T$  zones, consistent  
32 with geologic and hydrologic observations. The geologic data discussed in Section TFIELD-2.0  
33 are used to specify the boundaries of these Culebra conceptual model zones (Section TFIELD-  
34 3.0), which are then carried forward into the numerical implementation of the Culebra  
35 groundwater model (Section TFIELD-4.0).

36 The starting point in the T-field development process was to assemble and update information on  
37 geologic factors potentially affecting Culebra  $T$  (Section TFIELD-2.0). These factors include  
38 dissolution of the upper Salado Formation located below the Culebra, presence of gypsum  
39 cements, the thickness of overburden above the Culebra, and the spatial distribution of halite in  
40 the Rustler Formation both above and below the Culebra. Geologic information is available from  
41 hundreds of oil and gas wells and potash exploration holes in the vicinity of the WIPP site, while  
42 estimates of Culebra  $T$  are available from only 64 well locations. Details of the geologic data

1 compilation are given in Powers (Powers 2002a, Powers 2002b and Powers 2003), updated in  
2 Powers (Powers 2007a and Powers 2007b), and summarized in Section TFIELD-2.0.

3 A two-part geologically based approach was used to generate base Culebra T-fields. In the first  
4 part (Section TFIELD-3.0), a conceptual model for geologic controls (i.e., soft data) on Culebra  
5  $T$  was formalized and the hypothesized geologic controls were regressed against Culebra  $T$   
6 estimates at monitoring wells to determine linear regression coefficients. The regression includes  
7 one continuously varying function, Culebra overburden thickness, and three indicator functions  
8 that assume values of 0 or 1 depending on the occurrence of open, interconnected fractures;  
9 Salado dissolution; and the presence or absence of halite in Rustler units bounding the Culebra.

10 In the second part (Section TFIELD-4.0), a method was developed for applying the linear  
11 regression model to predict Culebra  $T$  across the WIPP model area between the sparse  
12 observations at wells. The regression model was combined with the maps of geologic factors to  
13 create 1,000 stochastically varying base Culebra T-fields. Details about the development of the  
14 regression model and the creation of the base T-fields are given in Hart et al. (Hart et al. 2008).  
15 The conceptual model embodied in these 1,000 base Culebra T-fields was subject to peer review  
16 before model calibration proceeded (Section TFIELD-3.7). The peer review panel concluded the  
17 justification and scientific rigor of the methodology for preparing base T-fields were adequate  
18 (Burgess et al. 2008). A sample of 200 out of the 1,000 created base T-fields were calibrated  
19 following the process outlined in Section TFIELD-5.0, with the 100 best calibrated T-fields  
20 eventually chosen for use in PA radionuclide transport calculations.

21 Section TFIELD-5.0 presents details on the modeling approach used to calibrate the T-fields to  
22 both steady-state heads across the model domain and transient drawdown measurements from  
23 multi-well pumping tests. Heads measured in 42 Culebra observation wells around May 2007  
24 were used to represent steady-state conditions in the Culebra, and drawdown responses in 67  
25 total observation wells (62 unique locations) across nine pumping tests were used to provide  
26 transient calibration data. See Appendix HYDRO-2014 for more information on the Culebra  
27 monitoring well network and recent trends observed in Culebra water levels. Details on the  
28 steady-state heads are described in Johnson (Johnson 2009a and Johnson 2009b), and the  
29 transient drawdown data are summarized in Hart et al. (Hart et al. 2009). Assumptions made in  
30 modeling, the definition of an initial head distribution, assignment of boundary conditions,  
31 discretization of the spatial and temporal domain, weighting of the observations, and the use of  
32 PEST (Doherty 2000) with MODFLOW-2000 to calibrate the T-fields using a pilot-point method  
33 are described in detail in Hart et al. (Hart et al. 2009) and summarized in Section TFIELD-5.0.  
34 Section TFIELD-5.3.4 addresses the development and application of acceptance criteria to select  
35 the 100 best T-fields from the 200 calibrated T-fields. Acceptance was based on a combination  
36 of objective fit to both the steady-state and transient pumping test calibration data. Section  
37 TFIELD-5.4 provides summary statistics and other information for the 100 T-fields that were  
38 judged to be acceptably calibrated. Attachment A presents  $T$ ,  $S$ , diffusivity ( $D$ ), and model-  
39 predicted flow speed for each of the chosen 100 realizations.

40 The data used in the construction (Sections TFIELD-3.0 and TFIELD-4.0) and calibration  
41 (Section TFIELD-5.0) of the T-fields were divided into three groups:

42 1. soft data only used in base T-field generation,

- 1        2. hard data used in both T-field generation and calibration, and
- 2        3. hard data only used in calibration.

3        This first group included geologic data (i.e., Salado dissolution, presence of gypsum cements in  
4        the Culebra, Culebra overburden thickness, and the locations of Rustler halite margins) and  
5        hydrologic data (i.e., pairs of pumping and observation wells interpreted to have high diffusivity  
6        from multi-well pumping tests). The soft data were included in T-field generation because they  
7        were used to define boundaries also used in the calibration phase. The second group only  
8        included estimated  $T$  from single-well pumping tests, which were used directly in indicator  
9        kriging, indirectly in the overburden regression analysis, and directly as fixed pilot points in the  
10       calibration phase. The third group only included head and drawdown observations used as  
11       calibration targets. Some of these third group data were used in other analyses to estimate  
12       diffusivity values used as soft data (first group), but the drawdown data from multi-well pumping  
13       tests only appeared directly in the calibration phase.

14       Section TFIELD-6.0 discusses modifications of the T-fields performed to account for the effects  
15       of potash mining both within and outside the WIPP land withdrawal boundary. Potentially  
16       mining-affected areas were delineated, random transmissivity multipliers were applied to the  
17       transmissivity field in those areas, and particle tracks and travel times were computed (Kuhlman  
18       2010). The flow fields produced by these mining-affected T-fields were input to the radionuclide  
19       transport model SECOTP2D used to compute both CRA-2009 PABC and CRA-2014 long-term  
20       PA releases (Appendix PA-2014). Section TFIELD-7.0 provides an executive summary of the  
21       development and modification of the Culebra T-fields.

## 1 **TFIELD-2.0 Geologic Data**

2 The work outlined in Section TFIELD-2.0 was performed as Task 1 under AP-114, Analysis  
3 Plan for Evaluation and Recalibration of Culebra Transmissivity Fields (Beauheim 2008). There  
4 were no changes to the model between CRA-2009 PABC and CRA-2014. Geologic data were  
5 updated to improve definition of geologic boundaries used to define zones as part of the process  
6 of creating new T-fields. Geologic boundaries were refined for CRA-2009 PABC using data  
7 from field investigations and newly obtained oil and gas well log data (Section TFIELD-2.2).  
8 The Salado dissolution margin bounds the high-*T* Culebra zone to the west in Nash Draw, and  
9 was only modified slightly for CRA-2009 PABC. The Rustler halite margins bound the very  
10 low-*T* Culebra zone to the east, and were modified significantly for CRA-2009 PABC. The  
11 confinement of the Culebra in the southeastern portion of Nash Draw was also investigated in  
12 AP-114 Task 1, to constrain the Culebra flow model inputs (Section TFIELD-2.3). Previous to  
13 CRA-2009 PABC, the Culebra groundwater flow model was only steady-state and did not  
14 include input parameters related to confinement or recharge. A model was developed regarding  
15 distribution of gypsum cements in the Culebra from available core data (Section TFIELD-2.3.3).

## 16 **TFIELD-2.1 Culebra Hydrogeologic Setting**

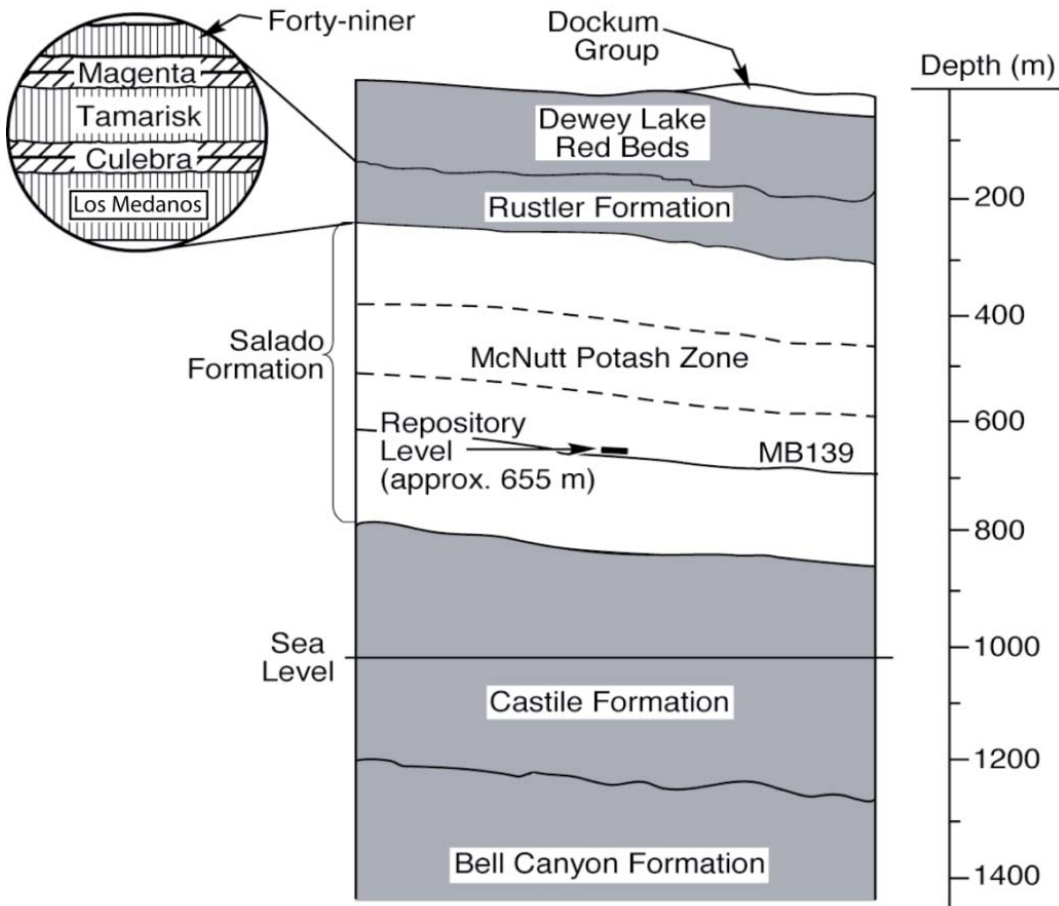
17 The Culebra Member of the Rustler Formation is considered as a potential long-term release  
18 pathway in WIPP PA because it is the most permeable laterally continuous geologic unit above  
19 the WIPP repository level (see Figure TFIELD 2-1 for general stratigraphy). Potential future  
20 human intrusion into the repository might connect the repository with the Culebra, which would  
21 then transport radionuclides to the accessible environment under natural flow conditions. The  
22 accessible environment is defined to be where the WIPP Land Withdrawal Boundary (LWB)  
23 intersects the Culebra in the subsurface.

24 The ability of the Culebra to advect groundwater and radionuclides to the accessible environment  
25 is affected by both depositional and post-depositional effects. The Culebra is believed to have  
26 been deposited quite uniformly over a wide area (the vertical thickness of the Culebra is quite  
27 uniform over lateral distances of many miles (e.g., Holt and Powers 1988)), but depositional  
28 effects include the presence of mudstone or halite layers in the Rustler Formation immediately  
29 above and below the Culebra. Post-depositional processes include dissolution of halite from the  
30 underlying Salado Formation and precipitation of vug- and pore-filling evaporates within the  
31 Culebra (see Figure TFIELD 2-2).

32 Understanding of the spatial distribution and thickness of halite in the Rustler Formation was  
33 improved for CRA-2009 PABC (compared to CRA-2009 (U.S. DOE 2009)) due to data obtained  
34 from analysis of geophysical logs from oil and gas wells. The lateral extent of Salado dissolution  
35 was modified slightly for CRA-2009 PABC, but remained largely similar to CRA-2009, with  
36 minor adjustments due to additional information for a few new WIPP wells (Powers 2007a and  
37 Powers 2007b).

38 Groundwater flow in the Culebra is generally from north to south at the WIPP site. Water levels  
39 in Culebra wells in Nash Draw (several miles to the west of the WIPP site) respond more rapidly  
40 to precipitation and behave differently than Culebra wells in the immediate vicinity of the WIPP  
41 site (Appendix HYDRO-2014, Section 7.1). Based on the north-south gradient currently

1 observed at the WIPP, particle-tracking predictions from the WIPP waste panels through the  
 2 Culebra result in flow towards the southern edge of the WIPP LWB.



TRI-6801-97-0

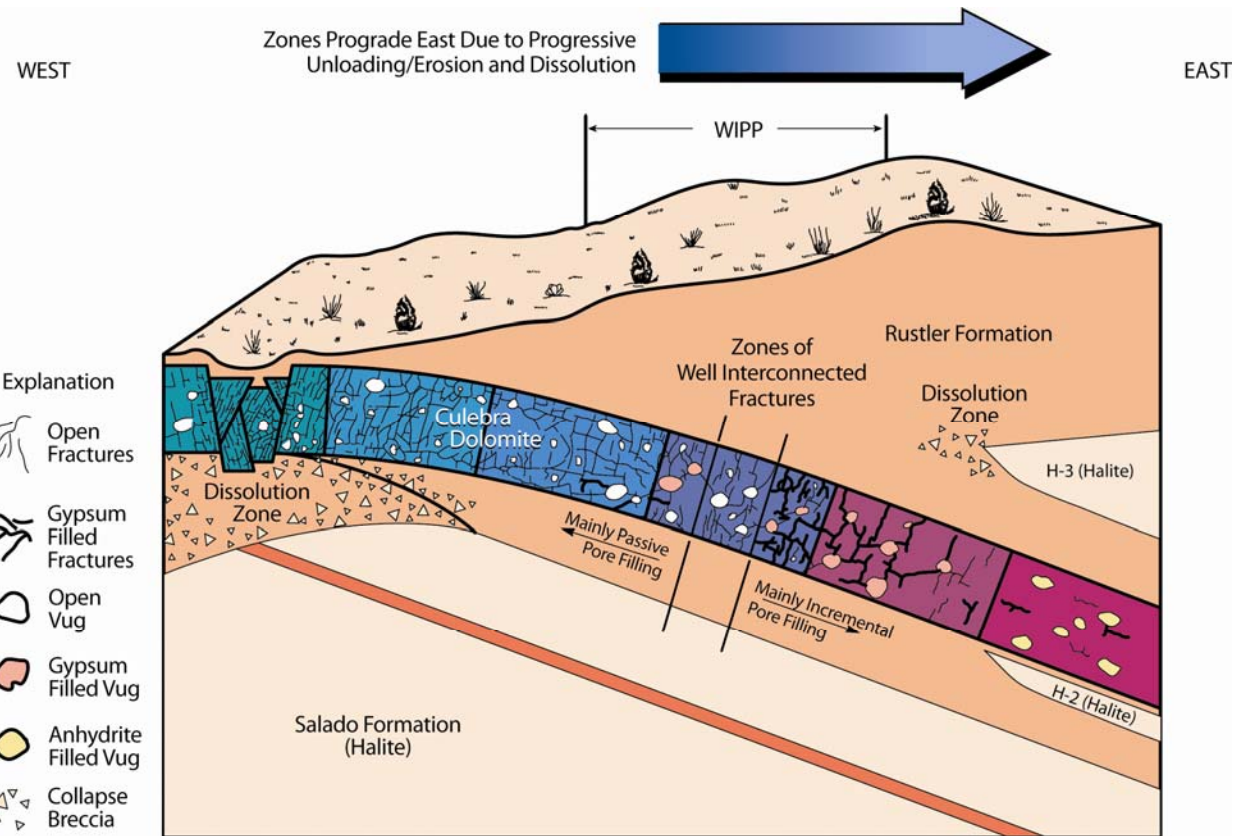
3  
 4 **Figure TFIELD 2-1. Generalized Stratigraphy Near the WIPP**

5 **TFIELD-2.2 Refinement of Geologic Boundaries**

6 The locations of the Rustler halite margins (Section TFIELD-2.2.1) and the Salado dissolution  
 7 margin (Section TFIELD-2.2.2) both affect the conceptual model of Culebra  $T$  (see Figure  
 8 TFIELD 2-1 for general relationships between the Rustler, the Salado and the WIPP repository).  
 9 These were updated as part of the CRA-2009 PABC geologic study.

10 The presence of halite in the non-dolomite members of the Rustler Formation correlates strongly  
 11 with estimates of Culebra  $T$ . Halite and anhydrite are found as pore-filling cements in the  
 12 Culebra (reducing open fractures) when halite exists in layers above the Culebra, below the  
 13 Culebra, or both (Figure TFIELD 2-2). When halite is found either above (H3) or below (H2) the  
 14 Culebra, observed Culebra  $T$  is low. When halite exists both above and below the Culebra,  
 15 observed Culebra  $T$  is extremely low.

1 North, south and west of the WIPP site, Cenozoic dissolution has affected the upper Salado  
 2 Formation. Where this dissolution has occurred, the rocks overlying the Salado, including the  
 3 Culebra, are strained (leading to larger apertures in existing fractures), fractured, collapsed, or  
 4 brecciated (e.g., Beauheim and Holt 1990). All WIPP Culebra wells within the Salado  
 5 dissolution zone have been interpreted to have high  $T$ . It is hypothesized that all regions affected  
 6 by Salado dissolution have well-interconnected fractures and therefore high  $T$ .



7  
 8 **Figure TFIELD 2-2. WIPP Culebra Dolomite Conceptual Model.** Culebra  $T$  decreases to  
 9 the east (increasing overburden and halite) and increases to the west  
 10 (fracturing due to underlying Salado dissolution). Halite appears  
 11 both above (H-3) and below (H-2) the Culebra in the east. Primary  
 12 groundwater flow direction through the Culebra is south.

### 13 **TFIELD-2.2.1 Rustler Halite Margins**

14 The Rustler Formation stratigraphic column given in Figure TFIELD 2-3 shows two types of  
 15 geologic variability. Vertical stratigraphy places older formations below younger formations at  
 16 the same location in space (e.g., the Los Medaños Member is older than the Culebra Member),  
 17 while facies change place two units of similar age at different spatial locations, due to changes in  
 18 depositional environments (e.g., Mudstone 4 (M4) and Halite 4 (H4) of the Forty-niner Member  
 19 are of the same age, but occur in different locations).

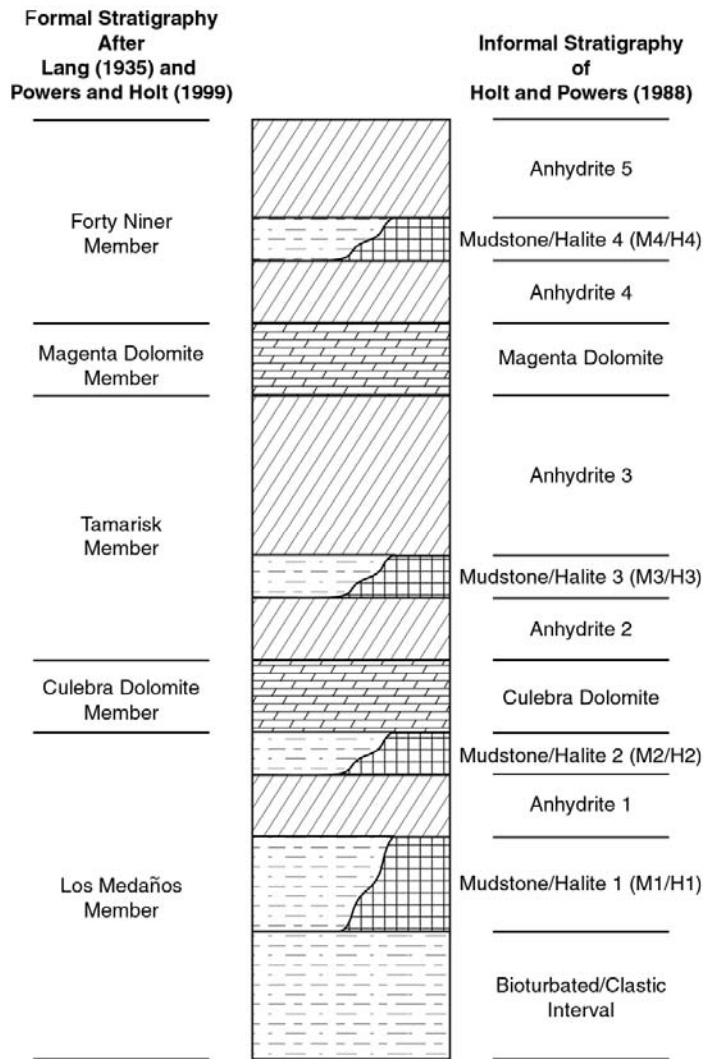


**Figure TFIELD 2-3. Rustler Formation Stratigraphic Nomenclature**

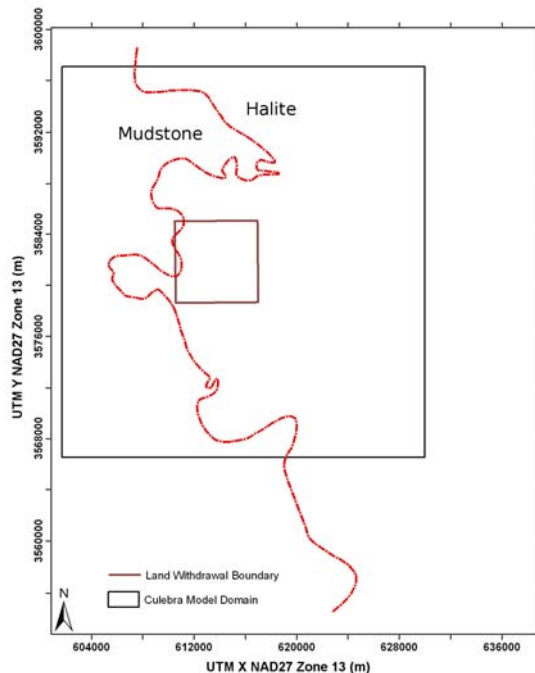
1 Powers (Powers 2002a and Powers 2002b) provided geologic data across the CRA-2004 PABC  
 2 Culebra modeling domain that included maps of halite margins within the Rustler Formation.  
 3 Those margins were largely based on work in Powers and Holt (Powers and Holt 1995),  
 4 modified by some data collected from potash drillholes, especially in the northern area of the  
 5 Culebra modeling domain. The observed distribution and thickness of halite in the Rustler is  
 6 interpreted to be the result of sedimentary structures and facies relationships controlled by  
 7 deposition, rather than the result of dissolution alone (Holt and Powers 1988; Powers and Holt  
 8 1999; Powers and Holt 2000). Before Holt and Powers (Holt and Powers 1988), many  
 9 researchers incorrectly believed a uniform thickness of Rustler halite was deposited and later  
 10 removed by dissolution in the areas near Nash Draw, leaving the observed mudstone layers as  
 11 dissolution residue. Definitive data collected during WIPP air-intake shaft geologic mapping  
 12 provided the basis for the current facies-based conceptual model used at the WIPP (Holt and  
 13 Powers 1988). Some minor zones adjacent to the depositional margins have been interpreted as  
 14 having undergone some post-depositional dissolution of halite, specifically the halite in the  
 15  
 16

1 Tamarisk Member, but the extent of this Rustler halite dissolution is relatively minor (Beauheim  
2 and Holt 1990).

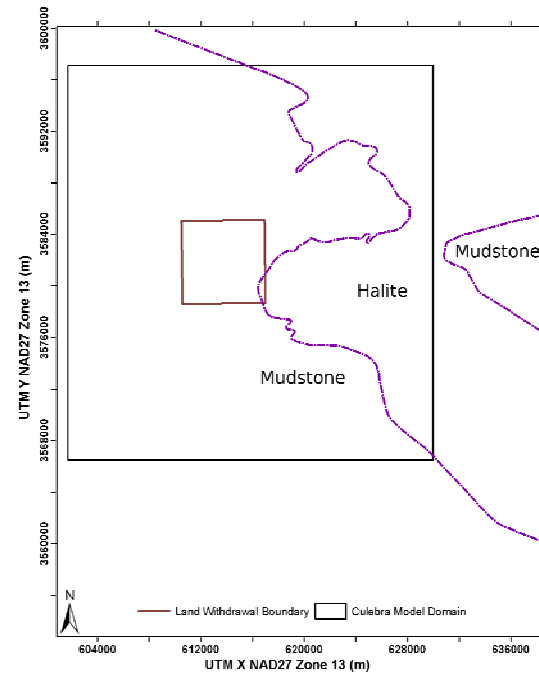
3 Significant changes to the locations of the M3/H3 and M2/H2 margins have been made for CRA-  
4 2009 in some areas since CRA-2004 (U.S. DOE 2004) as part of Task 1A of AP-114. The  
5 Rustler halite margins used since CRA-2009 PABC are shown over a wide area in Figure  
6 TFIELD 2-4 through Figure TFIELD 2-7, as defined in Powers (Powers 2007a and Powers  
7 2007b). Changes in the location of the halite margins were based mostly on newly obtained  
8 geophysical log data obtained from oil and gas exploration (both new and old wells), and a few  
9 hydrologic wells drilled by the WIPP program since 2003 (Powers 2007a).

10 Wells H-17 and H-12 (see Figure TFIELD 2-8), located where halite occurs in the Tamarisk  
11 Member (H3 interval; Figure TFIELD 2-6) but not in the Los Medaños Member (M2 interval;  
12 Figure TFIELD 2-5) of the Rustler Formation show low transmissivity. We assume high-  
13 transmissivity zones do not occur in the Culebra where H2 or H3 also occur. Margins near the  
14 WIPP remain nearly unchanged, and all modifications to the margins do not change the basic  
15 interpretation that the margins are the result of deposition and local syndepositional dissolution  
16 of halite, not regional halite dissolution from the Rustler (Holt and Powers 1988; Powers and  
17 Holt 2000; Powers et al. 2006). Core evidence from well SNL-8 shows limited brecciation of  
18 anhydrite 3 in the Tamarisk (Figure TFIELD 2-3) that is interpreted as an extension of a narrow  
19 margin along the H-3 margin where a limited amount of halite was dissolved after deposition  
20 (Powers 2009).

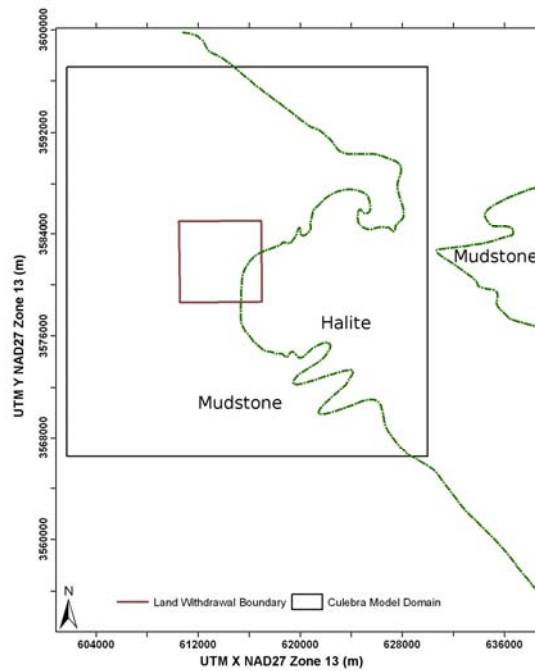
21 After refining the Rustler halite margin locations, all mudstone/halite margins now show similar  
22 gross trends (compare Figure TFIELD 2-4 through Figure TFIELD 2-7 and Figure TFIELD 2-8).  
23 Southeast of the WIPP, the margins are elongate roughly northwest to southeast. The gross  
24 trends of these margins are similar to the trend in the elevation of the top of Culebra (Figure  
25 TFIELD 2-9). As previously described (e.g., Holt and Powers 1988); Powers et al. (Powers et al.  
26 2003), this northwest-to-southeast trending anticlinal feature is called the Divide anticline.  
27 Mudstone dominates along this trend in three of the mudstone-halite units of the Rustler (i.e., all  
28 except M1/H1).



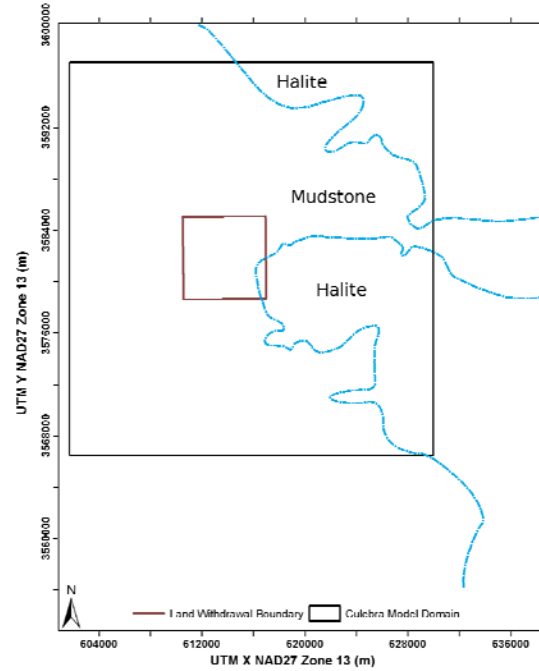
**Figure TFIELD 2-4. M-1/H-1 Halite Margin In the Lower Los Medaños Member**



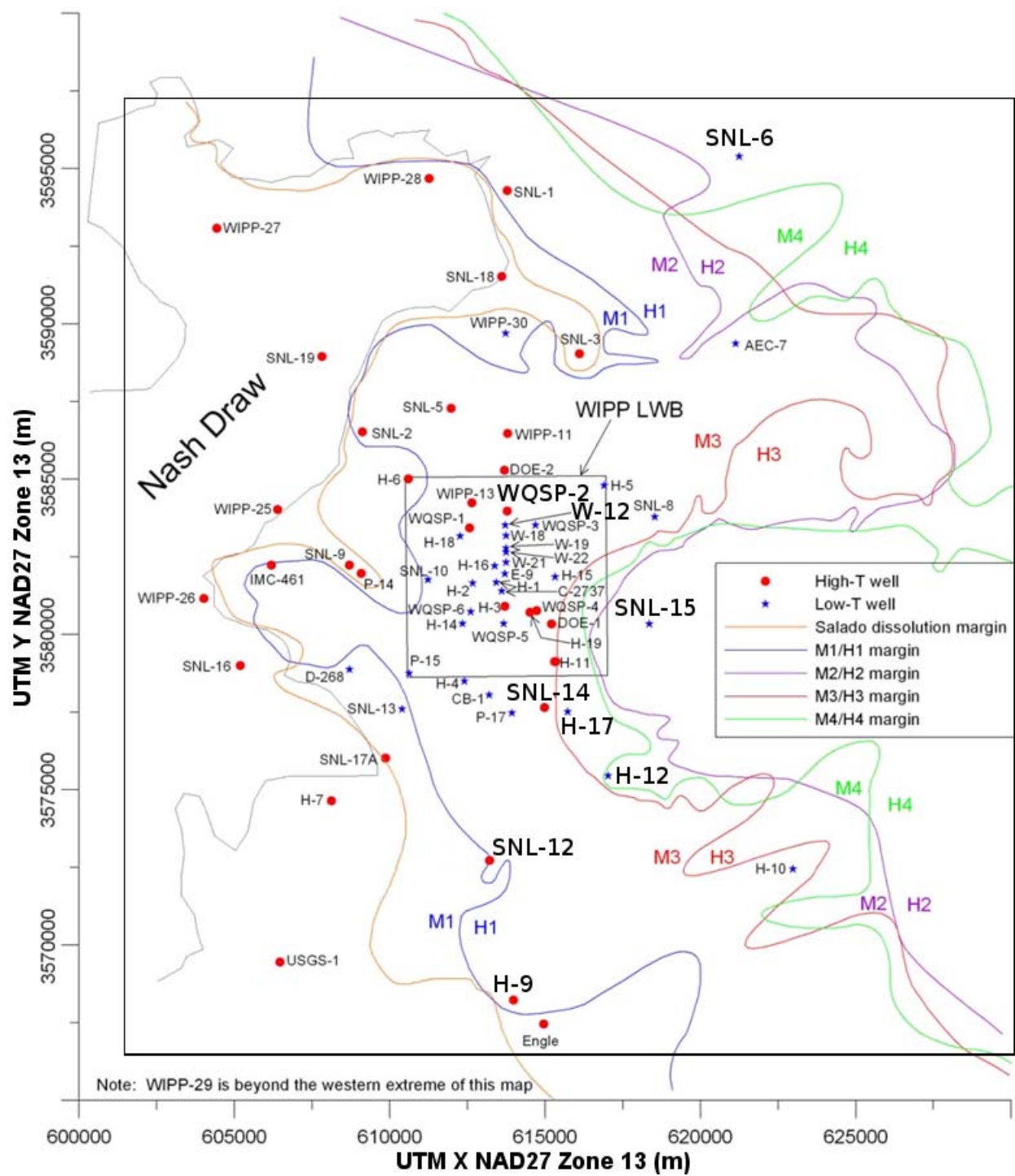
**Figure TFIELD 2-5. M-2/H-2 Halite Margin In the Upper Los Medaños Member**



**Figure TFIELD 2-6. M-3/H-3 Halite Margin In the Tamarisk Member**



**Figure TFIELD 2-7. M-4/H-4 Halite Margin In the Forty-niner Member**



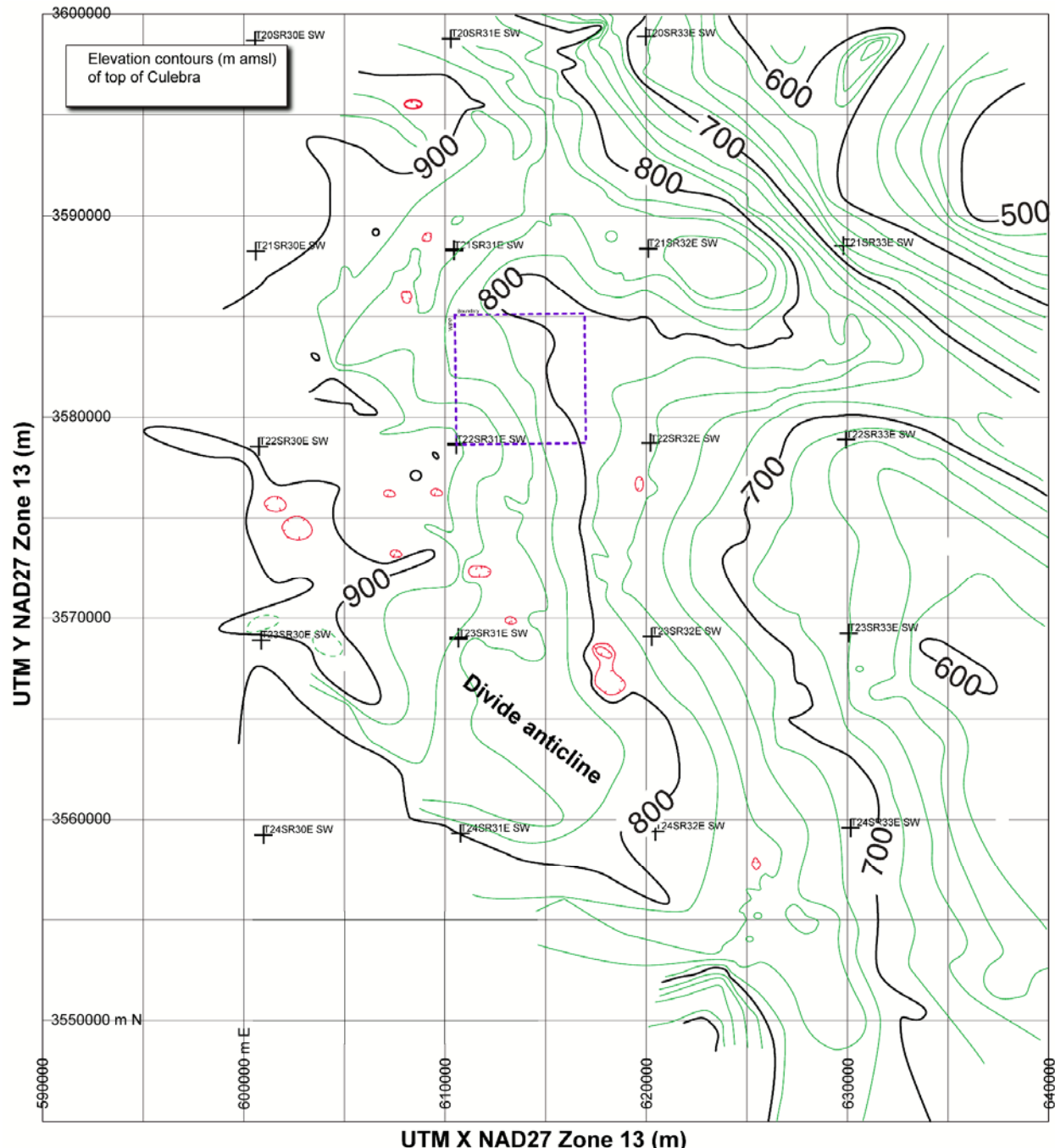


**Figure TFIELD 2-9. Top Elevation (m Above Mean Sea Level (AMSL)) of the Culebra. WIPP LWB indicated with blue dashed line. Township (T) and Range (R) corners indicated with crosses.**

## TFIELD-2.2.2 Salado Dissolution

A margin marking the lateral extent of significant dissolution of upper Salado Formation halite for CRA-2004 PABC was inferred from significant local changes in thickness of the interval between the Culebra Dolomite and the Vaca Triste Sandstone Member of the Salado (Powers

1 2002a and Powers 2002b). For CRA-2009 PABC, the margin was modified to reflect  
2 information indicating embayments of the dissolution margin. Additional data were added south  
3 of the WIPP, with log cross sections, to delineate the margin more accurately (Powers 2003).  
4 Some of these data are reflected in the simplified maps included in Powers et al. (Powers et al.  
5 2003) and Holt et al. (Holt et al. 2005).

6 The Salado dissolution margin was updated for CRA-2009 (see Appendix G from the Analysis  
7 Report for Task 5 of AP-114 (Hart et al. 2008)) based on reinterpretation of geophysical  
8 borehole logs from oil and gas wells in the vicinity of H-9, which were not available for CRA-  
9 2004 PABC. This analysis placed H-9 east of the dissolution line, where previously it was  
10 considered to be within the area affected by Salado dissolution. The Salado dissolution margin is  
11 shown with the Rustler halite margins in Figure TFIELD 2-8, reflecting the change near H-9.

## 12 **TFIELD-2.3 Confinement and Recharge in the Culebra**

13 Field and map studies were performed to identify potential recharge locations south and west of  
14 the WIPP in the southeastern arm of Nash Draw (Powers 2006). This work also identified  
15 Culebra unconfined regions in the same geographic area. The boundaries to the west and south  
16 correspond to the model domain; the northern and eastern boundaries included the southeastern  
17 arm of Nash Draw and an area beyond the apparent eastern extent of the draw.

18 Five elements were identified as contributing to understanding recharge, which might be useful  
19 for modeling the possible effects of recharge to the Culebra in the study area:

- 20 1. extent of and relationship between surface drainage basins,
- 21 2. areas with differing Culebra confinement,
- 22 3. location and character of drainage channels within drainage basins,
- 23 4. location of specific recharge points (e.g., sinkholes), and
- 24 5. soil characteristics and rainfall infiltration across the study area.

25 Of these, the estimate of Culebra confinement is the most interpretive element. Drainage basins,  
26 channels and specific points of recharge are identified using surface topography features  
27 identifiable from maps, aerial photos, or field reconnaissance. Existing maps of soils, combined  
28 with surface reconnaissance and aerial photographs, permitted relatively direct assignment of soil  
29 properties controlling runoff. The degree of confinement of the Culebra in the study area,  
30 however, was not directly determinable from the surface data. As a result, a variety of surface  
31 features and well data were combined to estimate areas where the Culebra is less confined  
32 compared to conditions at the WIPP site, where there are more well-test and drillhole data.

### 33 **TFIELD-2.3.1 Surface Drainage Basins**

34 Drainage basin size and characteristics are important elements to determine how rainfall,  
35 infiltration, and runoff may contribute to recharge of near-surface Rustler hydrologic units in

1 Nash Draw. Topographic maps, aerial photographs, and some field checking were used to define  
2 separate surface drainage basins.

3 The drainage basins are mainly separated by topographic divides and local lows or concentration  
4 points that can be distinguished on 7.5-minute quadrangle topographic maps supplemented by  
5 study of aerial photographs. Because Nash Draw is an area of significant evaporite karst (e.g.,  
6 Powers and Owsley (Powers and Owsley 2003)), collapse features, caves, or sinkholes may  
7 capture local drainage in smaller basins or subbasins wholly enclosed by another basin (Figure  
8 TFIELD 2-10). An example is drainage basin 7, which is wholly enclosed in drainage basin 6  
9 (Figure TFIELD 2-10). These quite localized closed drainage basins in Nash Draw represent  
10 potential recharge locations for the Rustler Formation. Mapping the basins is the first step in  
11 understanding the complex geology and hydrology inside Nash Draw, which expresses itself as  
12 water-level fluctuations in some Culebra wells in and near Nash Draw (see hydrographs and  
13 references in Appendix HYDRO-2014).

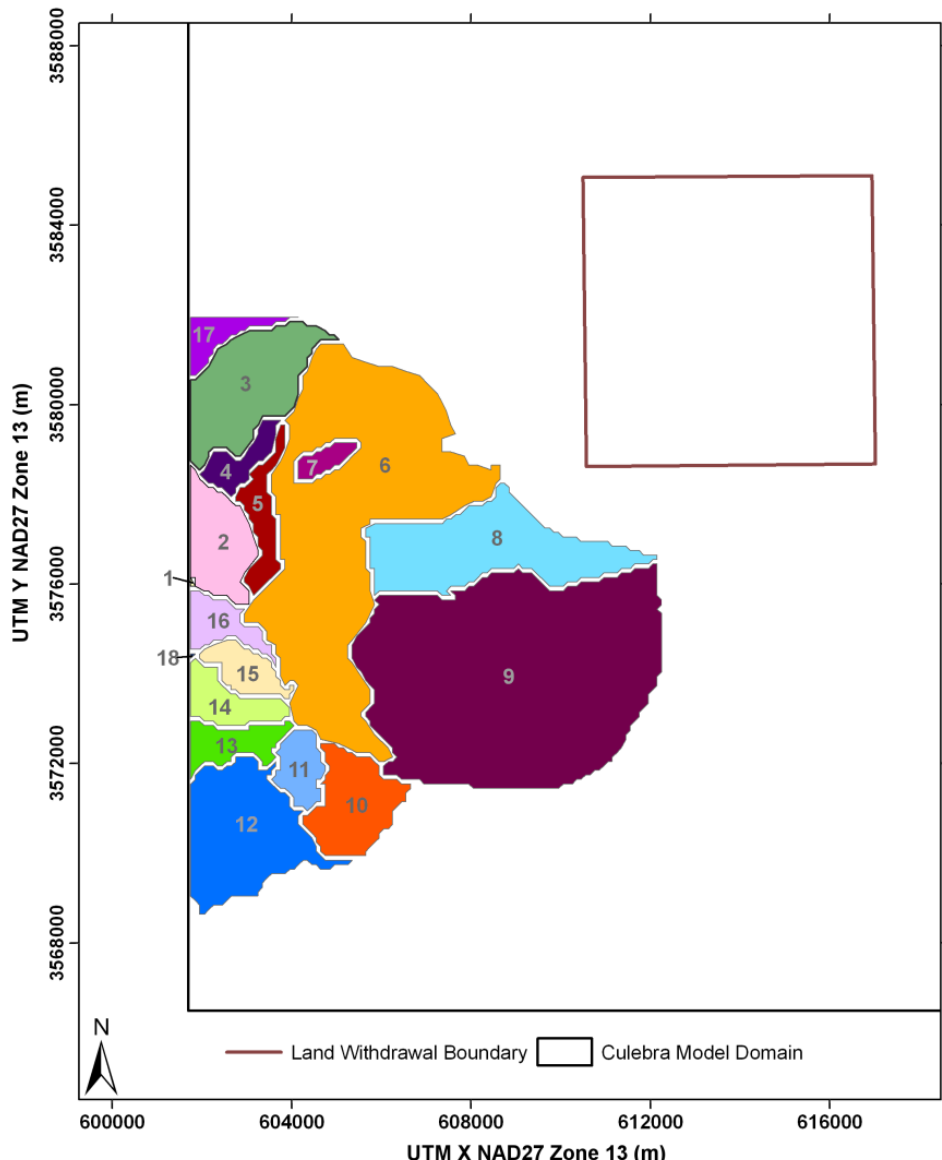


**Figure TFIELD 2-10. Closed Drainage Sub-basins Identified in Southeastern Nash Draw. White areas are either outside Nash Draw or the study area.**

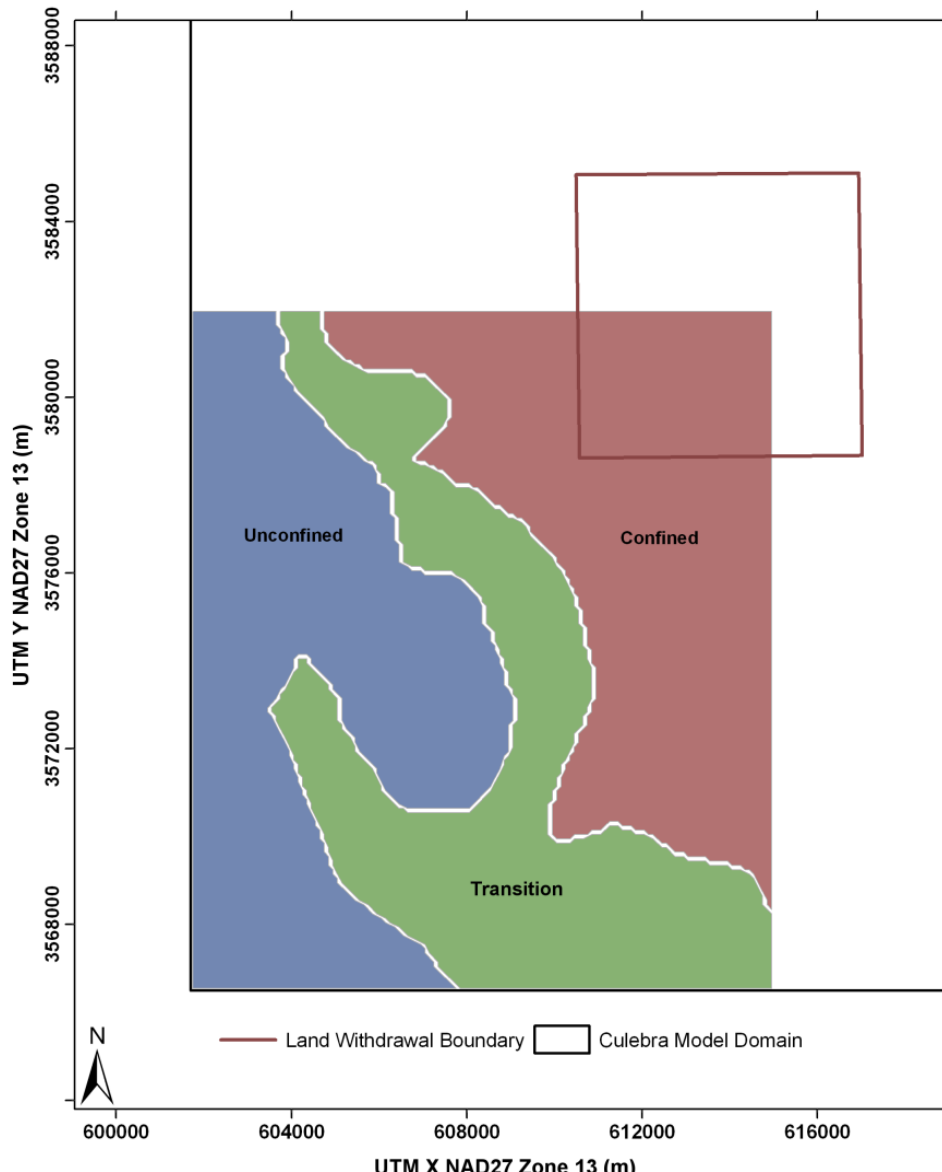
### TFIELD-2.3.2 Culebra Confinement

Across the WIPP site, the Culebra can be considered confined, with little potential for direct vertical recharge for the relatively short time period covered in the WIPP Culebra model calibration (i.e., the length of multi-well pumping tests). Within portions of Nash Draw, the Culebra is very shallow (i.e., only covered by portions of the highly fractured Tamarisk) and observed water levels show the Culebra responds to precipitation events in a very short time (Appendix HYDRO-2014). Due to the interpretative nature of the confinement estimate, no numerical values of storativity were predicted from this geologic analysis, only zones of relatively higher or lower confinement, with an intermediate transition zone. The confined area

1 has a relatively unambiguous definition, whereas the boundary between transition and  
2 unconfined is much more subjective.

3 The area of the Culebra considered confined (red in Figure TFIELD 2-11) is defined  
4 approximately by the interpreted margin of upper Salado halite dissolution (Powers et al. 2003).  
5 There is a significant increase in Culebra *T* values west and south of this margin, and this change  
6 is attributed to changes in fracture aperture associated with strain induced by dissolution. The  
7 transition zone (green in Figure TFIELD 2-11) includes areas where some data from wells  
8 indicate there is some vertical isolation of the Culebra, but information is less conclusive.

9 Most of the Culebra unconfined zone (blue in Figure TFIELD 2-11) is in central Nash Draw and  
10 out of the AP-114 Task 1 study area. The strategy for estimating relative Culebra confinement  
11 was to select areas where the Culebra is known or believed to be very shallow ( $\leq 30$  meters (m)  
12 below ground surface) and where observed recharge points (caves, sinkholes, alluvial dolines)  
13 are believed to access units below the Magenta. Some large caves and sinkholes are developed in  
14 the Tamarisk gypsum beds and have a greater likelihood of providing hydraulic connection to the  
15 Culebra than similar openings in the Forty-niner gypsum beds. Many potash exploration holes  
16 within Nash Draw encountered lost-circulation zones, but the stratigraphic relationships of these  
17 zones to the Culebra are not well constrained. Thus, apart from the location from Livingston  
18 Ridge (the escarpment marking the eastern edge of the surface expression of Nash Draw) and the  
19 upper Salado dissolution margin, the factors determining confinement of the Culebra are  
20 generally qualitative.



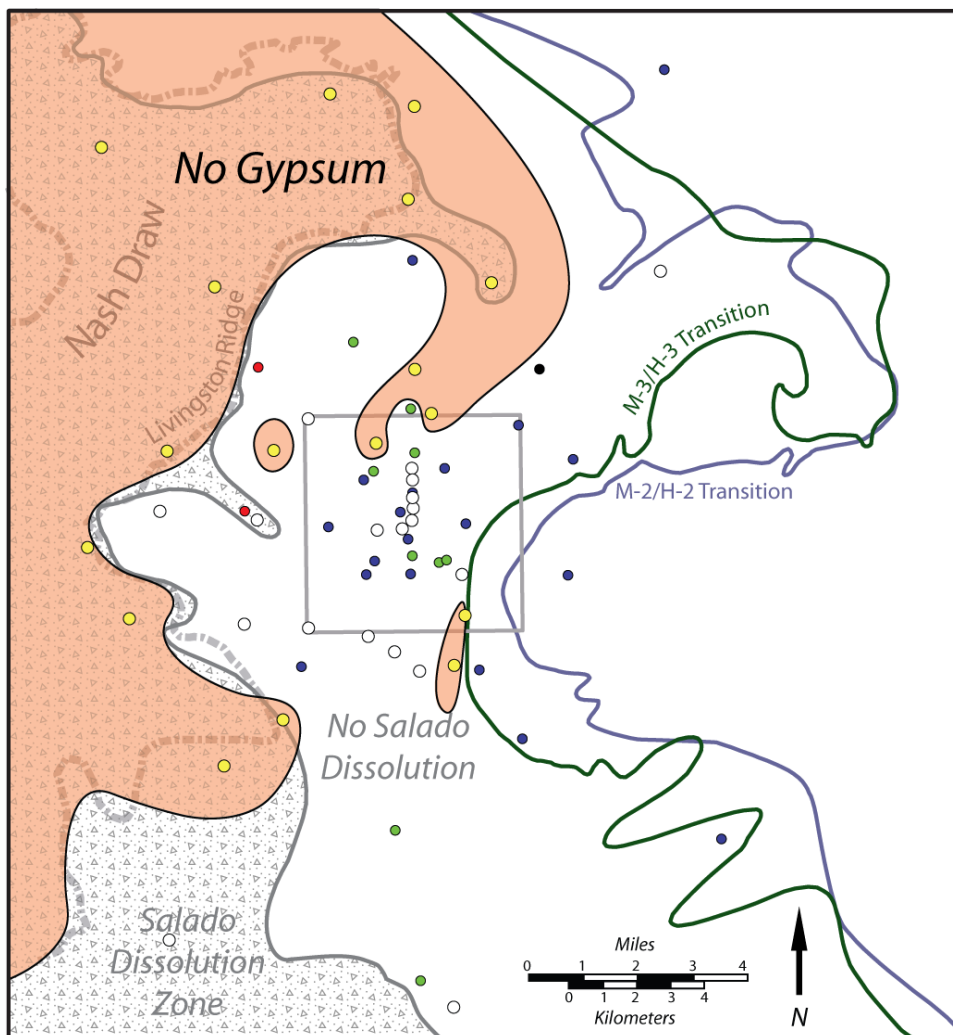
1  
2 **Figure TFIELD 2-11. Culebra Confinement Map for Southern Nash Draw Study**  
3 **Area. White areas are outside the Nash Draw geologic study**  
4 **area. Zones are shown over the entire model area in Figure**  
5 **TFIELD 5-3.**

6 **TFIELD-2.3.3 Gypsum Cements in the Culebra**

7 The amount of gypsum cements in fractures and vuggy porosity within the Culebra is believed to  
8 be inversely related to Culebra  $T$  (Beauheim and Holt 1990). They postulated gypsum fracture  
9 fillings limited Culebra  $T$  by closing fracture apertures, filling critical fracture junctions. The  
10 postulated relationship remained qualitative because too few well locations had both measured  $T$   
11 values and describable core. Since 1990, the Culebra has been cored and hydraulically tested at  
12 24 additional locations, providing sufficient data to construct a quantitative model linking

1 Culebra  $T$  with the presence of gypsum cements. No soft data on gypsum cements was used in T-  
2 field construction or calibration before CRA-2009 PABC.

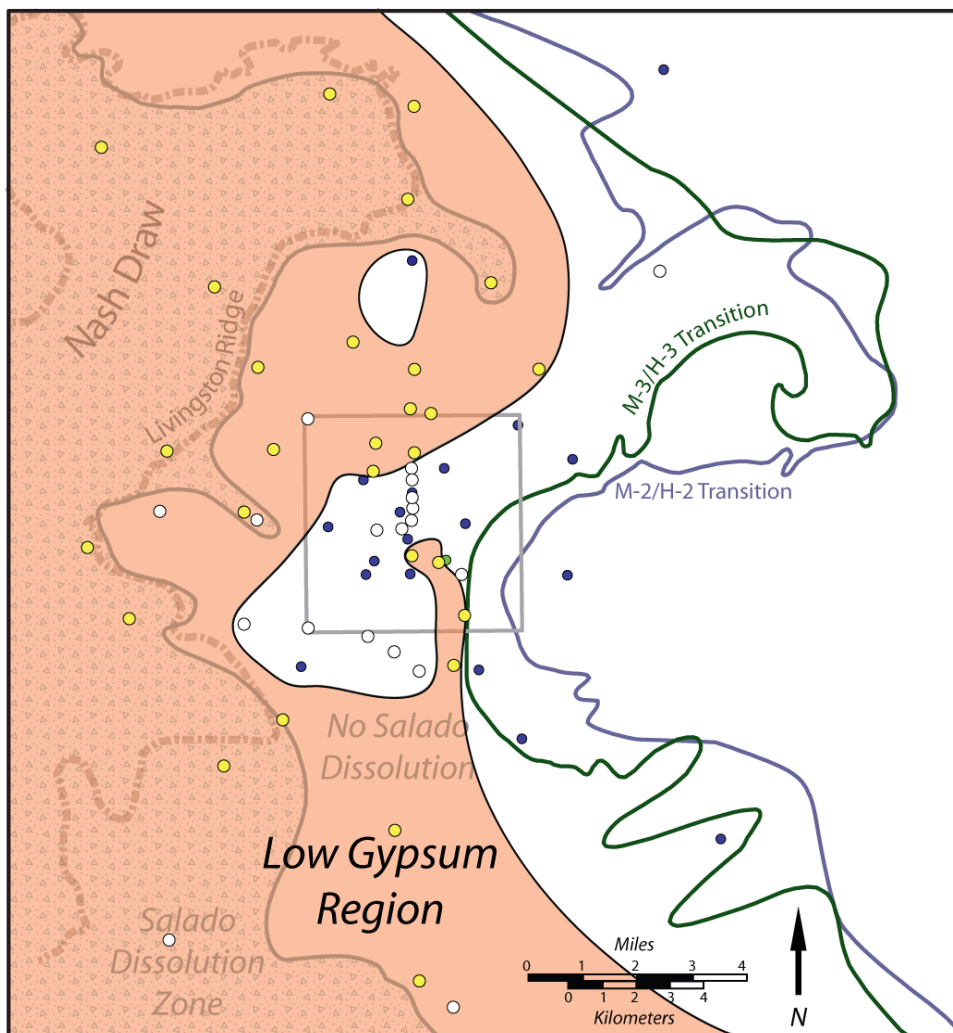
3 In Appendix F of Hart et al. (Hart et al. 2008), a simple quantitative model was constructed  
4 relating Culebra gypsum content to  $T$ . Using units defined by Holt (Holt 1997), maps were  
5 developed to illustrate spatial occurrence of gypsum in the Culebra. The maps used a gypsum  
6 index accounting for the relative Culebra gypsum content (Figure TFIELD 2-12 and Figure  
7 TFIELD 2-13). Using a critical value of the gypsum index, the high- $T$ /low- $T$  status of Culebra  
8 well locations were predicted with an accuracy >97% for WIPP well locations where both  
9 sufficient core and  $T$  estimates exist. These maps revealed that regions of no gypsum occur  
10 predominantly where Salado dissolution has affected the Culebra. The low-gypsum region in the  
11 southern WIPP LWB (Figure TFIELD 2-13) is similar to the high-diffusivity region defined by  
12 Beauheim (Beauheim 2007) (Figure TFIELD 4-2). Soft data were used to incorporate  
13 information about the influence of gypsum content on predicted Culebra  $T$ .



Explanation

- High T Location - Salado Dissolution
- High T Location - No Dissolution
- Low T Location
- No Gypsum
- No Gypsum Data
- No Hydraulic Data

1  
2  
3  
**Figure TFIELD 2-12. Areas Where No Gypsum Has Been Found in Core  
Samples, Corresponding to a Greater Likelihood of Having  
Higher Culebra T Values**



#### Explanation

- High T Location - Salado Dissolution
- High T Location - No Dissolution
- Low T Location
- Low Gypsum Content
- No Gypsum Data

1 **Figure TFIELD 2-13. Areas Where Wells Have Either No or Low Gypsum Content.**  
2 The areas not shaded are likely to have high gypsum content  
3 and lower T.

4

## 1 **TFIELD-3.0 T-Field Conceptual Model Refinement**

2 The work outlined in Section TFIELD-3.0 was performed for CRA-2009 PABC under AP-114,  
3 Analysis Plan for Evaluation and Recalibration of Culebra Transmissivity Fields (Beauheim  
4 2008), and still applies to CRA-2014. The conceptual model for base field creation was  
5 originally explained in Holt and Yarbrough (Holt and Yarbrough 2002), as Task 2, Subtask 1 of  
6 AP-088 for CRA-2004 PABC. Since then, the data supporting the conceptual model were  
7 updated and improved, but the model itself has changed very little. Any deviations of the CRA-  
8 2009 PABC model from the CRA-2009 model due to updates in data or process are discussed in  
9 this section. No updates have occurred for CRA-2014 since CRA-2009 PABC.

10 Figure TFIELD 2-2 illustrates the current geologic and hydrologic conceptual model of the  
11 Culebra dolomite in the vicinity of the WIPP site. Geologic controls on Culebra  $T$  were identified  
12 and a linear regression model relating these controls to  $T$  was constructed. The geology and  
13 geologic history of the Culebra has been described in detail elsewhere in the literature (Holt and  
14 Powers 1988; Beauheim and Holt 1990; Holt 1997). The following conceptual model was  
15 developed from this published work. Specifically, the model follows Holt (Holt 1997) in  
16 assuming variability in Culebra  $T$  is due strictly to post-depositional processes. Throughout the  
17 following discussion, the informal stratigraphic subdivisions of Holt and Powers (Powers 1988)  
18 are used to identify geologic units within the Rustler Formation, as listed in Figure TFIELD 2-3  
19 and shown in map view for the Culebra model area in Figure TFIELD 2-8. The Culebra  
20 conceptual model given in this section passed a peer review (Burgess et al. 2008) before the  
21 calibration process in Section TFIELD-5.0 was begun.

22 It is hypothesized that Culebra  $T$  spatial distribution is a function of several geologic factors,  
23 some of which can be determined at a location using mapped geologic data, including:

- 24 1. Culebra overburden thickness,
- 25 2. fracture interconnection,
- 26 3. presence of gypsum cements in fractures and vuggy porosity,
- 27 4. dissolution of the upper Salado Formation below the Culebra, and
- 28 5. occurrence of halite in Rustler units above or below the Culebra.

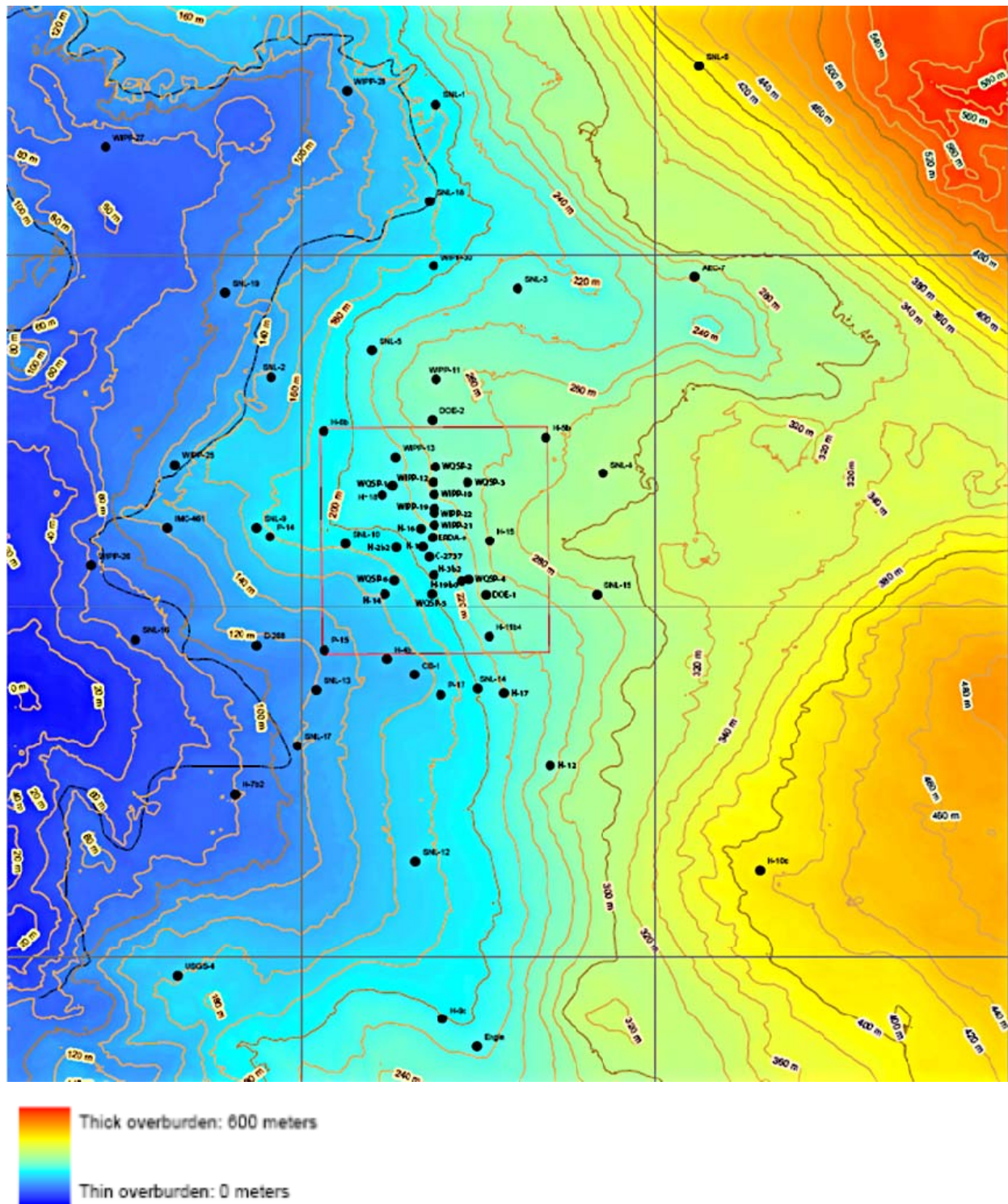
29 High- $T$  regions near the WIPP cannot be predicted using geologic data, as they represent areally  
30 persistent zones of well-interconnected fractures, and fracture interconnection cannot be  
31 observed or inferred from core or geophysical log data. Fracture interconnection is therefore  
32 treated as a stochastic process. Presence of gypsum cements in the Culebra, occurrence of  
33 Rustler halite, and Culebra overburden thickness instead varies slowly in space. These properties  
34 can be meaningfully mapped at the scale of the groundwater flow model.

1 **TFIELD-3.1 Model Domain**

2 The CRA-2009 PABC model domain was expanded to the east relative to the domain used for  
3 the CRA-2004 (U.S. DOE 2004) to reach an area where halite is present in all of the non-  
4 dolomite members of the Rustler Formation. This change was made to simplify the specification  
5 of the eastern boundary condition of the model. The current extent of the model domain is  
6 601,700 to 630,000 m UTM X NAD27 and 3,566,500 to 3,597,100 m UTM Y NAD27. The  
7 domain was discretized into 100-m square cells, yielding a model 284 cells wide by 307 cells  
8 high. The Culebra was modeled as a single layer of uniform 7.75-m thickness (U.S. DOE 1996).  
9 The area covered by Figure TFIELD 2-8 corresponds to the model domain, showing the WIPP  
10 site boundary, the relevant geologic margins, and various Culebra monitoring wells. The model  
11 domain for CRA-2014 has not changed since CRA-2009 PABC.

12 **TFIELD-3.2 Overburden Thickness**

13 An inverse relationship was hypothesized between Culebra overburden thickness and Culebra  $T$ .  
14 Overburden thickness is a metric for two different controls on Culebra  $T$ . First, fracture apertures  
15 can be related to overburden thickness (e.g., Currie and Nwachukwu 1974), as lower  $T$  are found  
16 where Culebra depths are greater (Beauheim and Holt 1990; Holt 1997). Second, erosion of  
17 overburden leads to stress-relief fractures, and the amount of Culebra fracturing increases as the  
18 overburden thickness decreases (Holt 1997). The structure contour map of Culebra elevation  
19 (Figure TFIELD 2-9) has been constructed using geophysical logs from hundreds of oil and gas  
20 wells, and geologic information from more than 100 WIPP-related boreholes. The difference  
21 between the land surface elevation (as obtained from U.S. Geological Survey (USGS)  
22 topographic maps) and Culebra elevation is the overburden thickness (Figure TFIELD 3-1).  
23 Culebra overburden thickness ranges from near zero in the southern end of Nash Draw, to over  
24 550 m in the northeastern corner of Figure TFIELD 3-1. The depth to the Culebra from the land  
25 surface defined the value of  $d(x,y)$  for each cell in the Culebra model domain.



1 **TFIELD-3.3 Fracture Interconnection**

2 High- $T$  zones within the Culebra are associated with interconnected fractures and occur  
3 randomly between areas bounded on the west by the Salado dissolution margin and on the east  
4 by H2 and/or H3 (the central area Zone 4 in Figure TFIELD 3-2). In these zones, fractures are  
5 well-interconnected, and fracture interconnectivity is controlled by a complicated history of  
6 fracturing with several episodes of cement precipitation and dissolution (Beauheim and Holt  
7 1990; Holt 1997). Unfortunately, no geologic metric for fracture interconnectivity was  
8 identifiable in cores or from subsurface geophysical logs, and fracture interconnectivity has only  
9 been identified from *in situ* hydraulic test data.

10 Because of this lack of a corresponding easy-to-map geologic metric for fracture  
11 interconnectivity, the spatial location of high- $T$  zones was considered to be a stochastic process  
12 that could not be predicted deterministically. The spatial layout of these zones was simulated for  
13 CRA-2009 PABC using geostatistical indicator kriging with conditioning data (this was not  
14 changed for CRA-2014 since CRA-2009 PABC). This stochastic development of zones was a  
15 change from CRA-2004 PABC (Holt and Yarbrough 2002), where the only conditioning  
16 information was based on the  $T$  at wells. Information was added to the geostatistical model to  
17 increase the likelihood of high  $T$  being placed between two wells that hydraulic testing has  
18 revealed to be associated with larger diffusivity values. North of the WIPP site (i.e., south of  
19 WIPP-30) evidence exists for *both* high levels of gypsum in the Culebra and relatively high  $D$   
20 between pumping/observation well pairs. In this unique region, the geologic conceptual model  
21 indicates there is slightly lower probability of being in a high- $T$  zone than in other areas where a  
22 high  $D$  or high  $T$  estimate exists. Section TFIELD-4.2 discussed the process of merging  
23 hydraulic hard and soft data (single-well  $T$  estimates and multi-well  $D$  estimates, respectively)  
24 with geologic soft data on gypsum.

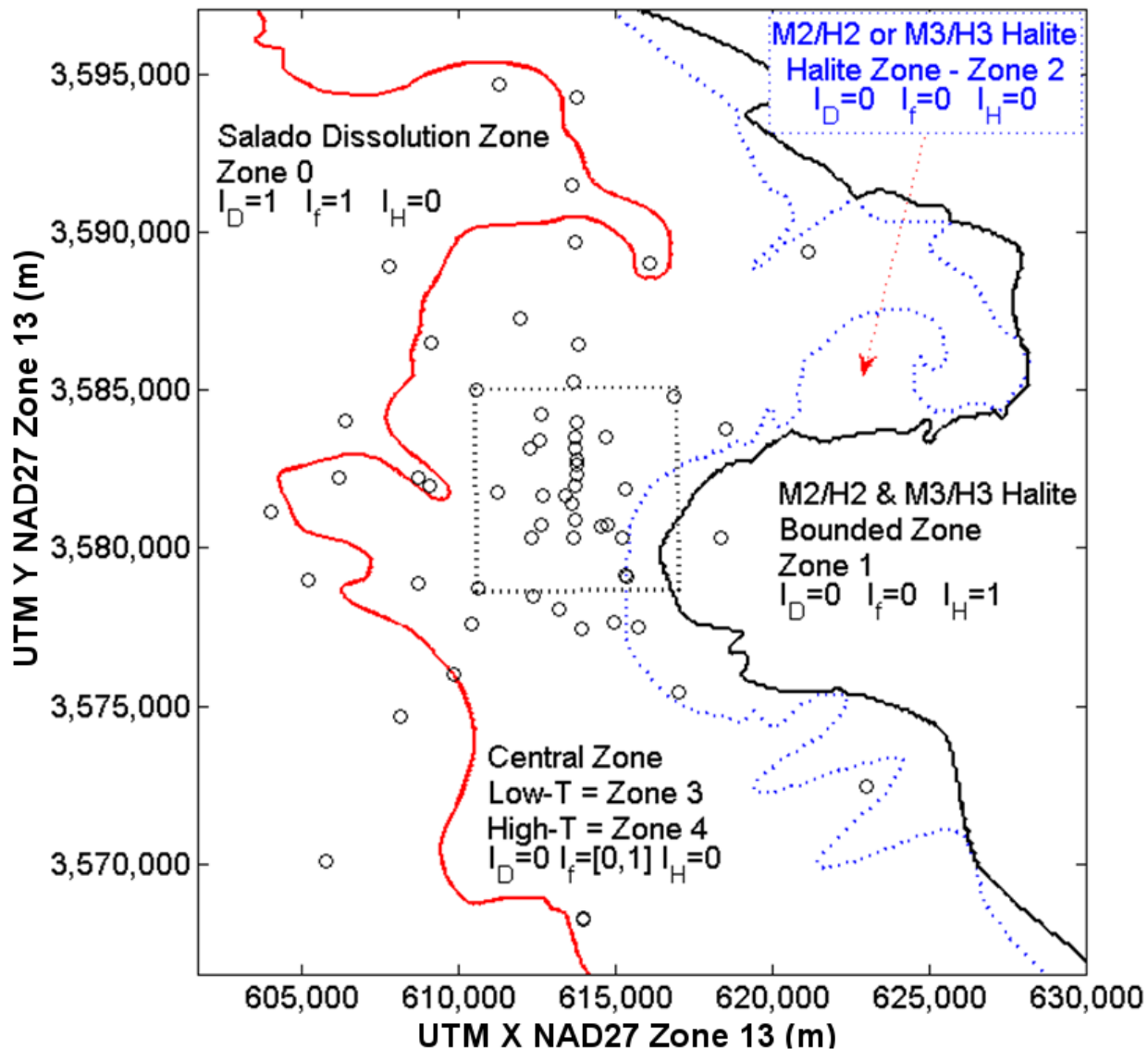


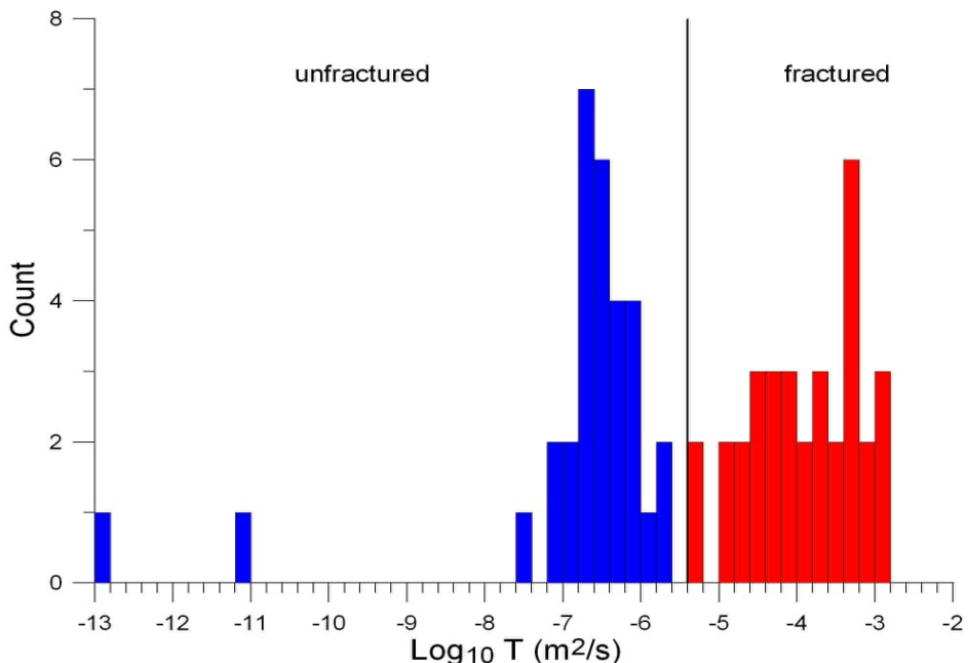
Figure TFIELD 3-2. Conceptual Model Zones With Indicator Values and Zone Numbers (Equation TFIELD 3.2). Zones 3 and 4 are distributed randomly between the Salado dissolution margin and westernmost M2/H3 or M3/H3 Rustler halite margins.

The Culebra  $T$  estimates at WIPP wells used in the CRA-2009 PABC modeling were the same as those used by Holt and Yarbrough (Holt and Yarbrough 2002), supplemented by more recent data reported from subsequent pumping tests (Roberts 2006 and 2007; Bowman and Roberts 2008). The  $\log_{10} T$  data show a bimodal distribution in Figure TFIELD 3-3. Closely spaced wells sometimes show very different values; higher- $T$  values are hypothesized to reflect the presence of well-interconnected fractures absent at lower- $T$  locations. For example, wells WQSP-2 and WIPP-12 are only 454 m apart, but have  $T$  values differing by over two orders of magnitude (see blue star labeled W-12 and red circle labeled WQSP-2 in the north portion of the WIPP LWB in Figure TFIELD 2-8). Thus, the fractures present at WQSP-2 apparently do not extend to WIPP-12 or are not intersected by the WIPP-12 borehole. Well-interconnected fractures occur in

1 regions affected by Salado dissolution (e.g., Nash Draw) and in areas with complicated cement  
 2 dissolution and precipitation histories (e.g., high- $T$  zones near the WIPP site). The natural break  
 3 between the measured  $\log_{10} T$  square meters per second ( $m^2/s$ ) values at  $-5.4$  (Holt and  
 4 Yarbrough 2002) is illustrated with a vertical black line in Figure TFIELD 3-3. The fracture-  
 5 interconnection indicator ( $I_f$ ) is defined in terms of this break (Equation TFIELD 3.1).

6

$$I_f = \begin{cases} 1, & \log_{10} T(m^2/s) \geq -5.4 \\ 0, & \log_{10} T(m^2/s) < -5.4 \end{cases} \quad (\text{TFIELD 3.1})$$



7

8 **Figure TFIELD 3-3. Histogram of Log<sub>10</sub> Culebra Transmissivity ( $T$ ) Estimates at**  
 9 **WIPP Wells from Single-well Tests**

10 **TFIELD-3.4 Salado Dissolution**

11 Slight modification was made to the Salado dissolution margin used in CRA-2009 PABC,  
 12 compared to CRA-2009, as outlined in Section TFIELD-2.2.2. No modifications were made for  
 13 CRA-2014 since CRA-2009 PABC. The indicator variable for Salado dissolution is  $I_D$ , and was  
 14 defined to be 1 in areas of the model domain where dissolution has occurred, and 0 elsewhere.  
 15 The Salado dissolution margin is plotted with the Rustler halite margins in Figure TFIELD 2-8.

16 **TFIELD-3.5 Rustler Halite Margins**

17 The M2/H2 and M3/H3 Rustler halite margins were modified for CRA-2009 PABC compared to  
 18 CRA-2009, as outlined in Section TFIELD-2.2.1. No modifications were made for CRA-2014  
 19 since CRA-2009 PABC. The margins are shown individually in Figure TFIELD 2-5 and Figure  
 20 TFIELD 2-6, and together with the M1/H1 and M4/H4 Rustler halite margins and Salado  
 21 dissolution margin in Figure TFIELD 2-8.

1   Wells SNL-6 and SNL-15 were drilled since Holt and Yarbrough (Holt and Yarbrough 2002).  
 2   They are located east of the M2/H2 and M3/H3 halite margins, where halite is present in both  
 3   intervals (see Figure TFIELD 2-8). As predicted by Holt (Holt 1997), the Culebra itself was  
 4   partially cemented with halite at these locations, and estimated  $T$  were extremely low (Roberts  
 5   2007; Bowman and Roberts 2008). Based on these observations, Culebra  $T$  is assumed lower in  
 6   the region where halite occurs both above (in the M3/H3 interval) and below (in the M2/H2  
 7   interval), than the Culebra  $T$  where halite occurs in only one of these intervals. The indicator  
 8   term  $I_H$  was defined to be 1 at any point where halite is present in both the M2/H2 and M3/H3  
 9   margins, and to be 0 elsewhere.

## 10   **TFIELD-3.6 Transmissivity Regression Model**

11   The following linear model for  $Y(x,y) = \log_{10} T(x,y)$  was constructed

$$12   Y(x,y) = \begin{cases} \beta_1 + \beta_2 d(x,y) + \beta_3 + \beta_4 & Salado \text{ Dissolution} & I_D = 1, I_f = 1, I_H = 0 \\ \beta_1 + \beta_2 d(x,y) + \beta_3 & Central \text{ High-}T & I_D = 0, I_f = 1, I_H = 0 \\ \beta_1 + \beta_2 d(x,y) & Central \text{ Low-}T & I_D = 0, I_f = 0, I_H = 0 \\ \beta_1 + \beta_2 d(x,y) & M2 / H2 | M3 / H3 & I_D = 0, I_f = 0, I_H = 0 \\ \beta_1 + \beta_2 d(x,y) + \beta_5 & M2 / H2 \& M3 / H3 & I_D = 0, I_f = 0, I_H = 1 \end{cases} \text{ (TFIELD 3.2)}$$

13   where  $\beta_1$  through  $\beta_5$  are regression coefficients, the two-dimensional location vector  $(x,y)$   
 14   consists of NAD27 UTM Zone 13  $x$  and  $y$  coordinates,  $d(x,y)$  is the Culebra overburden  
 15   thickness (Figure TFIELD 3-1),  $I_f$  is an indicator of whether interconnected fractures are present  
 16   in the Culebra,  $I_D$  is the Salado dissolution indicator, and  $I_H$  is the halite bounding indicator. In  
 17   this model, | means logical or, while & means logical and. Regression coefficient  $\beta_1$  is the  
 18   intercept value for the linear model. Coefficient  $\beta_2$  is the slope of  $Y(x,y)/d(x,y)$ . The coefficients  
 19    $\beta_3, \beta_4$ , and  $\beta_5$  represent adjustments to the intercept for the occurrence of interconnected  
 20   fractures, Salado dissolution, and halite bounding, respectively. Although other types of linear  
 21   models could have been developed, Equation TFIELD 3.2 is consistent with the conceptual  
 22   model relating Culebra  $T$  to geologic controls, can be tested using published WIPP geologic and  
 23    $T$  estimates, and can be potentially verified with new Culebra wells.

24   Because there are only two data points for  $T$  in the zone where Culebra is bounded by halite, and  
 25   both are significantly lower than any other  $T$  values in the model, the  $\beta_5 I_H$  term in Equation  
 26   TFIELD 3.2 was included to take into account the very low  $T$  zone. This was done to keep the  
 27   conceptual model consistent for all zones, recognizing the base fields are primarily a starting  
 28   point for subsequent calibration.

29   The combined results of the regression and the indicator kriging (Section TFIELD-4.3) were  
 30   1,000 base  $T$ -fields that shared certain geologic features, but were different from one another.  
 31   This difference was provided by the stochastic placement of high- $T$  areas in the central zone.  
 32   These areas were placed using the GSLIB Sequential Indicator Simulation (SISIM) routine  
 33   (qualified for use in WIPP PA according to NP 19-1 (Chavez 2006)). This routine used  
 34   geostatistical methods to create stochastic indicator (Boolean value) fields.

1 **TFIELD-3.7 Culebra Conceptual Model Peer Review**

2 The Culebra conceptual model given in this section passed peer review before proceeding with  
3 the CRA-2009 PABC calibration of the Culebra T fields (Burgess et al. 2008). The peer review  
4 panel found the methodology presented here to be adequate, accurate, and valid enough to justify  
5 proceeding with the numerical implementation and calibration of the Culebra T-fields. The panel  
6 found the CRA-2009 PABC conceptual model to be greatly improved, compared to the Culebra  
7 conceptual model used in the Compliance Certification Application (CCA) (U.S. DOE 1996).  
8 The panel found the understanding of the physical processes connecting the Culebra groundwater  
9 geochemistry with the Culebra hydraulic properties to be insufficient. The peer review panel did  
10 not feel this particular lack of understanding would be a problem in T-field development and  
11 calibration, due to the relatively high density of Culebra hydrologic data available at the WIPP  
12 site.

## 1 **TFIELD-4.0 Base T-Field Construction**

2 The work outlined in Section TFIELD-4.0 was performed under AP-114, Analysis Plan for  
3 Evaluation and Recalibration of Culebra  $T$  Fields (Beauheim 2008). This section discusses  
4 details associated with the incorporation of soft and hard data into the base T-field construction  
5 process. The base Culebra T-fields were the starting point for the calibration processes outlined  
6 in Section TFIELD-5.0. Aside from the definitions of some fixed parameter zones, all the  
7 parameters specified in the base T-field construction were allowed to be modified during the  
8 calibration process to produce model output that better matched observed steady-state and  
9 transient pressure observations. Inside the WIPP LWB there is a large amount of hard data to  
10 constrain the parameters of the groundwater model during calibration, while distant to the WIPP  
11 LWB the hard data are not sufficient to uniquely constrain the calibration. To help alleviate this  
12 problem, base T-field construction used soft data to provide additional constraints that could not  
13 be incorporated directly into the calibration process. Specification of soft data was used to create  
14 physically realistic starting points for the calibration. The starting point for the calibration has the  
15 most impact at locations distant to the WIPP LWB.

16 Kriging is a linear estimation process in the field of geostatistics that predicts an average value at  
17 locations without observations, using available observations and a model describing the  
18 variability of the function (i.e., the variogram, which is itself estimated from data). Indicator  
19 kriging is a specific form of the kriging where cutoffs are estimated (i.e., is the value above or  
20 below 1.0?), rather than a continuous value. Conditional stochastic simulation is a geostatistical  
21 approach for generating realizations that will have a common specified statistical structure  
22 specified through a variogram and data, but are otherwise random. Kriging predicts the mean and  
23 variance of a field, resulting in smooth mean fields. Kriging would be conceptually similar to  
24 generating many stochastic simulations and averaging the results. Conditional stochastic  
25 simulation with indicator kriging was used to predict location of high- and low- $T$  areas  
26 (is  $\log_{10} T > -5.4$  or  $< -5.4$ ?), taking the model indicator variogram and various hard and soft  
27 data into account.

28 The constraints used to construct the base T-fields included a class-based linear regression  
29 relationship between  $\log_{10} T$  and Culebra overburden within each type of well (see Section  
30 TFIELD-4.1) and geologic soft data such as the presence of halite in nearby units or gypsum  
31 cements in the Culebra (see Section TFIELD-4.2). The indicator variograms were constructed  
32 from these data (see Section TFIELD-4.3) and used to stochastically simulate the cutoff between  
33 high and low Culebra  $T$  (see Section TFIELD-4.4). The indicator kriging simulation result was a  
34 component of the base T-field construction (see Section TFIELD-4.5).

## 35 **TFIELD-4.1 Step 1 – Linear Regression Analysis**

36 The best fit to estimate  $T$  from single well tests was based on a multi-line regression analysis.  
37 The wells were separated into three groups: wells in the Salado dissolution zone, wells with low-  
38  $T$  pumping test results, and wells with high- $T$  pumping test results. Figure TFIELD 4-1 shows  
39 the  $\log_{10} T$  values from pumping test results, the Culebra overburden thickness, and the  
40 regression lines fit to each group's data individually. The cutoff between low and high  $\log_{10} T$  is  
41  $-5.4$ . Wells located where the Culebra is bounded above and below by halite (SNL-6 and SNL-  
42 15) were considered outliers and were not included in the regression analysis. Instead, the  $\beta_{5I_H}$

1 term was chosen to yield values close to those interpreted from tests at SNL-6 and SNL-15  
 2 (presented in Appendix F of Hart et al. (Hart et al. 2008), Table F-1); this value was directly  
 3 modified during the calibration stage in AP-114 Task 7 (Hart et al. 2009). The final regression  
 4 equation for  $Y = \log_{10} T$  (Equation TFIELD 4.1) and a table of the  $\beta$  values (Table TFIELD 4-1)  
 5 resulted in a fit characterized by  $R^2 = 0.92$  and  $F = 216$ .

6

$$Y(x, y) = \beta_1 + \beta_2 d(x, y) + \beta_3 I_f(x, y) + \beta_4 I_D(x, y) + \beta_5 I_H(x, y) + \varepsilon \quad (\text{TFIELD 4.1})$$

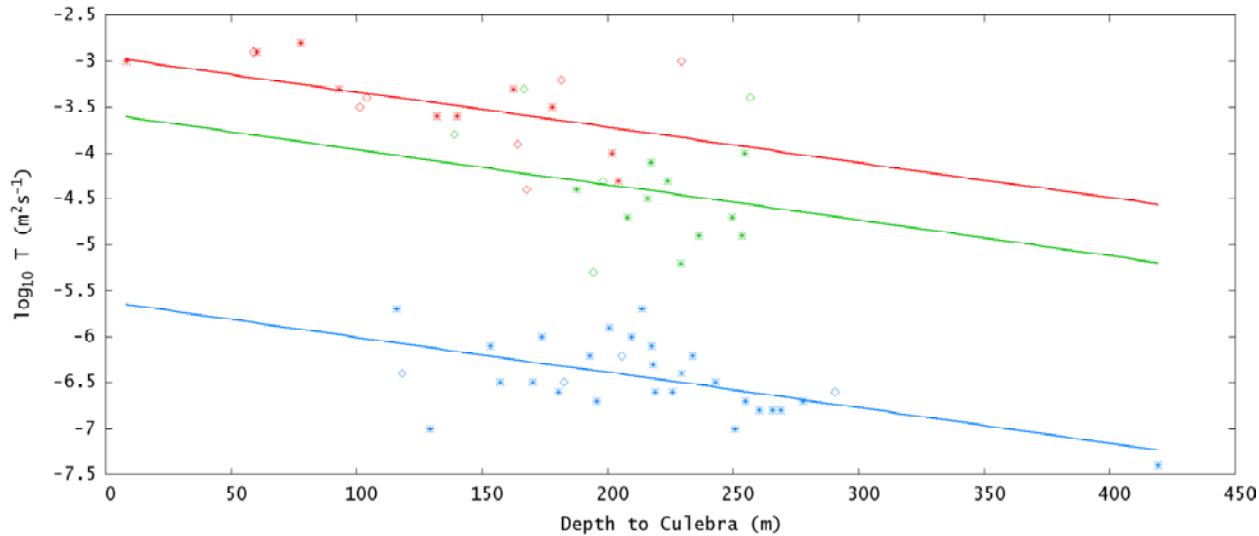
7 The remainder ( $\varepsilon$ ) represents the misfit between the regression model and observed data.

8 **Table TFIELD 4-1.  $\beta$ -values for Regression Equation TFIELD 4.1**

$\beta_1$	$\beta_2$	$\beta_3$	$\beta_4$	$\beta_5$
-5.69805	$-3.48357 \times 10^{-3}$	2.06581	0.68589	-4.75095

9

10 The data and calculations were provided in Appendix A of Hart et al. (Hart et al. 2008).



11

12 **Figure TFIELD 4-1. Regression Lines for Low- $T$  Wells (Blue), High- $T$  and Non-  
 13 dissolution Wells (Green), and Wells Within the Salado Dissolution  
 14 Zone (Red). Open diamonds are wells new to the CRA-2009 PABC  
 15 regression analysis (i.e., not included in CRA-2004 PABC).**

16 **TFIELD-4.2 Step 2 – Creation of Soft Data**

17 Geologic and hydraulic information are included as soft data to maintain the geologic conceptual  
 18 model through the stochastic indicator kriging simulations in Section TFIELD-4.4. Soft data  
 19 define probabilities ( $P_{\text{low}}$ ) a new well at a given point would have a low  $T$  value. For model cells  
 20 that include wells where  $\log_{10} T$  ( $\text{m}^2/\text{s}$ ) has been estimated from single-well hydraulic tests, the  
 21 observation is referred to as hard data to distinguish it from more indirect contributions to  $T$

1 values associated with soft data. Model cells where hard data (single-well test-derived  $\log_{10} T$ ) is  
 2 greater than  $-5.4$  are assigned  $P_{\text{low}} = 0$ , while  $P_{\text{low}} = 1$  for all cells containing low- $T$  pumping test  
 3 results. Estimated  $T$  used as hard data are presented in Table TFIELD 4-2, including coordinates,  
 4 depth, and  $\log_{10} T$  values used in regression model (from Listing A.1 of Appendix A in Hart et  
 5 al. (Hart et al. 2008)).

6 **Table TFIELD 4-2. Listing of Coordinates, Culebra Depth, and  $\log_{10} T$  Estimates from**  
 7 **Single-well Tests (Hard Data) Used in Regression Model (Equation TFIELD 4.1)**

Well	UTM X NAD27, Zone 13 (m)	UTM Y NAD27, Zone 13 (m)	depth to Culebra (m)	$\log_{10} T$ ( $\text{m}^2/\text{s}$ )
H-10b	622975	3572473	419.25	-7.4
P-15	610624	3578747	129.24	-7.0
WIPP-12	613710	3583524	250.7	-7.0
AEC-7	621126	3589381	269.14	-6.8
H-15	615315	3581859	265.79	-6.8
WQSP-3	614686	3583518	260.38	-6.8
H-12	617023	3575452	254.97	-6.7
H-5c	616903	3584802	277.82	-6.7
WIPP-30	613721	3589701	195.69	-6.7
H-17	615718	3577513	219.03	-6.6
SNL-8	618523	3583783	291.5	-6.6
WIPP-21	613743	3582319	225.85	-6.6
WQSP-6	612605	3580736	180.31	-6.6
CB-1	613191	3578049	157.27	-6.5
H-14	612341	3580354	170.23	-6.5
SNL-10	611217	3581777	182.58	-6.5
WIPP-18	613735	3583179	243.08	-6.5
SNL-13	610394	3577600	118.26	-6.4
WIPP-22	613739	3582653	229.51	-6.4
ERDA-9	613696	3581958	218.08	-6.3
C-2737	613597	3581401	205.74	-6.2
H-2c	612666	3581668	192.94	-6.2
WIPP-19	613739	3582782	233.93	-6.2
H-16	613369	3582212	217.46	-6.1
H-4c	612406	3578499	153.31	-6.1
H-1	613423	3581684	209.55	-6.0
P-17	613926	3577466	173.89	-6.0
WQSP-5	613668	3580353	200.67	-5.9
D-268	608702	3578877	115.98	-5.7
H-18	612264	3583166	213.57	-5.7
SNL-5	611970	3587285	194.16	-5.3
H-19b0	614514	3580716	229.2	-5.2
DOE-1	615203	3580333	253.44	-4.9
WQSP-4	614728	3580766	236.42	-4.9
H-3b1	613729	3580895	207.87	-4.7
WQSP-2	613776	3583973	249.72	-4.7
WQSP-1	612561	3583427	215.79	-4.5
H-6c	610610	3584983	187.61	-4.4
SNL-9	608705	3582238	167.64	-4.4

Well	UTM X NAD27, Zone 13 (m)	UTM Y NAD27, Zone 13 (m)	depth to Culebra (m)	$\log_{10} T$ ( $\text{m}^2/\text{s}$ )
Engle	614953	3567454	204.22	-4.3
H-11b4	615301	3579131	223.93	-4.3
SNL-14	614973	3577643	198.12	-4.3
WIPP-13	612644	3584247	217.17	-4.1
DOE-2	613683	3585294	254.51	-4.0
H-9c	613974	3568234	201.78	-4.0
SNL-18	613606	3591536	163.98	-3.9
SNL-2	609113	3586529	138.99	-3.8
WIPP-25	606385	3584028	140.06	-3.6
WIPP-28	611266	3594680	131.98	-3.6
P-14	609084	3581976	178	-3.5
SNL-17	609863	3576016	101.19	-3.5
SNL-19	607816	3588931	103.94	-3.4
WIPP-11	613791	3586475	256.95	-3.4
SNL-12	613210	3572728	166.73	-3.3
USGS-1	606462	3569459	162.44	-3.3
WIPP-27	604426	3593079	92.97	-3.3
SNL-1	613781	3594299	181.66	-3.2
SNL-3	616103	3589047	229.51	-3.0
WIPP-29	596981	3578694	8.23	-3.0
SNL-16	605265	3579037	58.83	-2.9
WIPP-26	604014	3581162	60.2	-2.9
H-7c	608095	3574640	77.88	-2.8

1

## 2 TFIELD-4.2.1 Halite Bounding

3 Two geologic margins, M2/H2 and M3/H3, were updated by Powers (2007a and 2007b), as  
 4 summarized in Section TFIELD-2.2.1. Wells penetrating the Culebra in areas that are bounded  
 5 both above and below by halite (e.g., SNL-6 and SNL-15) have been found to have very low  $T$   
 6 estimates, less than  $10^{-11} \text{ m}^2/\text{s}$  (Roberts 2007). Wells bounded by only one margin (e.g., H-12  
 7 and H-17) have lower than average  $T$  estimates.

8 Because high- $T$  fractures are not predicted where halite is present in the Rustler, model cells  
 9 located on the combined M2/H2 and M3/H3 margin were assigned  $P_{\text{low}} = 1$ . This ensured that no  
 10 high- $T$  areas were placed on the boundary itself, largely a cosmetic consistency fix. Additionally,  
 11 regression results for all model cells in the halite zone were replaced with values directly from  
 12 the regression equation; indicator values were only used in Zones 3 and 4, and were not used east  
 13 of the Rustler halite margins in Zone 1 (Figure TFIELD 3-2).

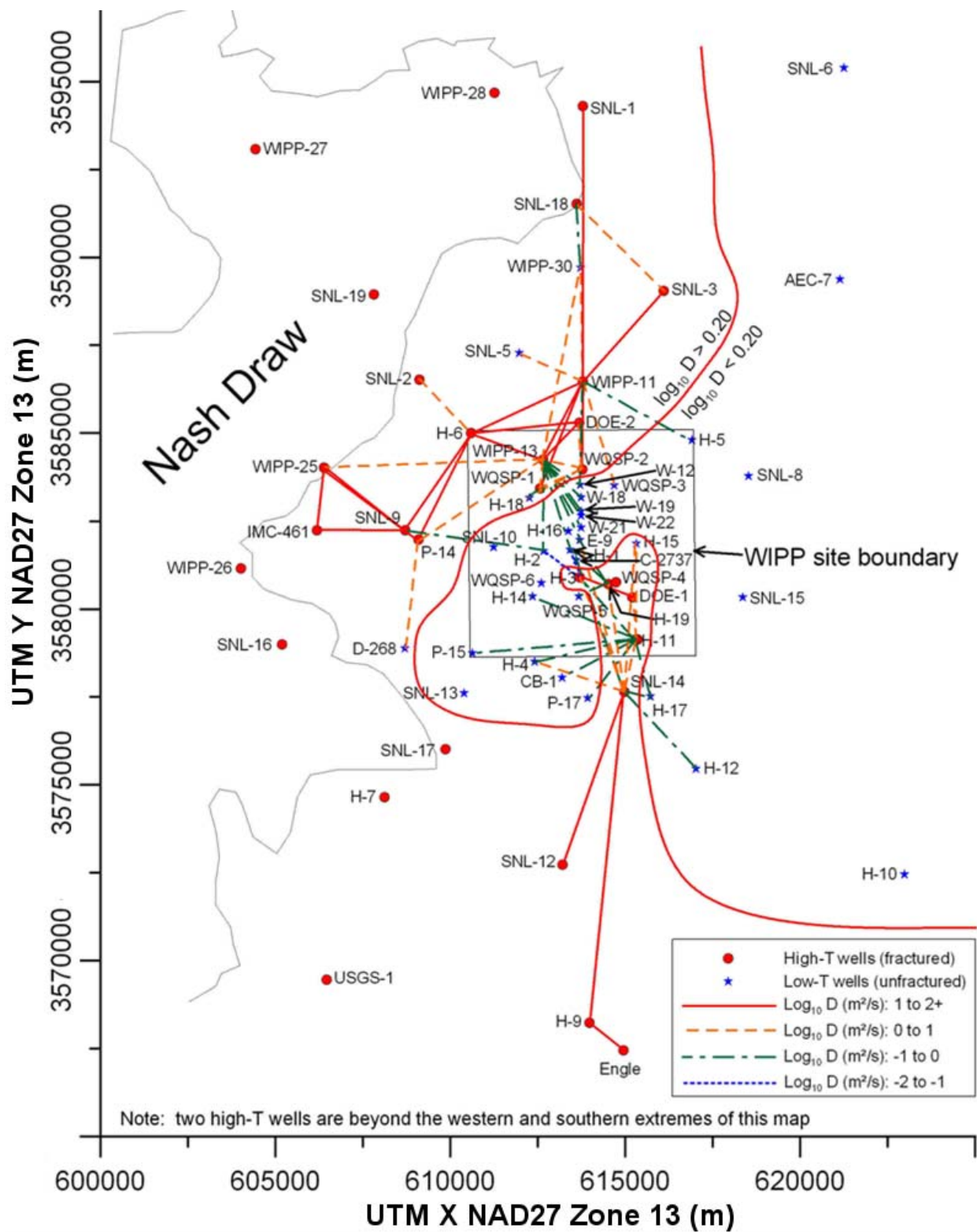
## 14 TFIELD-4.2.2 Gypsum Cements

15 In all cases where sufficient core and  $T$  estimates exist, wells with no gypsum (Figure TFIELD  
 16 2-12) have high  $T$ , due to well-interconnected fractures. To account for this relationship, cells  
 17 were assigned  $P_{\text{low}} = 0.05$  where no gypsum is present. As seen in Figure TFIELD 2-12, this is a  
 18 fairly large area. Rather than give all the cells in the area such a low  $P_{\text{low}}$  value, cells were  
 19 selected from a regular grid at 1300-m spacing to receive soft data assignments (Figure TFIELD

1 4-3). A grid of 1300-m spacing was chosen to provide sufficient definition of the boundaries  
2 without overwhelming the SISIM geostatistical simulation with too many samples. The size of  
3 the matrix decomposed by SISM during estimation is proportional to the number of samples  
4 considered at each estimation location.

5 It was observed that in all cases where sufficient core and  $T$  estimates exist, wells outside of the  
6 low-gypsum region (Figure TFIELD 4-3) have low  $T$  because fracture interconnectivity is  
7 limited by gypsum cements. In the indicator kriging, areas outside of the low-gypsum region  
8 were assigned  $P_{\text{low}} = 0.95$  to increase the likelihood of predicting low  $T$  in the simulation.

9 By definition, the areas of no-gypsum and high-gypsum content cannot overlap, therefore the  
10 high-gypsum data were sampled on the same grid used by the no-gypsum data. By using  
11 fractional likelihoods and sparse sampling, these soft data did not overwhelm the random  
12 sampling algorithm of SISIM and allowed for greater variation between base field realizations.  
13 The high/low-gypsum content map is shown in Figure TFIELD 2-13. The low-gypsum region  
14 was not sampled, since it overlapped the no-gypsum region. Instead, the high-gypsum region was  
15 used. The area of high gypsum directly north of the WIPP LWB was sampled at 300-m spacing,  
16 to compensate for the diffusivity soft data described in the next section and produce model  
17 results more similar to observed Culebra behavior during pumping tests.



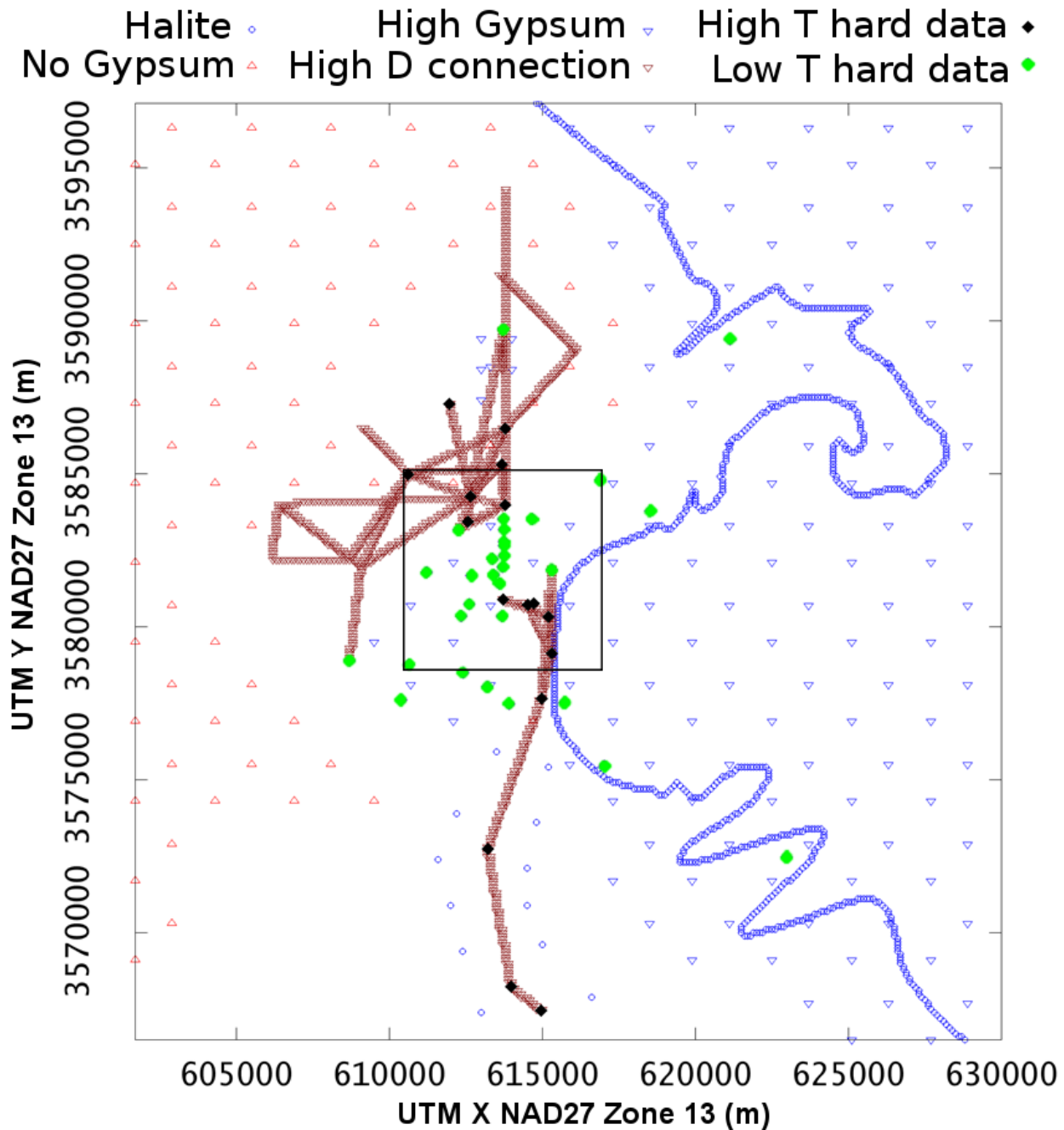


Figure TFIELD 4-3. Soft Data Points (Open Symbols) Generated During Step 2. Hard data points (filled symbols) are located at wells with single-well estimates of  $T$ . The black square is the WIPP LWB.

#### TFIELD-4.2.3 Diffusivity and Hydraulic Connections

Soft data were used to incorporate the degree of hydraulic connection observed between pairs of wells (pumping and observation wells) into the construction of the base fields. The diffusivity  $D$  ( $\text{m}^2/\text{s}$ ) associated with the pumping and observation well pair was calculated from the results of many hydraulic tests conducted at the WIPP site (Beauheim 2007). A map of these values is

1 shown in Figure TFIELD 4-2, showing colored lines connecting pumping and observation wells  
2 involved in the nine pumping tests used in T-field calibration (pumping/observation wells listed  
3 in Table TFIELD 5-2). The model cells falling on a straight line connecting two wells with a  
4 calculated  $\log_{10} D > 0.2$  (i.e., all red connecting lines and some orange dashed lines) were  
5 assigned  $P_{low} = 0.25$  to account for the increased likelihood a cell on the connecting line would  
6 be high  $T$  (inverted maroon triangles in Figure TFIELD 4-3). Using  $P_{low} = 0$  would have forced  
7 SISIM to create a direct path connecting two wells where a strong response to pumping was  
8 observed, and there is no geologic reason that these connections must be straight.

9 In addition to the high- $T$  connection lines, a set of low- $T$  points was placed roughly parallel to  
10 the SNL-14/SNL-12/H-9/Engle connection path to keep the high- $T$  connection relatively narrow  
11 (blue circles in south central portion of Figure TFIELD 4-3). These points were assigned a  $P_{low} =$   
12 1, to ensure they would impact the indicator kriging simulation. Pumping SNL-14 in 2005  
13 produced a strong response at H-9c nearly ten kilometers (km) to the south. During model  
14 development it was found the only way to recreate the observed response with the MODFLOW  
15 model was to incorporate a relatively narrow connecting zone of high  $T$ . Without adding some  
16 low- $T$  points along the flanks of this path, SISIM tended to create a wide high- $T$  area, which did  
17 not allow the drawdown response to propagate significantly from SNL-14 to H-9, as was  
18 observed. The observed response would be consistent with a narrow linear geological feature,  
19 which is difficult to simulate using the current MODFLOW model with 100-m grid spacing.  
20 These low- $T$  points did not force the simulation to create a narrow high- $T$  pathway in each  
21 realization, as many base fields still had large areas of high  $T$  that extend past these points. Fields  
22 generated with and without the narrow high- $T$  pathway were modified through the calibration  
23 process, which included the SNL-14 pumping test data as calibration targets. This exercise was  
24 performed in an attempt to improve the ability of the base  $T$  fields to match observed data, since  
25 this might lead to fewer PEST iterations and quicker calibration times.

#### 26 **TFIELD-4.2.4 Combined Soft Data**

27 The final combined soft data field is shown in Figure TFIELD 4-3. The soft data input files and  
28 calculation scripts are provided in Appendix B of Hart et al. (Hart et al. 2008).

29 Single-well estimates of  $T$  are hard data shown on the figure with filled diamonds (data listed in  
30 Table TFIELD 4-2). Hard data are combined here with soft data in base T-field creation, but  
31 appear again (without soft data) as fixed pilot points in the T-field calibration process (Section  
32 TFIELD-5.0). Filled green diamonds are wells with  $\log_{10} T$  estimates  $\leq -5.4$  ( $\text{m}^2/\text{s}$ ), and black  
33 filled diamonds are wells with  $\log_{10} T$  estimates  $> -5.4$  ( $\text{m}^2/\text{s}$ ).

34 The grid of inverted open blue triangles in the east indicate areas with “high gypsum” (white area  
35 in Figure TFIELD 2-13), while the grid of open red triangles in the west indicates areas with “no  
36 gypsum” (peach area in Figure TFIELD 2-12).

37 Lines of closely spaced inverted brown triangles represent the connections between pumping and  
38 observation wells interpreted with a  $\log_{10}$  diffusivity ( $D$ )  $> 0.2 \text{ m}^2/\text{s}$ , including all solid red and  
39 some dashed orange lines in Figure TFIELD 4-2.

1 The open blue circles (“Halite” in the figure legend) are used in two ways to enforce high  
 2 probability for low  $T$  in two different locations. The first use is the line of closely spaced open  
 3 blue circles corresponding to M2/H2 or M3/H3; locations east of this line have either halite  
 4 above or below the Culebra. This boundary marks the eastern edge of the random placement of  
 5 high- $T$  and low- $T$  zones (Zones 3 and 4 in Figure TFIELD 3-2). The second group, the open blue  
 6 circles straddling the line connecting Engle, H-9, SNL-12, and SNL-14 (running south to north  
 7 from the bottom middle of the figure), represents a low- $T$  zone added to increase the contrast of  
 8 the high- $T$  zone along this line of south-to-north connectors, to better represent results observed  
 9 in the SNL-14 multi-well pumping test.

## 10 **TFIELD-4.3 Step 3 – Indicator Variography**

11 The geostatistical indicator simulations done as part of the base T-field development are only  
 12 utilized in the central section of the model domain, between the Salado dissolution area to the  
 13 west and the low- $T$  halite-sandwiched region to the east. Therefore, only wells in this middle  
 14 section are used for construction of the indicator variogram. A total of 46 wells that provide  
 15 information regarding  $\log_{10} T$  were used in the calculation of the indicator variograms. The  
 16 indicator value is determined by comparing each  $\log_{10} T$  value to a threshold  $\log_{10} T$  value,  
 17  $T_t = -5.4$ ,

$$18 \quad I(x, y) = \begin{cases} 1 & \text{if } \log_{10} T < T_t \\ 0 & \text{if } \log_{10} T \geq T_t \end{cases} \quad (\text{TFIELD 4.2})$$

19 Where  $I(x, y)$  denotes the unitless indicator value at well location  $(x, y)$ . The experimental  
 20 indicator variogram was fit with a spherical variogram model, whose model parameters are given  
 21 in Table TFIELD 4-3. Figure TFIELD 4-4 illustrates the experimental and model indicator  
 22 variograms. The proportion of low- $T$  values in the data set is 0.652. The variance of an indicator  
 23 value is  $(1 - p)p$ , where  $p$  is the proportion of high or low values. The variance for these  
 24 indicator data is 0.227 and is used directly as the sill in the variogram modeling (dashed  
 25 horizontal line in Figure TFIELD 4-4). The parameters in Table TFIELD 4-3 are used as input to  
 26 the SISIM program for creation of the stochastic component of the base T-fields. In an attempt to  
 27 identify anisotropy, model variograms were calculated in both the NE-SW and NW-SE  
 28 directions (see Appendix C of Hart et al. (Hart et al. 2008)). These directional variograms  
 29 analyses were inconclusive, only omnidirectional (i.e., isotropic) variograms were used in the  
 30 final analysis.

31 **Table TFIELD 4-3. Variogram Parameters for Isotropic Fit to Indicator Data**  
 32 **Variogram. Omnidirectional variogram calculated with a lag**  
 33 **spacing of 500 m.**

Parameter	Value
Model Type	Spherical
Nugget	0.0
Sill	0.227
Range	2195 m

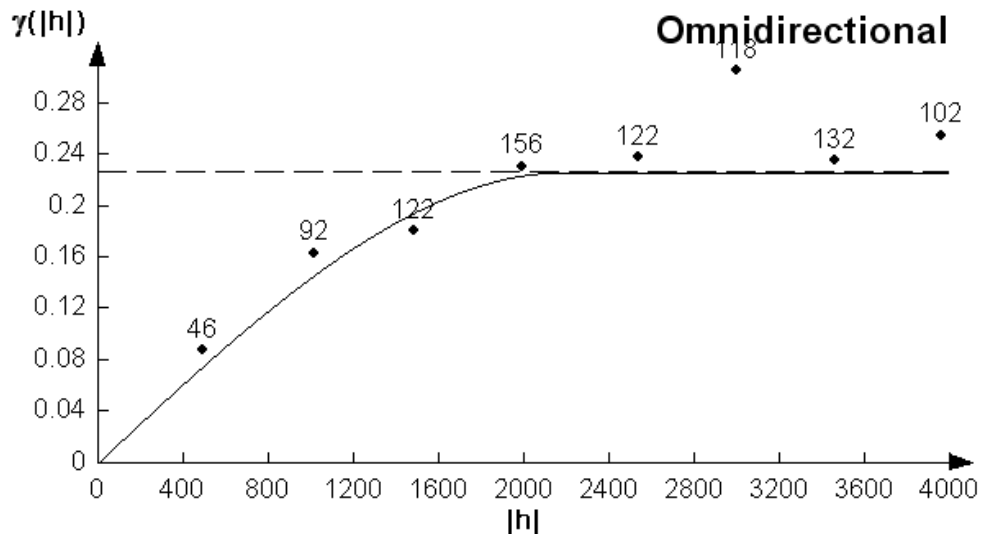


**Figure TFIELD 4-4. Experimental Variogram (Dots) and Spherical Model (Line) for Indicator Values. x-axis is lag distance [meters], y-axis is the unitless indicator; numbers by dots indicate the number of pairs represented at each lag.**

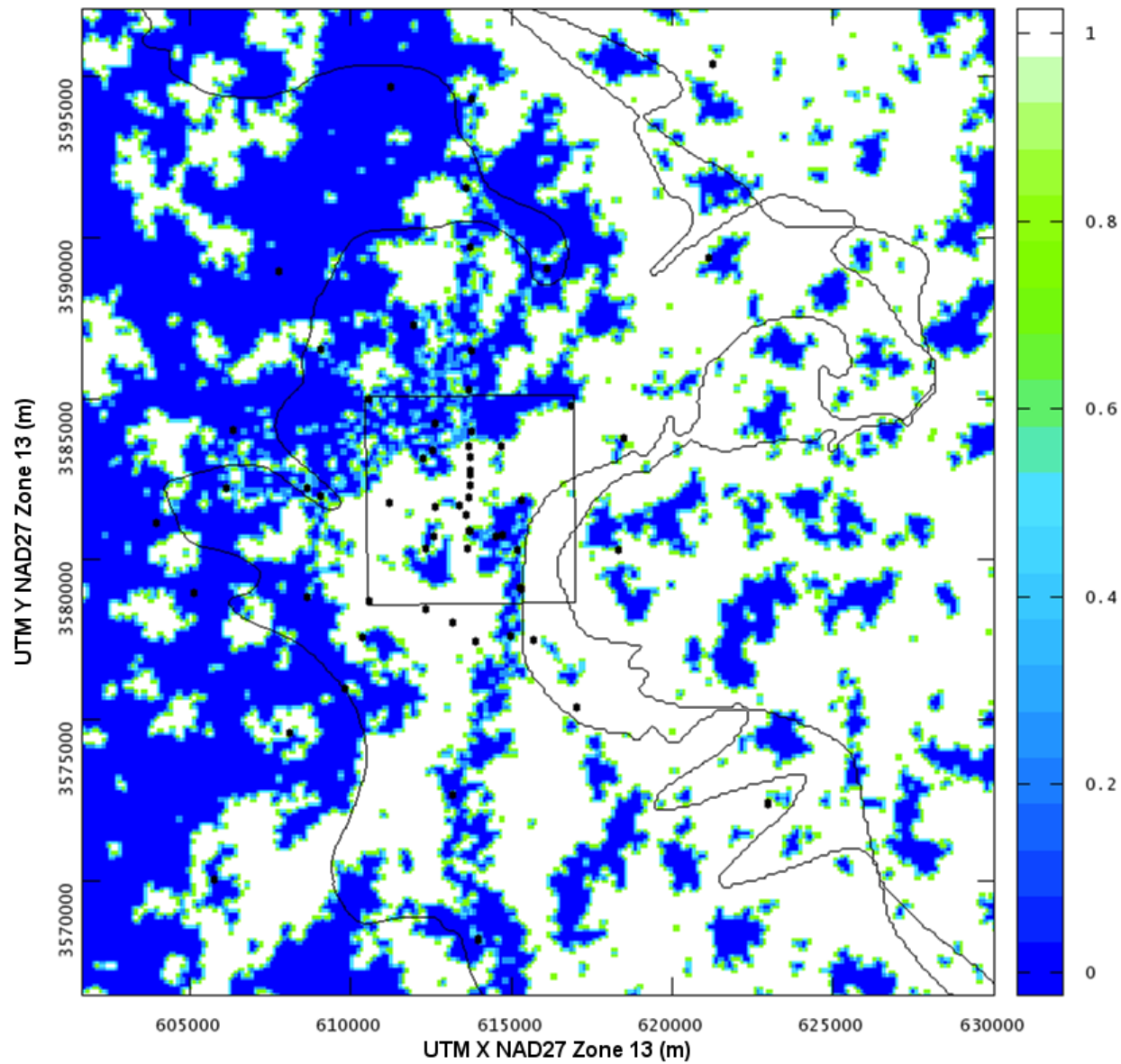
#### TFIELD-4.4 Step 4 – Conditional Indicator Simulation

With previous sections describing the indicator variogram model, hard  $T$  data values, and soft geologic and hydrologic data, stochastic realizations of high- $T$  zones were constructed using the GSLIB program SISIM (Deutsch and Journel 1998). An example indicator field is given in Figure TFIELD 4-5. Maps summarizing statistics for the 1,000 resulting base T-fields are presented in Figure TFIELD 4-6 and Figure TFIELD 4-7. These figures show the impact the conditioning information had on the overall fields. The combined M2/H2 and M3/H3 margins have a standard deviation of 0 and are constant at the proper value as desired. Areas designated as higher likelihood of high  $T$  do show an average value that trends towards the high- $T$  value (in this case, 0), but they still have a standard deviation that is non-zero, indicating that there is some variability in those areas. The same is true in areas outside the low-gypsum region. Additionally, areas with no conditioning information have higher standard deviations, indicating that high- $T$  zone placement in those locations was allowed to be fully variable. Though there are some visible artifacts from the grids used in the average and standard deviation fields (locations of soft data points in Figure TFIELD 4-3 are discernible in Figure TFIELD 4-6 and Figure TFIELD 4-7), the individual realizations, such as Figure TFIELD 4-5, do not show these artifacts. Additionally, the majority of the artifacts occur outside the central zone, which is the only place the indicator fields are used. The indicator fields created by this process are the best possible combination of hydraulic and geologic conditioning given current data.

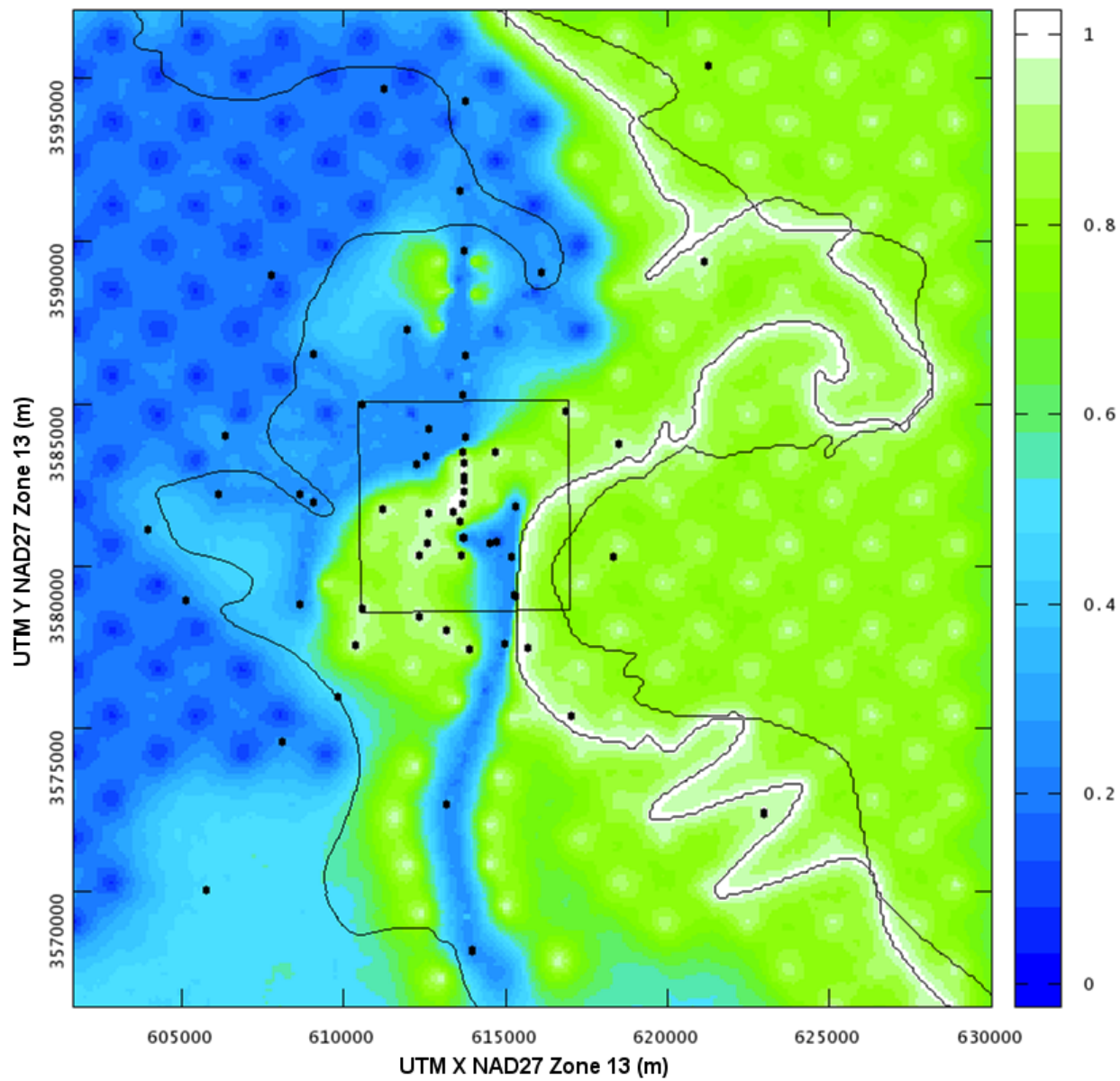
There is a relatively high density of hard data available inside the WIPP LWB, which significantly constrains the estimation process there. Geostatistical simulation is most useful to fill in large gaps near the edges of the model domain where a small number of observations exist. It must also be considered that these base-T fields are just a first guess for the model calibration

1 process, which utilizes the single-well  $T$  and both the steady-state and multi-well pumping test  
2 drawdown data as calibration targets. Ultimately, these data drive the calibration, adjusting input  
3 parameters to better match observed data. See Section TFIELD-5.4 for figures and discussion  
4 illustrating the extent to which the input fields were adjusted to match the data (e.g., see Figure  
5 TFIELD 5-19).

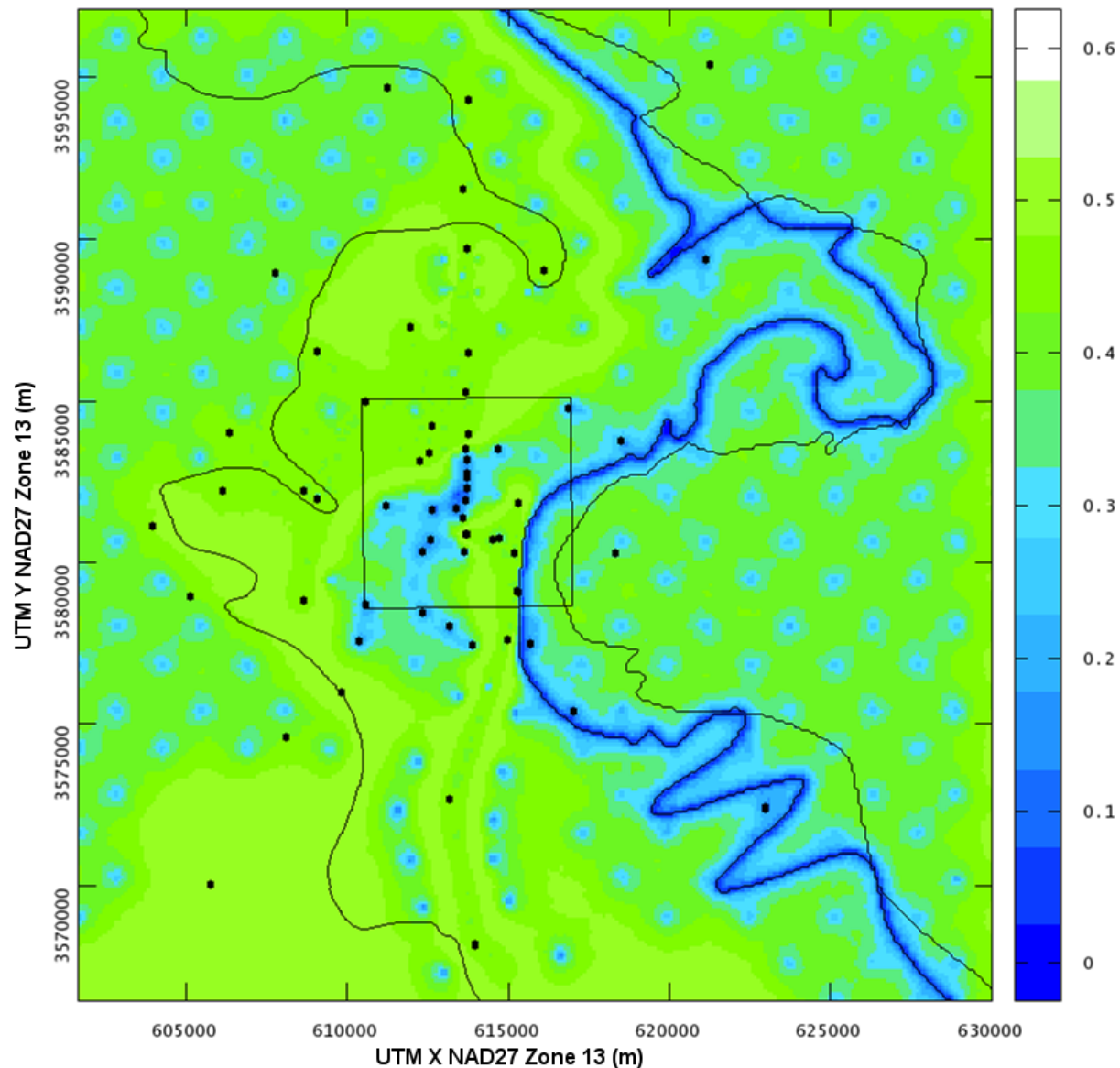
6

7  
8  
9

**Figure TFIELD 4-5. Sample Indicator Field for Realization r123. 1 indicates low  $T$  and 0 indicates high  $T$ .**



1      **Figure TFIELD 4-6.      Average Indicator Values Across All 1000 Base Realizations. 1**  
2      **3**      indicates low  $T$  and 0 indicates high  $T$ .



1  
2 **Figure TFIELD 4-7. Standard Deviation of Indicator Values Across All 1000 Base**  
3 **Realizations**

4 **TFIELD-4.5 Step 5 – Construction of Transmissivity Fields**

5 Once the indicator fields were created, the  $T$  values were assigned using Equation TFIELD 4.1  
6 using a Perl script. Equation TFIELD 4.3 was used to calculate  $Y = \log_{10} T$  at each cell,

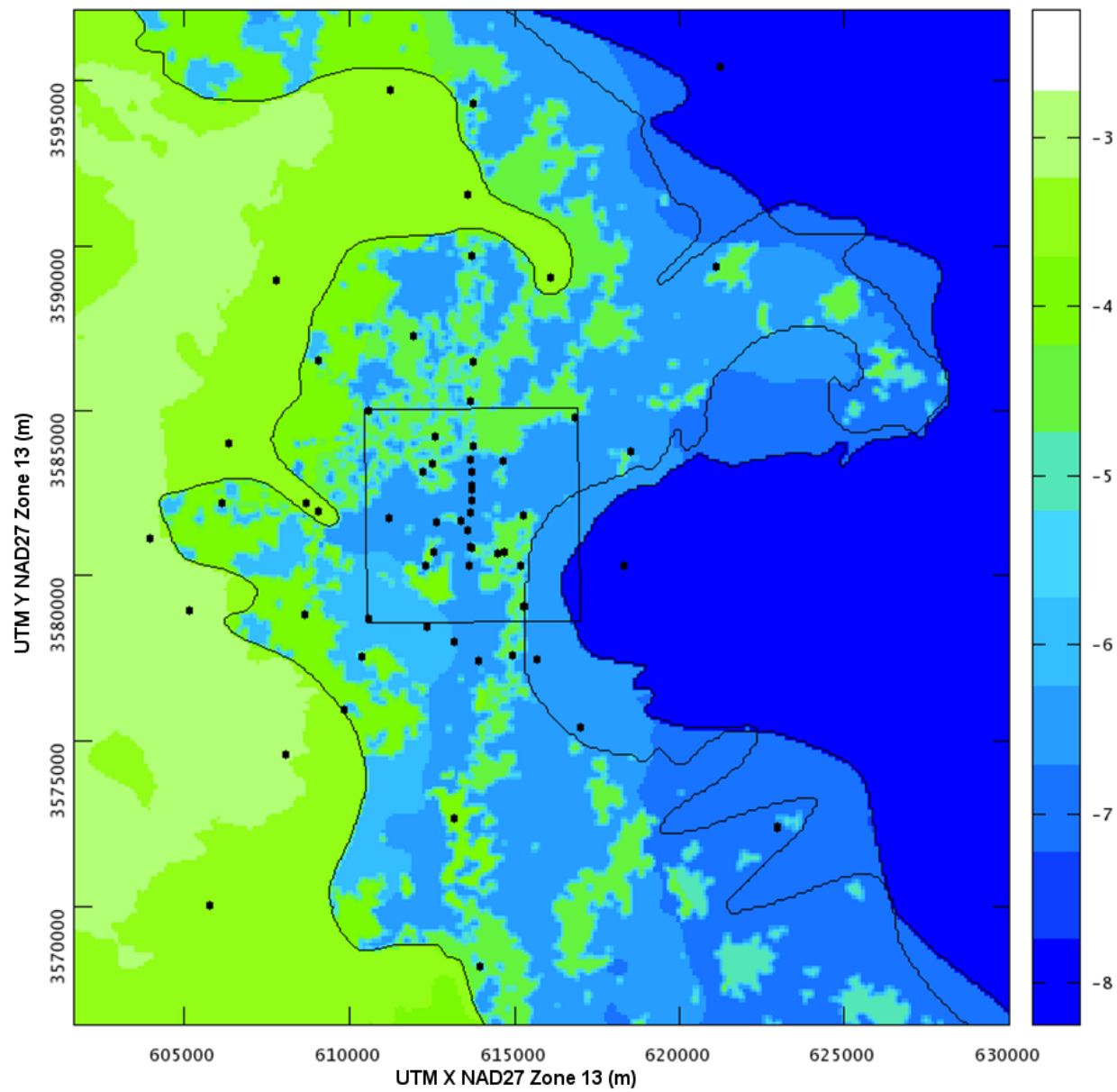
7 
$$Y(x,y) = \mathbf{b}[Z(x,y)] + \mathbf{a}[Z(x,y)] d(x,y) \quad (\text{TFIELD 4.3})$$

8 where  $\mathbf{b}$  and  $\mathbf{a}$  represent combinations of the  $\beta$ -coefficient based on the zone ( $Z(x,y)$ ) of the cell.  
9 Table TFIELD 4-4 shows how the variables in the original linear regression equation (Equation  
10 TFIELD 4.1) were related to Equation TFIELD 4.3. Figure TFIELD 3-2 shows the indicator  
11 zone distribution.

1 **Table TFIELD 4-4. Correlation of  $\beta$  and  $I$  Values from Equation TFIELD 4.1 to  $a$  and  $b$**   
 2 **Values in Equation TFIELD 4.3**

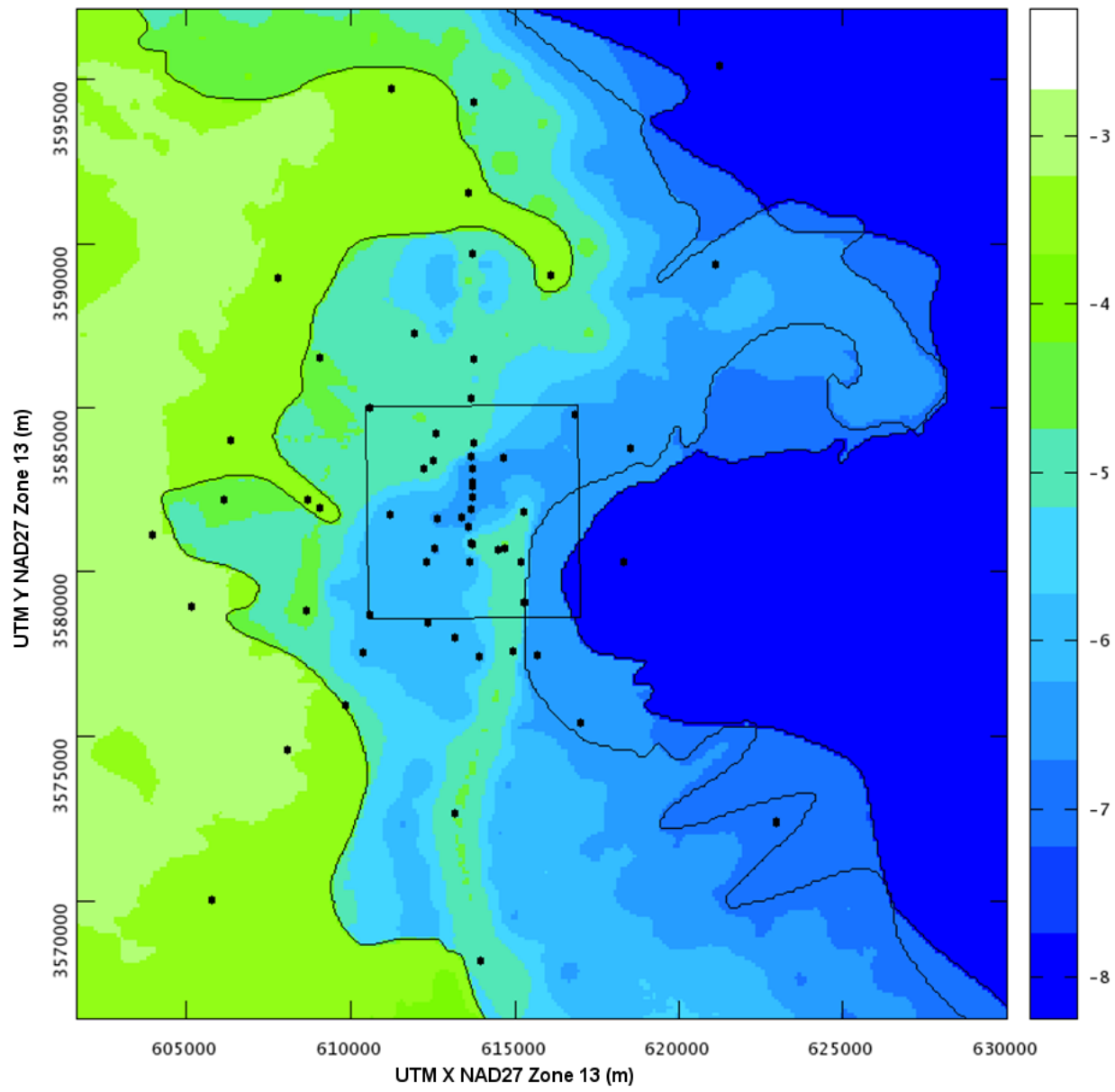
	<b>Zone 0</b> <i>Salado</i>	<b>Zone 1</b> <i>Halite 2</i>	<b>Zone 2</b> <i>Halite</i>	<b>Zone 3</b> <i>Central low T</i>	<b>Zone 4</b> <i>Central high T</i>
$I_f$	1	0	0	0	1
$I_D$	1	0	0	0	0
$I_H$	0	1	0	0	0
$I_h$	0	1	1	0	0
<b><math>b</math></b>	$\beta_1 + \beta_3 + \beta_4$	$\beta_1 + \beta_5$	$\beta_1$	$\beta_1$	$\beta_1 + \beta_3$
<b><math>a</math></b>	$\beta_2$	$\beta_2$	$\beta_2$	$\beta_2$	$\beta_2$

3  
 4 The Perl script was executed on all 1,000 realizations. A sample final base  $T$  field is presented in  
 5 Figure TFIELD 4-8 for realization r123 (a random representative selection from the possible  
 6 fields). The mean  $\log_{10} T$ -field across all 1,000 realizations is presented in Figure TFIELD 4-9.  
 7 The standard deviation of  $\log_{10} T$  is presented in Figure TFIELD 4-10. Very low standard  
 8 deviation occurs across the 1000 base realizations outside the stochastically sampled areas,  
 9 including the higher  $T$  areas to the west and the lower  $T$  areas to the east (Figure TFIELD 4-10).  
 10 These stochastically sampled areas are the main source of variability between the 1000 base  
 11 realizations. The variability of the indicator variable across the realizations (Figure TFIELD 4-7)  
 12 is one component of the variability observed in the final  $T$  values in the base  $T$  fields (plotted  
 13 normalized to the range {0,1} in Figure TFIELD 4-10). The regression analysis produced  
 14 variability in the predicted  $T$  values in a zone related to the variability in the overburden  
 15 thickness.



1  
2

**Figure TFIELD 4-8. Sample  $\text{Log}_{10} T$  (m<sup>2</sup>/s) Base Field Realization r123**



1

2 **Figure TFIELD 4-9. Mean  $\text{Log}_{10} T$  (m<sup>2</sup>/s) Values Across All 1000 Base Realizations**

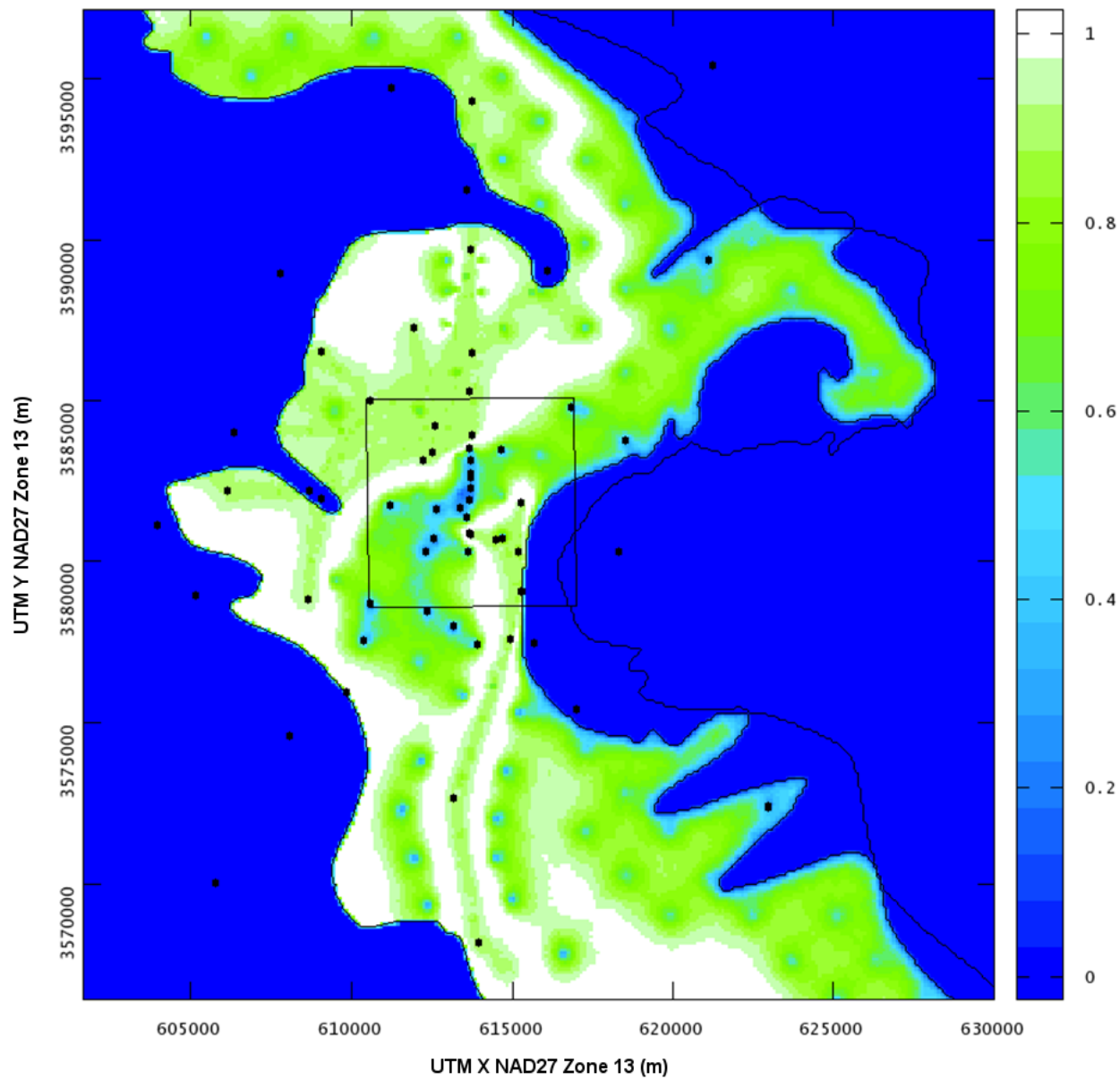


**Figure TFIELD 4-10. Normalized Standard Deviation of  $\log_{10} T$  ( $\text{m}^2/\text{s}$ ) Values Across All 1000 Base Realizations**

## 1 TFIELD-5.0 T-Field Calibration

2 The work outlined in Section TFIELD-5.0 was performed under AP-114, Analysis Plan for  
3 Evaluation and Recalibration of Culebra T Fields (Beauheim 2008). The calibration of the T-  
4 fields used 200 of the 1,000 base fields from the results of AP-114 Task 5 (Hart et al. 2008,  
5 summarized in Section TFIELD-4.0) as starting points for the calibration process. More than 200  
6 fields could not be calibrated, due to time constraints. Calibration is the process of systematically  
7 adjusting the input parameters to the MODFLOW model (fields of  $T$ ,  $A$ ,  $S$ , and  $R$ ) to reduce the  
8 sum of the squared differences between field observations and MODFLOW model output  
9 (steady-state and transient head).

10 The pilot point calibration method was implemented using the parameter estimation software  
11 PEST. Automatic model calibration was utilized to make the process more easily documentable  
12 and reproducible, compared to manual calibration (i.e., trial and error). The MODFLOW model  
13 used to simulate groundwater flow through the Culebra contains a large number of active model  
14 cells for  $T$ ,  $A$ , and  $S$  fields. Estimating each model element independently would require  
15 estimating hundreds of thousands of unknown parameters. The pilot point approach makes the  
16 calibration process more tractable by lowering the number of parameters to estimate. Instead of  
17 estimating each parameter in each model cell independently, parameter values are estimated at  
18 strategically placed pilot point locations. Parameter values at each model cell are then  
19 interpolated from the pilot points using kriging as a pre-processing step between parameter  
20 assignment by PEST and MODFLOW model execution. The pilot point approach allows mixing  
21 estimated and fixed pilot points (e.g.,  $T$  pilot points at wells with single-well hydraulic test  
22 estimates of  $T$ ). The pilot point approach was also used in CRA-2004 PABC and a variant of it  
23 was used (without PEST) in the CCA. Both steady-state and transient head calibration targets are  
24 discussed in Section TFIELD-5.1. The parameter zones, pilot point locations for each parameter,  
25 initial conditions, and boundary conditions are specified in Section TFIELD-5.2. The  
26 components of the MODFLOW model used with PEST, and the utilities required to pre-process  
27 and post-process the inputs and outputs from the model during the calibration are discussed in  
28 Section TFIELD-5.3. Finally, some post-calibration analysis of the results is presented in Section  
29 TFIELD-5.4.

30 The initial  $T$  values at pilot points were taken from the base fields. In addition to  $T$ , the horizontal  
31  $T$  anisotropy ( $A$ ), the storativity ( $S$ ), and a linear section of recharge ( $R$ ) were also calibrated. The  
32 same zone definitions used for developing the base  $T$  fields (see TFIELD-4.0) were used for  $T$   
33 pilot points (although zone numbers changed), and similar zone definitions were used for  
34 anisotropy. Zones for storativity and recharge were based on other analyses completed in the  
35 area surrounding the WIPP site (see Section TFIELD-5.2.1). Pilot points were selected for each  
36 parameter and initial values were selected that were consistent with the conceptual model used to  
37 create the base fields (see Section TFIELD-5.2.2 and Section TFIELD-5.2.7).

38 A model variogram for  $T$  was created using the estimated  $T$  from single-well hydraulic tests. This  
39 variogram was also used for all parameters, as it was the only one that could be created from  
40 field data (see Section TFIELD-5.2.8). This variogram was used to create kriging factors that  
41 were then used to create continuous fields from the pilot point values. The  $T$ ,  $A$ ,  $S$ , and  $R$  fields  
42 were then used as inputs to the MODFLOW numerical model to produce simulated head and  
43 drawdown results (see Section TFIELD-5.2.10).

1 Once the MODFLOW models produced simulated drawdown and head results, the modeled  
2 results were compared to the field data for the tests that were modeled. The residual of an  
3 observation is calculated in PEST as the weighted difference between measured and modeled  
4 data. Observation weights were selected to make the sum of the weighted steady-state head  
5 errors approximately equal to the sum of errors of four observation wells in a transient pumping  
6 test to approximately balance the steady-state and transient model-to-data misfits. The PEST  
7 optimization uses a single objective function, which is the sum of the steady-state and transient  
8 residuals. Because the improvement of model fit for steady-state heads might come at the  
9 expense of fit to transient pumping tests, a decision was made to balance the importance of the  
10 two groups in the calibration effort. The residuals were used by PEST to construct a finite-  
11 difference approximation of the Jacobian matrix. The Jacobian matrix is a measure of the  
12 sensitivity each model prediction has to each adjustable parameter, and is used to optimize the  
13 pilot point parameter values. The goal of the optimization is to minimize the objective function  
14 value, a measure of the misfit between model predictions and observed data (see Section  
15 TFIELD-5.2.9).

16 Because traditional construction of the Jacobian matrix requires at least  $N_p + 1$  forward model  
17 calls ( $N_p$  parameters estimated in the calibration), using 1,100-plus parameters would be  
18 impossible without additional efficiency in the optimization. The PEST singular value  
19 decomposition (SVD) assist approach reduces the size of the Jacobian matrix by only using the  
20 most significant "super-parameters" that correspond to the eigenvectors with the largest singular  
21 values, estimated using the SVD of the Jacobian matrix. The SVD process required initial  
22 calculation of a full Jacobian matrix, but then reduced the subsequent number of required  
23 forward calls by a factor of four to six. The result was that three calls to PEST were required to  
24 calibrate the fields (see Figure TFIELD 5-1):

- 25 1. a single full Jacobian calculation, which required 1,100+ forward model calls;
- 26 2. an SVD calibration using the reduced parameter set that ran up to 50 iterations, requiring  
27 between 100 and 400 forward model calls per iteration; and
- 28 3. a final PEST run with the best parameter results to create the final fields corresponding to  
29 the best parameter values calculated during the SVD-assisted calibration.

30 Total calibration time for a single base field was approximately seven days using six processors  
31 (one master node and five slave nodes).

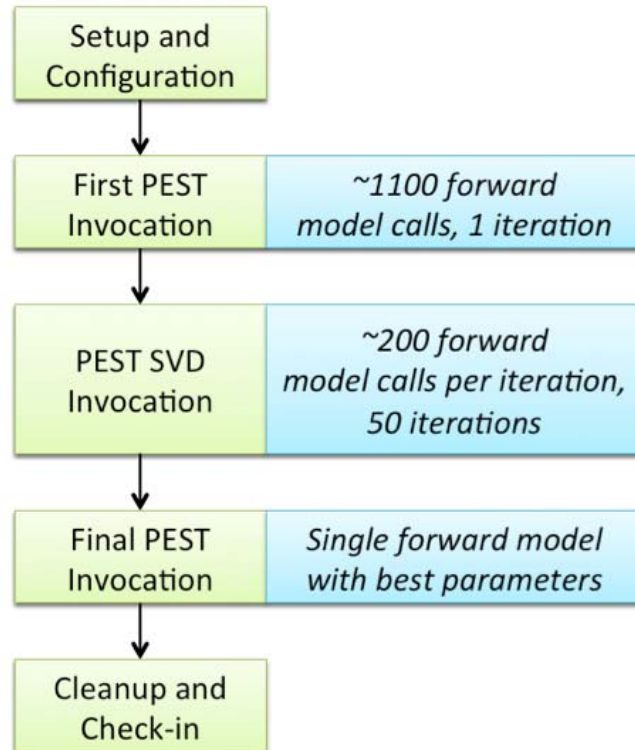


**Figure TFIELD 5-1. Complete Calibration Process for a Single Realization**

3 After approximately 140 fields had been calibrated, a few steady-state calibration targets were  
 4 found to be incorrect by several meters. A total of 150 fields were calibrated using the incorrect  
 5 targets, and an additional 50 fields were started using the corrected heads (Beauheim 2009;  
 6 Johnson 2009a and Johnson 2009b). To deal with the incorrect values, a limited recalibration  
 7 was performed on the results of the first 150 calibrations (see Section TFIELD-5.3.2). The same  
 8 process that has been described was followed for the limited secondary calibration, but since the  
 9 initial parameter values were taken from the calibrated results, only the necessary pilot point  
 10 locations near the updated steady-state head values were allowed to be changed, and the SVD  
 11 portion of the PEST recalibration was limited to 10 iterations. The end result was 200 fields, with  
 12 150 of these fields having undergone a secondary calibration to incorporate corrected field  
 13 observation data. The impact of this change is discussed in Section TFIELD-5.3.3.

14 The end result of the calibration was the first 200 of the original 1,000 field sets ( $T$ ,  $A$ ,  $S$ , and  $R$ )  
15 calibrated to one set of steady-state heads and nine transient, multi-observation well pumping  
16 tests. More than 200 of the 1,000 base  $T$ -fields could not be calibrated due to time constraints  
17 associated with the calibration effort. Since the 1,000 base  $T$ -fields were generated randomly, the  
18 first 200 were in effect a random sample. The 100 best-calibrated fields (those with the smallest  
19 residuals) were selected as the final results from this task (see Section TFIELD-5.3.4). Several  
20 statistical analyses were performed on the fields themselves to generate average values and  
21 variances in the field results (Section TFIELD-5.4.1).

22 The complete calibrations were performed under quality-assurance run control with inputs and  
23 outputs stored in a version control repository on a central server. The calibrations required

1 approximately six months of continuous runtime on a total of 80 processors. See Hart et al. (Hart  
2 et al. 2009) for details.

3 **TFIELD-5.1 Model Calibration Targets**

4 Two sets of head values were used for calibration of the Culebra flow model. The first dataset  
5 consists of 42 freshwater head values measured in May 2007, which were used as steady-state  
6 calibration targets (see Table TFIELD 5-1 for values used and see Johnson (Johnson 2009a and  
7 Johnson 2009b) for details). Appendix HYDRO-2014 shows the behavior of water levels in  
8 wells since 2007. The data in Appendix HYDRO-2014 support the continued use of 2007 water  
9 levels to represent steady-state conditions at the WIPP up to the CRA-2014 (see additional  
10 discussion in Appendix HYDRO-2014). The second dataset consists of drawdown data collected  
11 during 9 independent multi-well pumping tests conducted over a span of more than 20 years (see  
12 Table TFIELD 5-2 for lists of observation wells and relevant references).

13 The steady-state MODFLOW simulation is calibrated against data in Table TFIELD 5-1. Each of  
14 the nine transient pumping tests in Table TFIELD 5-2 are simulated as a separate MODFLOW  
15 model simulation. A “single” forward model run actually involved 10 individual MODFLOW  
16 simulations (1 steady-state and 9 transient simulations), each using the same input parameter  
17 fields, but different pumping configurations. Some wells appeared in multiple pumping tests  
18 (e.g., H-15, H-18, or ERDA-9). These wells had calibration targets associated with multiple  
19 transient forward simulations. The MODFLOW model is discussed more in Section TFIELD-  
20 5.2.10.

21 SNL-6 and SNL-15 are listed as steady-state targets in Table TFIELD 5-1, but they are located in  
22 the constant-head portion of the model domain and therefore their corresponding model-  
23 predicted values are not adjustable through changes in the *T* field.

1                   **Table TFIELD 5-1. Freshwater Head Observations Used as Steady-state Calibration**  
 2                   **Targets**

Well Name	May 2007 head target (m AMSL)
C-2737	921.23
ERDA-9	924.88
H-2b2	929.62
H-3b2	918.68
H-4b	916.34
H-5b	939.12
H-6b	936.44
H-7b1	914.58
H-9c	912.8
H-10c	922.02
H-11b4	917.09
H-12	916.53
H-15	920.32
H-17	916.24
H-19b0	918.84
IMC-461	928.95
SNL-1	941.86
SNL-2	937.65
SNL-3	939.81
SNL-5	938.59
SNL-6	1110
SNL-8	929.94
SNL-9	932.05
SNL-10	931.54
SNL-12	915.24
SNL-13	918.19
SNL-14	916.33
SNL-15	1060
SNL-16	918.68
SNL-17A	916.78
SNL-18	939.87
SNL-19	937.58
USGS-4	911.11
WIPP-11	940.65
WIPP-13	939.78
WIPP-19	933.66
WIPP-25	937.57
WIPP-30	939.37
WQSP-1	938.28
WQSP-2	939.87
WQSP-3	936.43
WQSP-4	919.5
WQSP-5	918.18
WQSP-6	921.96

1      **Table TFIELD 5-2. Summary of Transient Observations Used as Calibration Targets**

Pumping Well(s)	Observation Wells <sup>1</sup>	Total # obs.	Reference
WQSP-2	H-18, DOE-2, WQSP-1, WIPP-13	77	Beauheim and Ruskauff 1998
H-19 and H-11	WQSP-5, H-1, H-15, DOE-1, ERDA-9, WIPP-21, H-3b2	143	Beauheim and Ruskauff 1998
WQSP-1	H-18, WIPP-13	36	Beauheim and Ruskauff 1998
WIPP-11	WQSP-2, WQSP-3, WIPP-12, SNL-9, SNL-5, H-6b, SNL-3, SNL-2, SNL-1, WIPP-30, WQSP-1, WIPP-13	250	Toll and Johnson 2006b; Roberts 2006
H-11	H-4b, H-12, H-14, H-15, H-17, DOE-1, CB-1, P-15, P-17, H-3b2	130	Beauheim 1989
WIPP-13	WIPP-19, WIPP-18, H-2b2, H-6b, WIPP-12, WIPP-25, DOE-2, WIPP-30, P-14	167	Beauheim 1987b
SNL-14	H-9c, H-4b, SNL-13, SNL-12, H-15, H-17, C-2737, ERDA-9, H-19b0, H-3b2, H-7, H-11b4	252	Toll and Johnson 2006a; Roberts 2006
P-14	D-268, H-18, WIPP-26, H-6b, WIPP-25	82	Beauheim and Ruskauff 1998
H-3	DOE-1, H-2b2, H-1, H-11b2	69	Beauheim 1987a

<sup>1</sup> See Figure TFIELD 4-2 for locations of pumping and observation wells and diffusivity values estimated from pumping tests.

2

3      **TFIELD-5.2 Step 1 – Calibration Setup and Configuration**

4      This step comprised the setup and configuration processes that were the same for every  
5      calibrated base field. Step 1 included the creation and definition of zones for each of the  
6      parameters and the selection of pilot point locations and initial values. Because of the stochastic  
7      nature of the transmissivity fields, unique zones are associated with each field, as defined in Hart  
8      et al. (Hart et al. 2008). The process to set up each field was the same, but certain elements, such  
9      as the exact number of pilot point locations used, were unique to each field.

10     The model domain and extent are identical to the domain defined in Section TFIELD-3.1. The  
11     base T-fields were taken from the results of Section TFIELD-4.5. Some model input files were  
12     created statically, and were used for every calibration. Some model input files were created  
13     dynamically for each calibration, but used the same variables and parameters in their creation.

14     **TFIELD-5.2.1 Creation of Parameter Zones**

15     Parameter zones were defined for each of the calibrated parameters. These zones or regions were  
16     defined to be consistent with the conceptual model for Culebra flow defined in Hart et al. (Hart  
17     et al. 2008) and summarized in Section TFIELD-3.0. The parameter zones were chosen to  
18     organize common pilot points groups together in the PEST calibration. Numerical values of  
19     parameter zones (i.e., zone numbers) are often different from those used in the conceptual model.

1 Figure TFIELD 2-8 shows the different margins that define geologic zones and the locations of  
2 the Culebra wells that have been drilled in the vicinity of the WIPP.

3 **TFIELD-5.2.1.1 Transmissivity Zones**

4 The  $T$  zones were defined to be consistent with the zones used in the geologic model and soft  
5 data analysis (Section TFIELD-4.2). As shown in Figure TFIELD 5-2, a high- $T$  zone exists to the  
6 west (zone 2), corresponding to the area of Salado dissolution, and a mixture of higher and lower  
7  $T$  values corresponding to the stochastic zones (zone 0 and 1) provided in the base fields defined  
8 the center of the model domain. Unlike AP-114 Task 5 (Section TFIELD-4.5), where it was a  
9 separate zone, the area between the H2/M2 and H3/M3 margins (green in Figure TFIELD 5-2)  
10 was included in the same zone (zone 1) as the lower  $T$  stochastic areas provided by the base  
11 fields. The area east of both the H2/M2 and H3/M3 margins – where the Culebra is bounded both  
12 above and below by halite-cemented elements – was defined to be its own zone (zone 3), as was  
13 done in AP-114 Task 5. A no-flow boundary roughly follows the axis of Nash Draw defining the  
14 final region (zone 4), which is inactive and applies to all parameters.

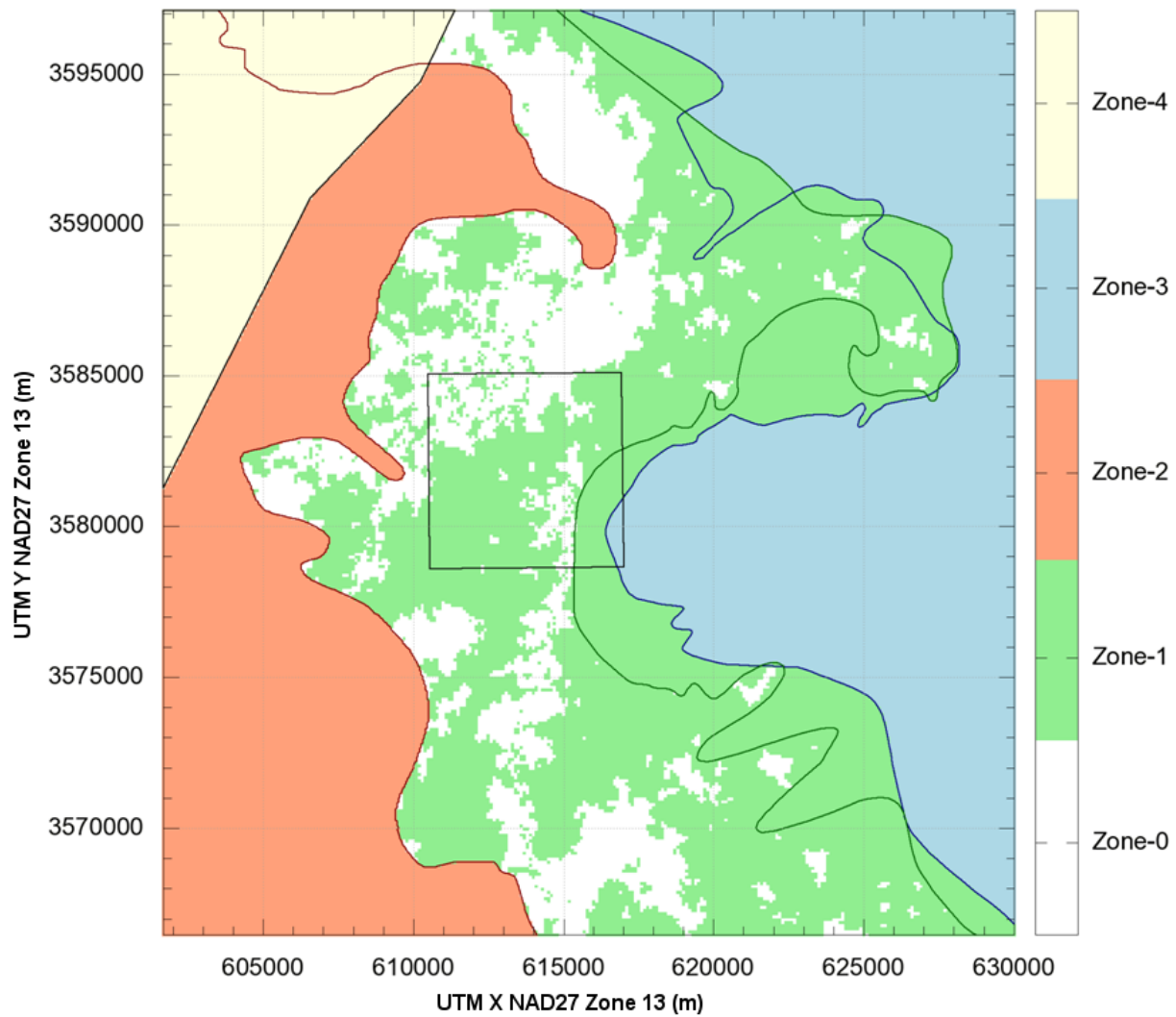


**Figure TFIELD 5-2. Transmissivity Zone Map for a Single Realization. Zones 0 and 1 are the stochastic zones created in Hart et al. (2008); Zone 2 is the high- $T$  Salado dissolution area; Zone 3 is the very low- $T$  halite-bounded area; Zone 4 is the northwestern inactive area.**

### TFIELD-5.2.1.2 Horizontal Anisotropy Zones

The  $T$  anisotropy field used the same zones defined for  $T$ . The  $T$  values in the north-south ( $y$ ) direction were calculated by multiplying the transmissivity value for the east-west ( $x$ ) direction (given in the T-field) by the anisotropy value ( $A$ ) at a given cell

$$T_{NS} = T_{EW} A. \quad (\text{TFIELD 5.1})$$

The map shown in Figure TFIELD 5-2 represents the zonation used for both  $A$  and  $T$ .

1 **TFIELD-5.2.1.3 Storativity Zones**

2 Besides the no-flow area (zone 4), four zones were defined for storativity estimation. The  
3 westernmost region (zone 2) is unconfined, as described in Powers et al. (Powers et al. 2006)  
4 (summarized in Section TFIELD-2.3.2). The largest area (zone 0) is fully confined, with its  
5 western boundary roughly following the Salado dissolution margin. The area between these two  
6 regions (zone 1) is the transition zone, where the Culebra is uncertainly confined. As with the  $T$   
7 and  $A$  zones, the area east of both the H2/M2 and H3/M3 margins is a separate region (zone 3),  
8 but in this case storativity is simply held constant at the initial confined-zone value. A map of the  
9 storativity zones is shown in Figure TFIELD 5-3.

10 The unconfined zone was implemented as a zone of high confined storativity to simplify the  
11 numerical model by approximating the non-linear unconfined problem with a linear storativity  
12 one. By defining a much higher storativity value in the unconfined part of the domain,  
13 unconfined behavior can be approximately modeled using a confined numerical model, which is  
14 linear and executes quicker than the unconfined non-linear model. Since the unconfined or  
15 transition zone does not exist inside the WIPP LWB, this choice has little impact on  
16 interpretation of transient hydraulic tests there, and this choice has no impact on steady-state  
17 flow simulations ( $S$  is only used in transient simulations) used to predict radionuclide transport in  
18 PA.

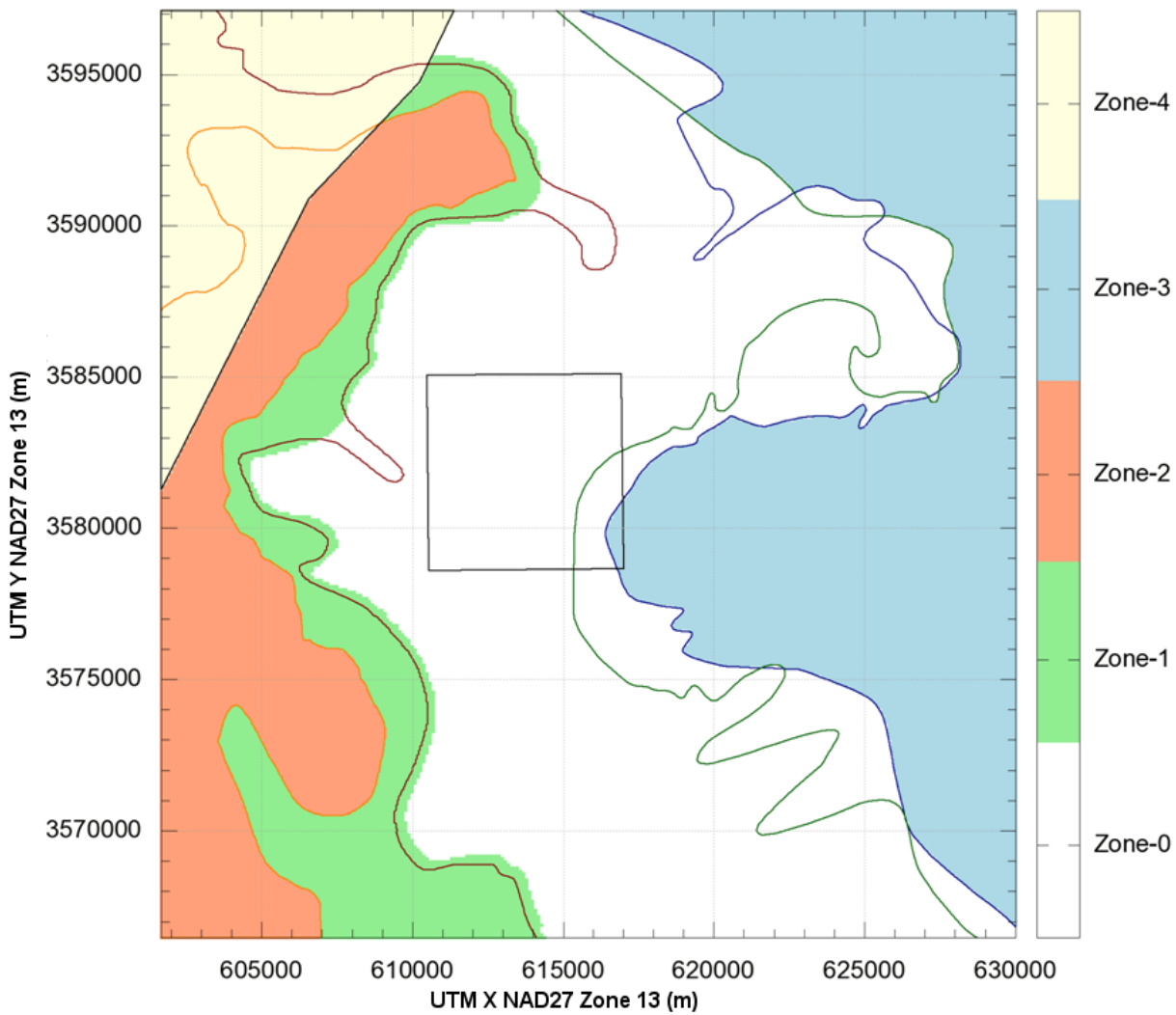
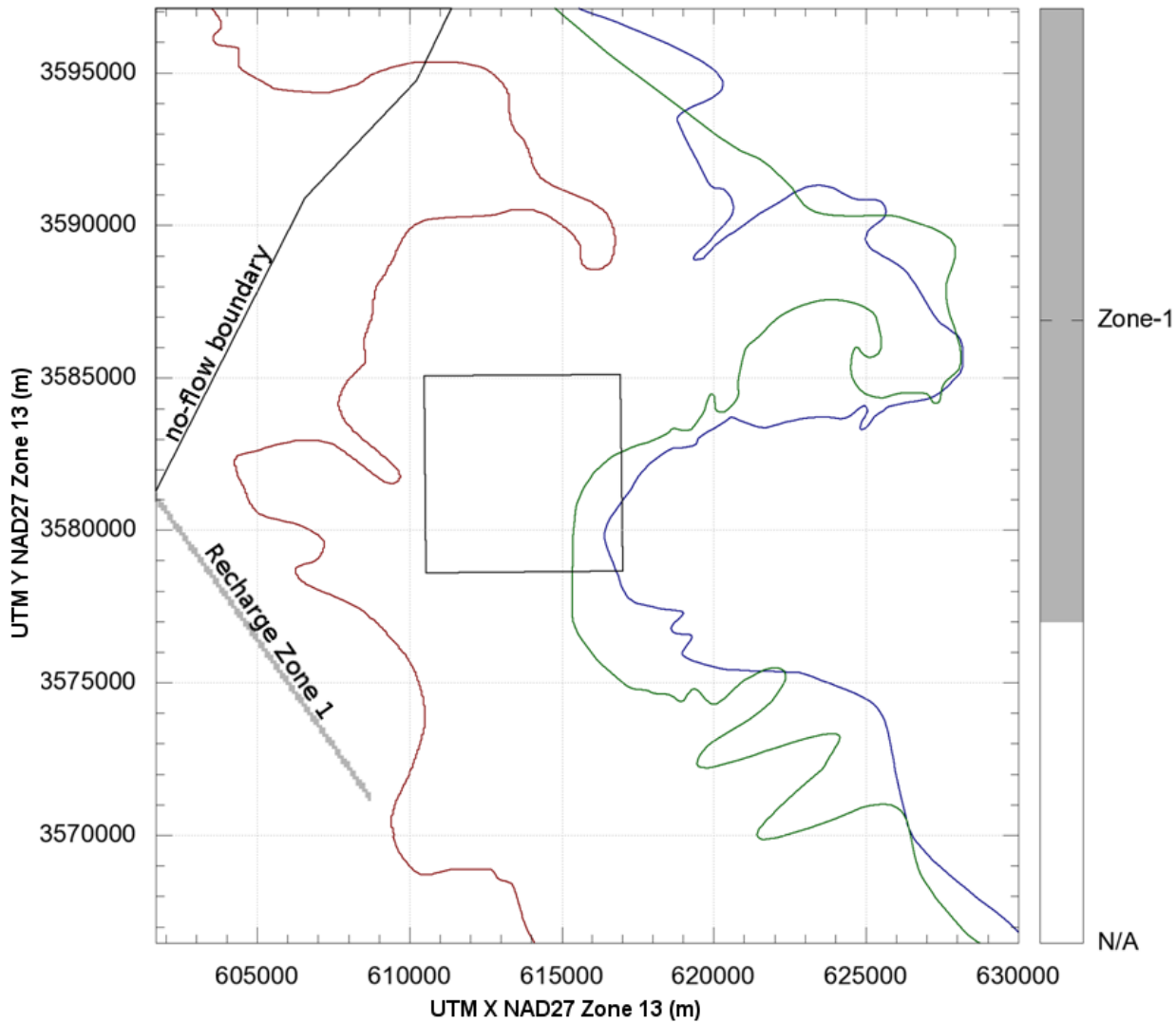


**Figure TFIELD 5-3. Storativity Zones. Zone 0 is confined; Zone 1 is a transition between confined and unconfined; Zone 2 is unconfined; Zone 3 is confined and uncalibrated from the initial confined value; Zone 4 is inactive (no flow).**

#### TFIELD-5.2.1.4 Recharge Zones

The conceptual model presented in Holt (Holt 1997) and Hart et al. (Hart et al. 2008) indicates that a groundwater divide exists somewhere southwest of the WIPP site. Previously in CRA-2004 PABC and CRA-2009, this groundwater divide was represented by extending the no-flow zone all the way to the southern boundary (McKenna and Hart 2003). Because the model used in this current task included the unconfined zone, it was decided to model the groundwater divide using recharge instead of a no-flow boundary. The areas of possible recharge were defined in AP-114 Task 1B (Powers 2006), summarized in Section TFIELD-2.3.1. Recharge values had to be extremely small (on the order of  $10^{-11}$  m/s) to ensure convergence of steady-state MODFLOW simulations. Rather than try to determine which of the configurations presented in Task 1B was the "best" approximation, a similar simple approximation to the older no-flow

1 approach was used. A recharge zone consisting of a line of cells extending NW to SE along the  
 2 axis of the largest topographic feature (and roughly following the old no-flow boundary from  
 3 McKenna and Hart (McKenna and Hart 2003) was used as the recharge zone. See Figure  
 4 TFIELD 5-4 for a map of the recharge zone.

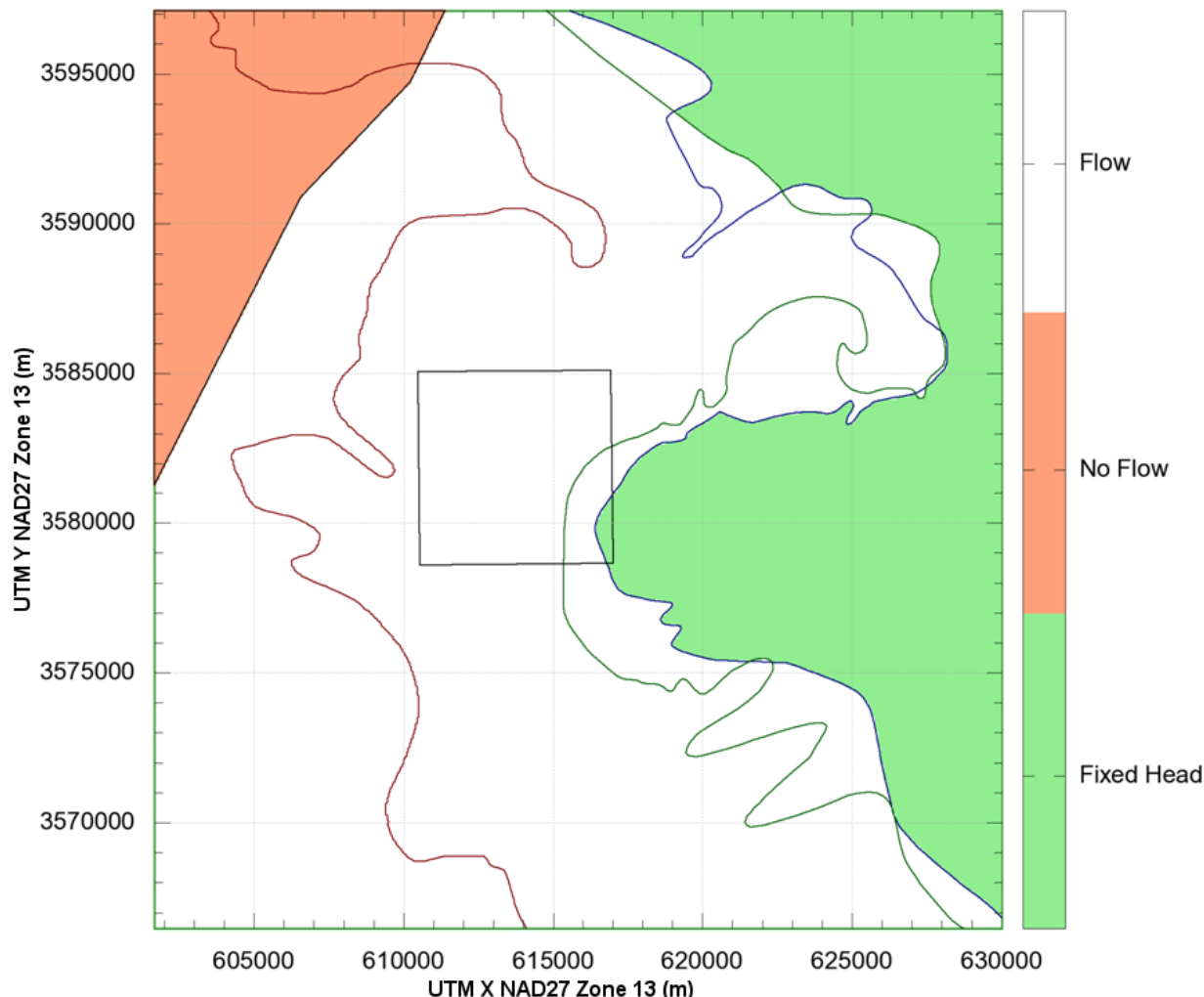


5  
 6 **Figure TFIELD 5-4. Zone 1, the Zone of Non-zero Recharge. Zone 1 is the linear**  
 7 **feature directed southeast from the center of the west edge of the**  
 8 **model domain. The remaining model area has no recharge.**

9 **TFIELD-5.2.1.5 Flow, No-Flow, and Fixed-Head Zones**

10 While the boundary conditions were not variable parameters in the calibration, the definition of  
 11 the specified-head boundary conditions was an important part of the setup and configuration  
 12 step. The no-flow zone in the northwest was defined to be the same as was used in AP-088 for  
 13 CRA-2004 PABC. Though the  $T$  in this area is extremely low ( $10^{-13}$  to  $10^{-11}$   $\text{m}^2/\text{s}$ ), there should  
 14 be some flow exiting along the zone margin, however minute. Testing at SNL-6 and SNL-15

1 indicates that the hydraulic heads in this area may be recovering ultimately to levels above the  
 2 land surface (Roberts 2007; Bowman and Roberts 2008; Appendix HYDRO-2014, Section 7.1).  
 3 The "halite-sandwiched" zone east of either M2/H2 or M3/H3 was simultaneously made  
 4 extremely low  $T$  and set to fixed-head values at the ground surface elevation. While this meant  
 5 that the head values at SNL-6 and SNL-15 were no longer estimable, it was considered the  
 6 simplest way to model the nearly stationary nature of the water in this zone using MODFLOW-  
 7 2000. The flow zones are shown in Figure TFIELD 5-5, and the selection of the initial values is  
 8 discussed in Section TFIELD-5.2.7. The northern, western, and southern flow boundaries were  
 9 all fixed-head boundaries.



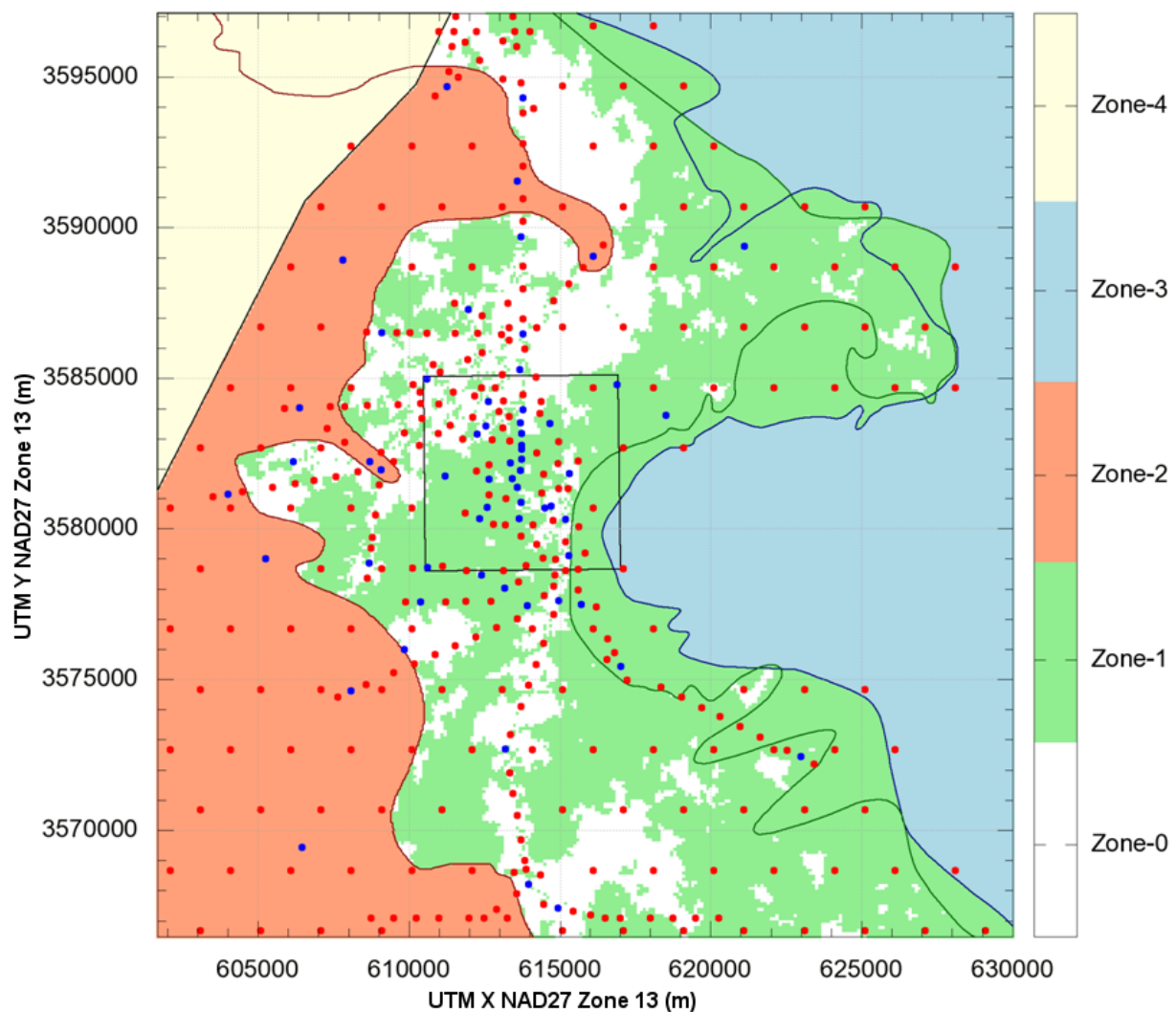
10  
 11 **Figure TFIELD 5-5. Flow Zones. The fixed-head zone is green; the no-flow zone is**  
 12 **salmon; the white area is normal flow. The fixed-head zone**  
 13 **includes one cell along the northern, southern, and western**  
 14 **boundaries.**

1    **TFIELD-5.2.2 Selection of Pilot Point Locations**

2    Once the zones were defined, pilot point locations were selected. There were two types of pilot  
3    points, fixed and variable, and two placement approaches, gridded and linear. Selection of the  
4    points for each parameter required a combination of both types and approaches. The exact  
5    algorithm used to calculate placement is detailed in Hart et al. (Hart et al.2009), and resulted in  
6    the pilot point locations used and shown in Figure TFIELD 5-6 through Figure TFIELD 5-9.

7    **TFIELD-5.2.3 Transmissivity-Specific Pilot Point Settings**

8    In addition to pumping test wells, extra pilot points were placed in the transmissivity fields.  
9    These were included along the northern and southern boundaries to try to limit the effects that  
10   the fixed-head boundaries would have on transient pumping and the steady-state model results.  
11   The estimated  $T$  values from single-well pumping and slug tests were used as fixed  $T$  points that  
12   corresponded to the tested wells (see Table TFIELD 4-2 for test-derived transmissivity values).  
13   See Table TFIELD 5-3 for the ranges of pilot point values used, and see Figure TFIELD 5-6 for  
14   pilot point locations.



1  
2 **Figure TFIELD 5-6.** Transmissivity Pilot Point Locations. Blue points are fixed values  
3 and red points are variable parameters. Zones correspond to a  
4 single realization.

1

**Table TFIELD 5-3. Initial Values of Parameters at Pilot Points**

Parameter	Zone	$\log_{10}$ Value <sup>1</sup>	Pilot Point $\log_{10}$ Calibration Limits
Transmissivity	Zone 0	$-0.003484 d(x,y) - 3.6322$	[−19.0,−1.0]
	Zone 1	$-0.003484 d(x,y) - 5.6981$	[−19.0,−1.0]
	Zone 2	$-0.003484 d(x,y) - 2.9463$	[−19.0,−1.0]
	Zone 3	$-0.003484 d(x,y) - 10.4490$	[−19.0,−1.0]
Anisotropy	All Zones	0.0	[−0.5, 0.5]
Storativity	Zone 0	−5.0	[−5.5,−4.5]
	Zone 1	−4.0	[−6.0,−0.5]
	Zone 2	−1.5	[−2.5,−0.5]
	Zone 3	−5.0	Fixed
Recharge	Zone 1	−11.0	[−19.0,−1.0]

<sup>1</sup>  $d(x,y)$  is Culebra overburden thickness.

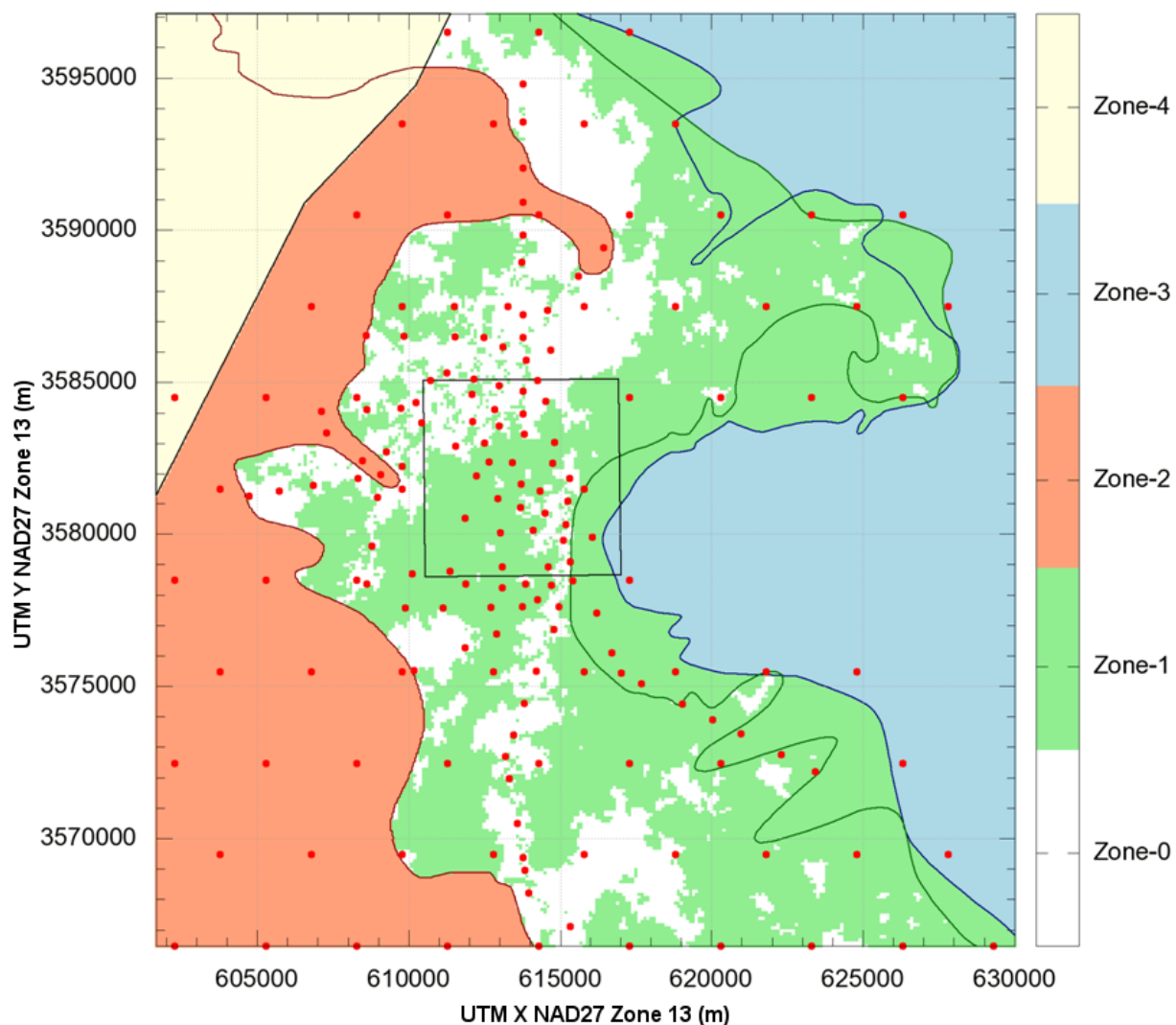
2

### 3 TFIELD-5.2.4 Anisotropy-Specific Pilot Point Settings

4 Anisotropy was unique because no fixed values and therefore no fixed pilot points were used.  
 5 This result is due to the single-well tests not providing any estimate of anisotropy, and the multi-  
 6 well tests providing too localized an estimate of anisotropy (only valid for a single cell or two in  
 7 the model). See Figure TFIELD 5-7 for the locations of anisotropy pilot points.

### 8 TFIELD-5.2.5 Storativity-Specific Pilot Point Settings

9 The only variable storativity pilot points in the confined zone were along straight lines  
 10 connecting pumping and observation wells in transient pumping tests. The gridded points were  
 11 set as fixed values, since it was assumed there was no information allowing for effective  
 12 calculation of storativity outside the transient tests. All pilot points located within the unconfined  
 13 and transition zones were defined as variable. See Figure TFIELD 5-8 for the location of  
 14 storativity pilot points.



1  
2 **Figure TFIELD 5-7.** Anisotropy Pilot Point Locations. All anisotropy pilot points were  
3 variable parameters. Zones correspond to a single realization.  
4

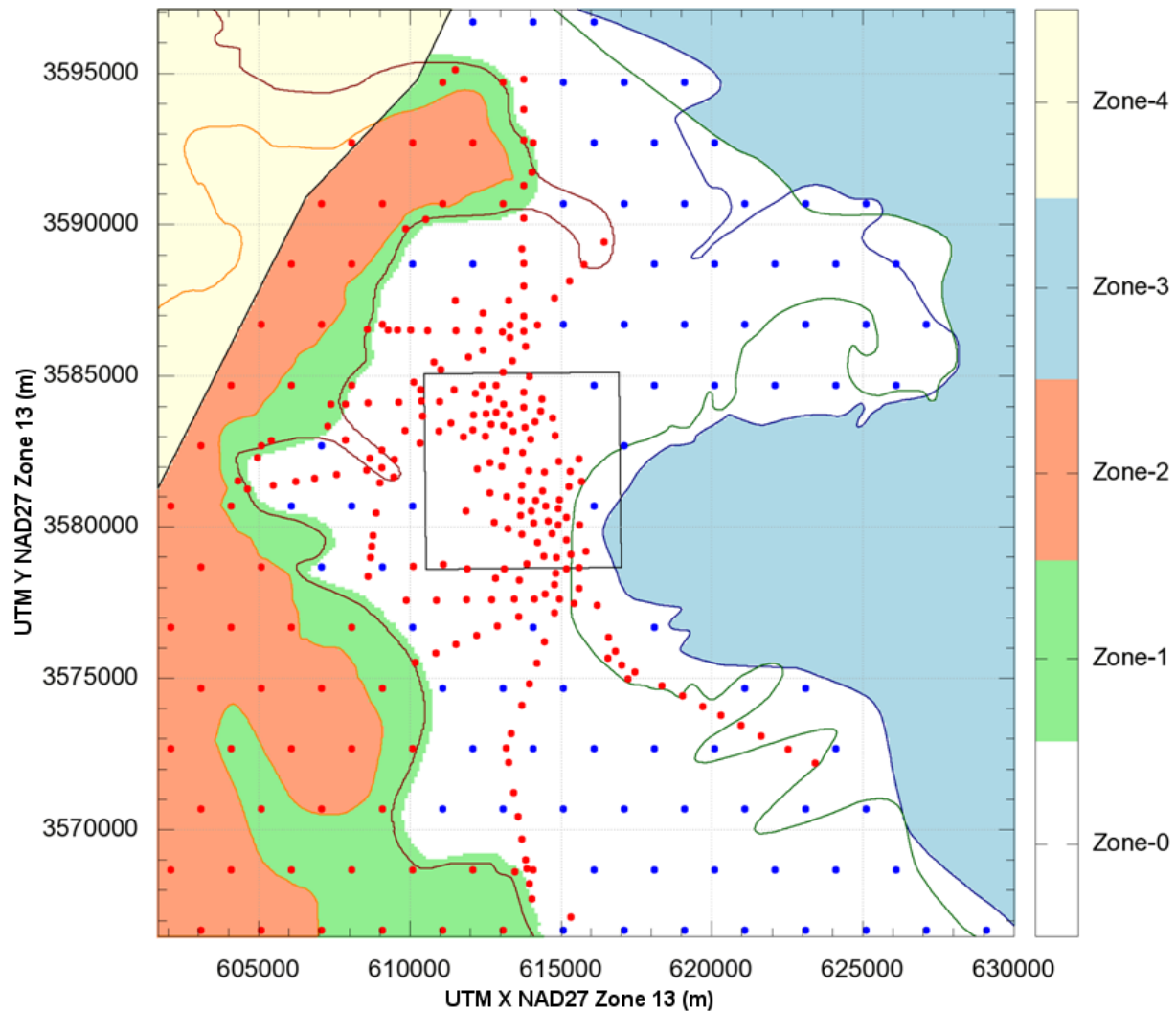


**Figure TFIELD 5-8. Storativity Pilot Point Locations. Only pilot points along lines between wells in transient pumping tests and points in the unconfined zones (zones 1 and 2) were variable (red dots); the remaining pilot points were fixed (blue dots).**

#### TFIELD-5.2.6 Recharge-Specific Pilot Point Settings

Because the recharge zone was a line, only four pilot points were needed in the entire zone. In this case, the pilot point nearest the western domain boundary was set as a fixed value of  $10^{-30}$  m/s, which was interpreted as zero by the pre-processors to MODFLOW, and the other three were variable. See Figure TFIELD 5-9 for the location of the recharge pilot points.

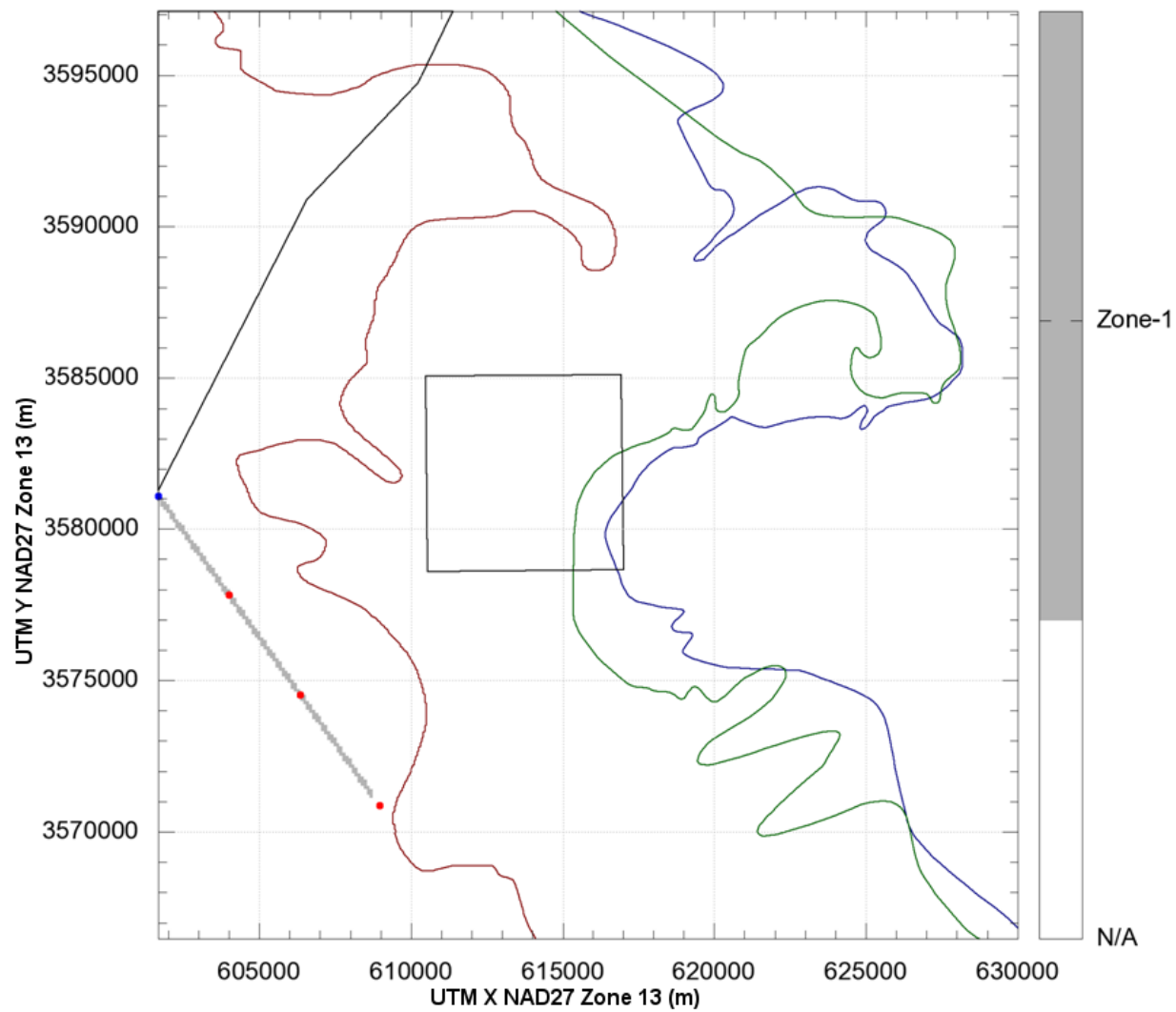


**Figure TFIELD 5-9. Recharge Pilot Point Locations. The pilot point along the model domain boundary was fixed, while the other three points were variable.**

### TFIELD-5.2.7 Selection of Initial Values

Section TFIELD-5.2.7.1 discusses the initial values assigned to parameters before calibration, while TFIELD-5.2.7.2 discusses the assignment of a head field to the initial condition and certain specified-head boundary conditions in the groundwater flow model.

#### TFIELD-5.2.7.1 Parameter Initial Values

The initial values for each of the pilot points were defined according to the conceptual model and the values presented in Hart et al. (Hart et al. 2008), and summarized in Section TFIELD-3.0. For  $T$ , this meant that the same equation used to create the base  $T$  fields was used to define the initial values for the pilot points, based on their zone. Anisotropy was set to isotropic conditions ( $A = 1$ ) for all points. Storativity was defined to start at  $10^{-5}$  for the confined zone (the same

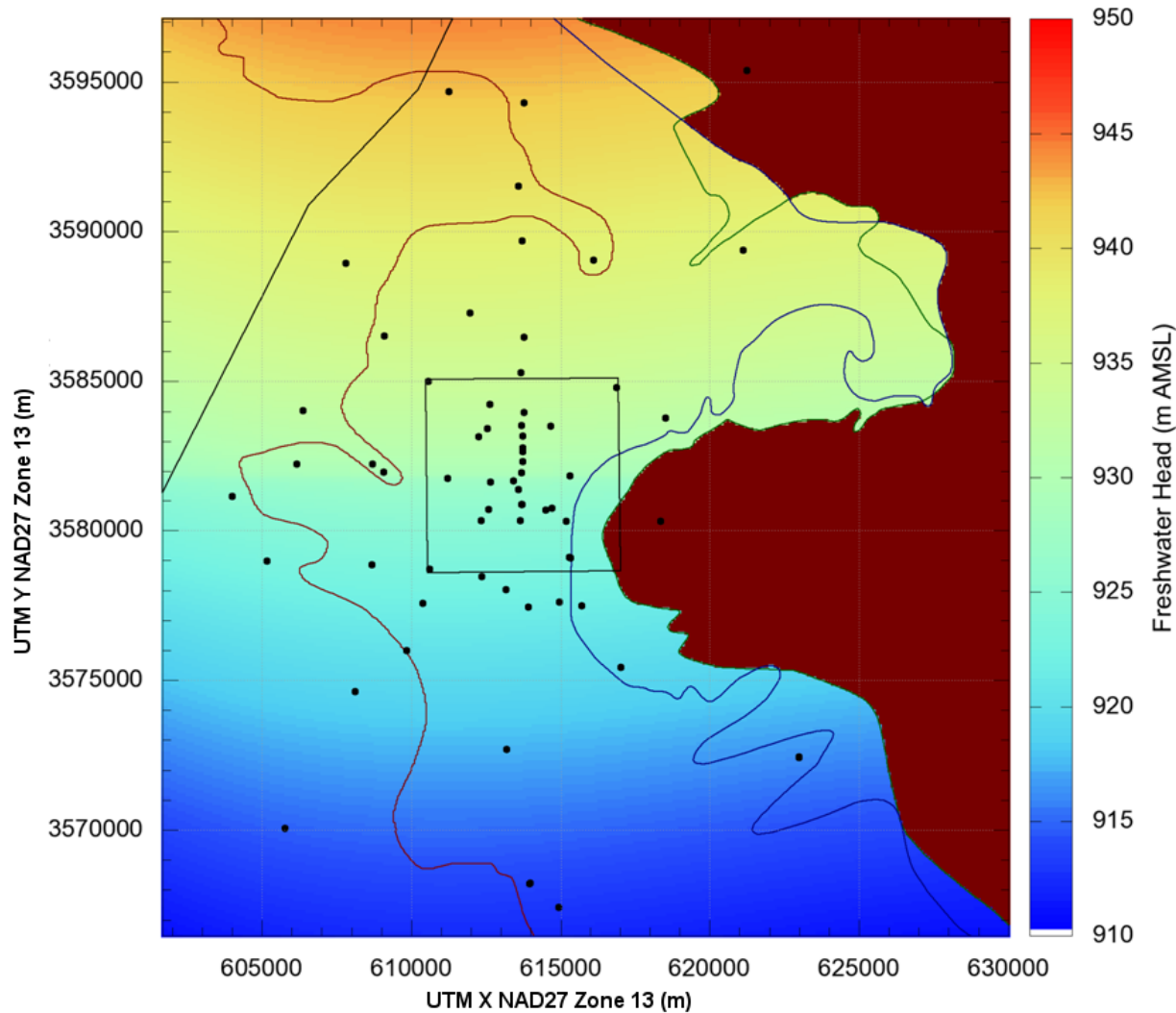
1 value that was used for  $S$  in CRA-2004 PABC model AP-088), at  $10^{-4}$  in the transition zone, and  
 2 at  $10^{-1.5}$  in the unconfined zone. Recharge was initialized as  $10^{-11}$  m/s, a value found to be  
 3 sufficiently small to allow MODFLOW to perform an initial run prior to PEST calibration. The  
 4 zone-by-zone initial values for each parameter, and the limits placed on the range the values  
 5 could take in calibration, are presented in Table TFIELD 5-3. See Table TFIELD 4-2 for fixed  $T$   
 6 values.

## 7 TFIELD-5.2.7.2 Initial Head Field

8 Initial heads ( $H_0$ ) were created using a multivariate equation based on normalized  $x$  and  $y$   
 9 coordinates ( $-1 \leq \{x,y\} \leq +1$ ). The equation was designed to keep head along the northern  
 10 boundary just above the measured head at SNL-1 and head along the southern boundary below  
 11 the level measured at H-9c. These constraints were the defining factors on the constants in the  
 12 equation that follows. This process was done only once, and the result was used as a static input  
 13 file for all calibrations. The field was defined by the following equations

$$14 \quad \begin{aligned} x &= \frac{i}{142} \Big|_{i=-142, -141, \dots, 140, 141} \\ y &= \frac{j}{142} \Big|_{j=-153, -152, \dots, 152, 153} \\ H_0(x, y) &= 928 + 8 \left[ y + \text{sign}(y) \sqrt{|y|} \right] + 1.2(x^3 - x^2 - x) \end{aligned} \quad (\text{TFIELD 5.2})$$

15 where  $\text{sign}()$  is the sign of its argument (either +1 or -1) and  $|y|$  is absolute value. For values east  
 16 of both the H2/M2 and H3/M3 boundaries, the ground-surface elevation was used as the initial  
 17 head value; see Appendix A of Hart et al. (Hart et al. 2009) for details. The resulting initial head  
 18 field is shown in Figure TFIELD 5-10.



1  
2 **Figure TFIELD 5-10.** Initial Head Values for Use in MODFLOW Steady-state Solution.  
3 Brick red head values were fixed at the ground surface elevation  
4 (>1,000 m AMSL).

5 **TFIELD-5.2.8 Creation of Transmissivity Fields**

6 Transmissivity fields are created from pilot points using kriging. Some pilot points are adjusted  
7 using PEST, while other pilot points are held fixed, because they correspond to estimated  $T$   
8 values at wells with pumping tests. A variogram is needed to interpolate and extrapolate from the  
9 pilot points onto every element of the MODFLOW grid.

10 The transmissivity variogram (different from the indicator kriging variogram discussed in  
11 Section TFIELD-4.3) was created using transmissivity values estimated from well tests at 62 of  
12 the wells around the WIPP site. Wells outside the model domain and values at SNL-6 and SNL-  
13 15 were excluded from the calculation. The values at SNL-6 and SNL-15 are both several orders  
14 of magnitude lower than at the other wells, and are in a geologically distinct zone. While initial  
15 calculations showed that there was some statistical anisotropy, there were not sufficient

1 measurements to create an anisotropic variogram. The complete steps for creating the variogram  
 2 are presented in Hart et al. (Hart et al. 2009), Appendix B. The final parameters used are shown  
 3 in Table TFIELD 5-4.

4

5 **Table TFIELD 5-4. Parameters for  $T$  Model Variogram, Fitted to Transmissivity Data**  
 6 **Using an Omnidirectional Variogram with Lag Spacing of 1,500 m**

Parameter	Value
Model Type	Exponential
Nugget	$0.02 (\log_{10} T)^2$
Sill	$1.95 (\log_{10} T)^2$
Range	9,500 meters

7  
 8

### TFIELD-5.2.9 Observations and Residuals

9 The observations (steady-state freshwater heads and pumping test drawdowns) used as  
 10 calibration targets for PEST are summarized in Section TFIELD-5.1. Residuals are calculated as  
 11 the difference between measured and model-generated freshwater heads or drawdowns. The  
 12 PEST utility program MOD2OBS is used to extract the observations from model output at times  
 13 and locations associated with each steady and transient observation.

14 **TFIELD-5.2.10 MODFLOW Numerical Model**

15 Inverse modeling (i.e., automatic calibration) requires a numerical model which generates results  
 16 to compare against observed information. In this task, a MODFLOW 2000 (Harbaugh et al.  
 17 2000) flow model was developed for the Culebra that could use the base fields generated in Hart  
 18 et al. (Hart et al. 2008) as inputs. As was done in CRA-2004 PABC (McKenna and Hart 2003),  
 19 the link algebraic multi-grid (Mehl 2001) solver was used to increase speed and performance  
 20 compared to other available solvers. In addition to  $T$ , it was decided to calibrate the local  
 21 horizontal  $T$  anisotropy, storativity, and a strip zone of recharge as parameters in the calibration.  
 22 Having these four parameters –  $T$ ,  $A$ ,  $S$ , and  $R$  – required a slightly more complex MODFLOW  
 23 model implementation than was used in CRA-2004 PABC AP-088 (McKenna and Hart 2003).  
 24 Specifically, both storativity and anisotropy were single values previously, and changing these to  
 25 cell-by-cell values required the use of the layer property flow package instead of the block  
 26 centered flow package used previously. Using recharge also required the addition of the recharge  
 27 package; both packages are part of the standard MODFLOW distribution (Harbaugh et al. 2000).  
 28 For the known information, steady-state heads from 2007 and drawdown results from nine  
 29 different pumping tests performed between 1985 and 2008 were used as the measured data. A  
 30 conceptual diagram of the MODFLOW model with its inputs and outputs is shown in Figure  
 31 TFIELD 5-11.

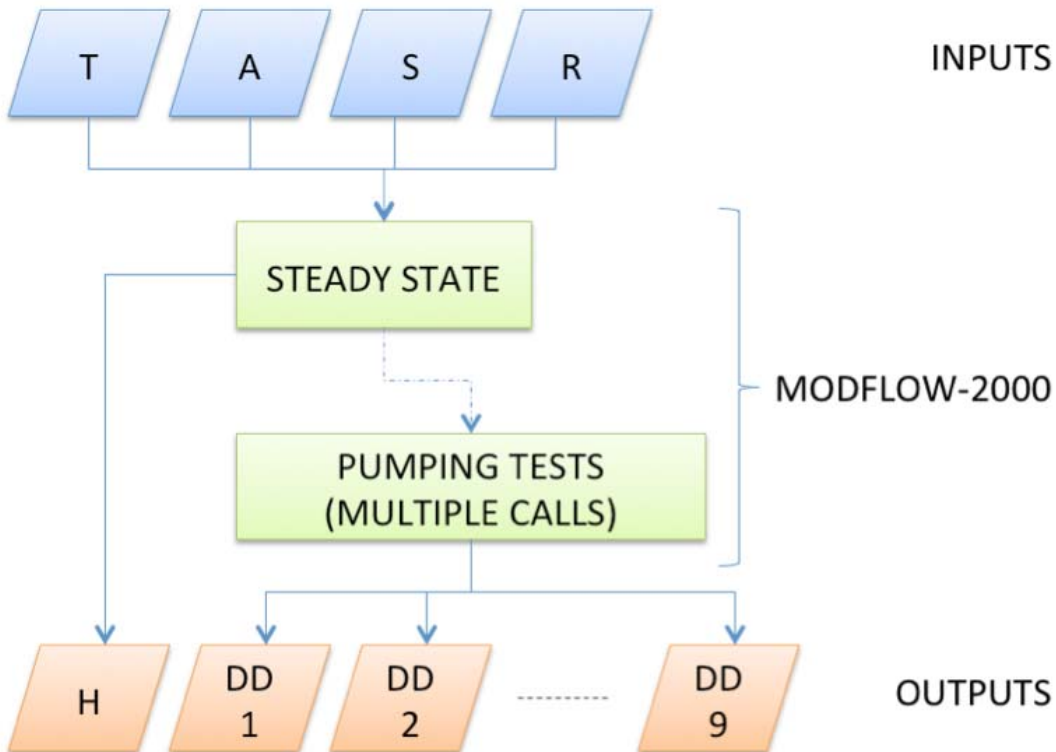


**Figure TFIELD 5-11. Flow Chart Showing the Forward Model Used In the Model Calibration.** *T, A, S, and R are parameter fields. H represents the steady-state flow solution. DD<sub>1</sub>-DD<sub>9</sub> represent transient drawdown computed for the 9 individual pumping tests from 9 separate forward simulations.*

### TFIELD-5.3 Step 2 –Calibration Process

The calibration process used multiple forward model calls to evaluate the impact that perturbing an input parameter has on model predictions at locations and times corresponding to observations. This process was computationally intensive, and involved 80 processors on 2 different computing clusters running for 6 months to calibrate 200 of the 1,000 base T fields.

#### TFIELD-5.3.1 PEST Calibration Process

The calibration process was done using the PEST inverse modeling software suite and its groundwater utilities. The steps involved in each forward model run during the PEST calibration are illustrated in Figure TFIELD 5-12; the complete calibration process is shown in Figure TFIELD 5-1.

The completed PEST simulation included the creation of the fields from the kriging factors and pilot points (PPK2FAC, FAC2REAL, REAL2MOD), the MODFLOW calls, and finally the observation extraction utilities (MOD2OBS and OBS2REAL), which extract modeled cell head or drawdown values from a binary MODFLOW output file. For SVD iterations, another preprocessor, PARCALC, is used to create the pilot point values from the super parameters (i.e., eigenvectors related to the largest eigenvalues – see description in TFIELD-5.0). The model

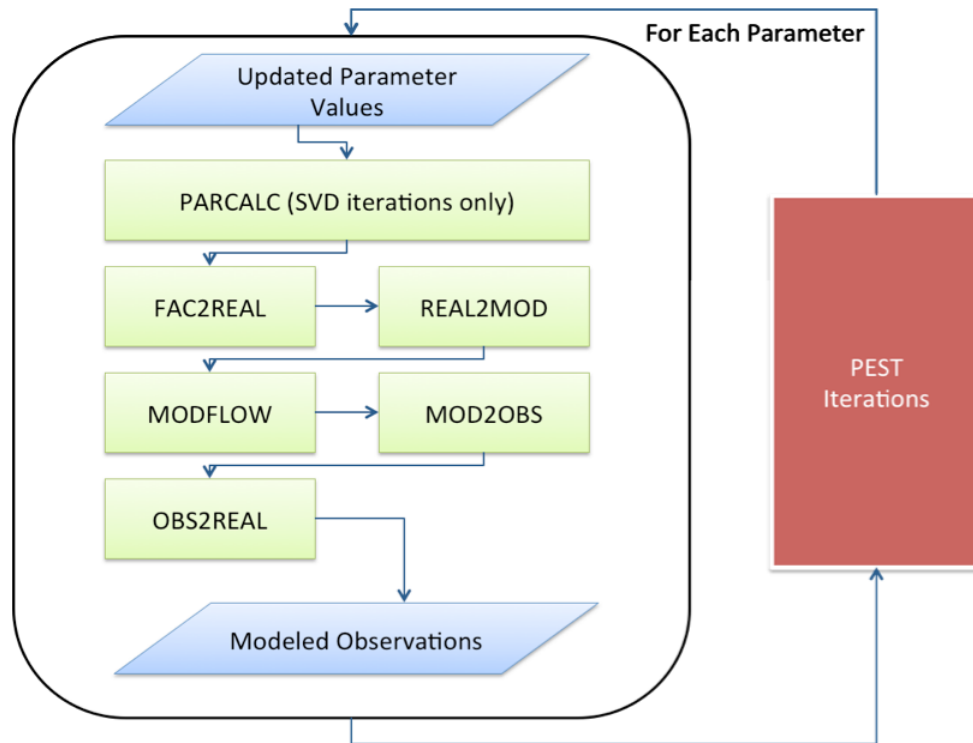
1 script (model.sh), the REAL2MOD script, and the OBS2REAL script were written for this task,  
2 and are included in Appendix G of Hart et al. (Hart et al. 2009). PPK2FAC, FAC2REAL, and  
3 MOD2OBS are PEST utilities.

4 The first call to the PEST program was a single outer iteration to estimate the Jacobian matrix.  
5 This required over 1,100 forward model calls, one for each variable parameter value. Once the  
6 Jacobian matrix was calculated, the SVDAPREP program decomposed the Jacobian matrix into  
7 eigenvectors and kept the super parameters corresponding to the largest singular values. The  
8 result was a set of 100 to 300 super parameters that were then used with a 50-iteration PEST  
9 calibration. The termination criteria were:

10     1. a maximum of 50 iterations,  
11     2. three successive iterations without an improvement in the objective function, or  
12     3. a relative decrease of less than 0.001 in the objective function for three iterations.

13 Once termination criteria had been reached, the PEST program would output the best parameters  
14 to a file. This file was then used to create one final PEST control file, which issued a single  
15 model run with the best parameters as input. The results of this final call were then used to  
16 calculate the measures of fit and the final fields.

17 The run control details regarding the calibration process are presented in Appendix G of Hart et  
18 al. (Hart et al. 2009). Using the ReadScript.py run control system allowed automatic check-out of  
19 input files, execution, and check-in of the results to version control following calibration.



1  
2 **Figure TFIELD 5-12. Flowchart Illustrating the PEST Calibration Process**

3 **TFIELD-5.3.2 Calibrated Correction of Steady-State Head Values**

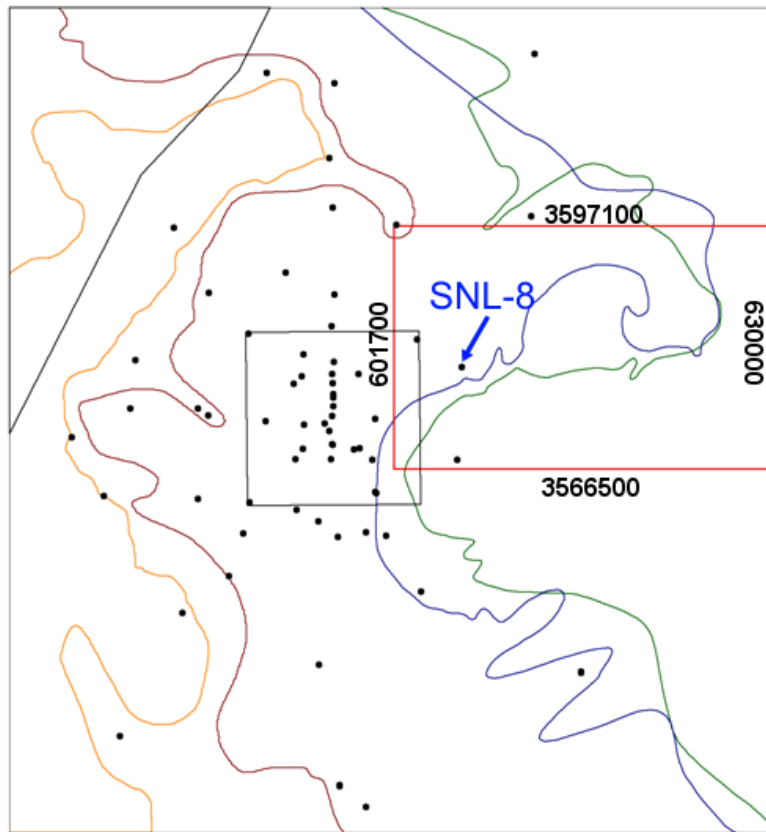
4 Because some of the original steady-state calibration targets were incorrect, the fields that had  
5 already been calibrated to the incorrect data needed to be recalibrated to the new data. The two  
6 wells with the most significant changes, ERDA-9 and SNL-8, had more than one meter change  
7 from the old to new values. At ERDA-9 the calibrations had consistently been unable to match  
8 the incorrect head value, which was too low compared to the higher corrected value. Without any  
9 recalibration, correcting the value for ERDA-9 produced better model fits.

10 **TFIELD-5.3.2.1 Localized Recalibration in the Vicinity of SNL-8**

11 The new calibration target for SNL-8 was based on a recalculation of the freshwater head  
12 (Johnson 2009a and Johnson 2009b). Because SNL-8 was not an observation well in any of the  
13 transient pumping tests, and because it was to the east and upgradient from the WIPP LWB, only  
14 a section of the fields were recalibrated to correct for the change in the calibration target at SNL-  
15 8. It was hoped that this would allow the *T*, *S*, *A* and *R* fields to change to match the SNL-8 head  
16 without requiring the week-long recalibration for each of the affected fields if the entire domain  
17 was recalibrated.

18 The recalibration process involved fixing all the parameters that had previously been calibrated,  
19 except for those parameters in a rectangular area around and upgradient from SNL-8. The  
20 complete area definition was 14 km east-west by 9 km north-south with the southwest corner at  
21 616000 m X, 3580000 m Y UTM NAD27, and is shown in red on Figure TFIELD 5-13. All  
22 other aspects of the automatic calibration, including the forward model and the SVD assist

1 process, were left the same. The resulting fields had significantly better fits to the steady-state  
 2 heads, and little impact was seen on the transient test results (Table TFIELD 5-5).



3  
 4 **Figure TFIELD 5-13. Recalibration Boundary Shown in Red To the Northeast of the**  
 5 **WIPP Site. Recalibration boundary limits are UTM X and Y**  
 6 **NAD27 Zone 13 (m).**

#### 7 **TFIELD-5.3.2.2 Continued Recalibration Activity**

8 After examination of the acceptance criteria (discussed in the next section), some fields were  
 9 recalibrated again, using the same recalibration process but holding none of the parameter values  
 10 fixed at previously calculated values. This process essentially added some additional calibration  
 11 iterations to these fields. This was only done on 15 fields that were now completely within the  
 12 acceptance criteria for steady-state heads, and just outside the acceptance criteria for transient  
 13 tests (Table TFIELD 5-5). The intent of this additional calibration was to increase the quality of  
 14 the transient fits to get a total of 100 fields that met both the steady-state and transient calibration  
 15 requirements. This secondary recalibration process was continued until 100 fields were obtained  
 16 that met the requirements, and it did not always improve fits (i.e., in some cases the fields were  
 17 already as fully calibrated, given the number of pilot points and observations and initial  
 18 conditions).

1                   **Table TFIELD 5-5. Summary of Statistics Regarding Average Steady-state and**  
 2                   **Transient Errors Across Three Calibration Groups**

	Steady-state Average Error (cm)			Pumping Response Average Error (cm)			n
	Minimum	Average	Maximum	Minimum	Average	Maximum	
A	45.6	68.9	195.0	12.9	16.4	34.2	135
B	50.5	73.8	115.3	12.5	16.5	23.0	50
C	57.8	66.1	72.8	13.9	15.4	17.4	15

A: Realizations with targeted recalibration near SNL-8.

B: Realizations with correct SNL-8 data.

C: Realizations recalibrated twice.

#### 4           **TFIELD-5.3.3 Evaluation of Impact of Multiple Calibration Processes**

5           Because some fields were calibrated only once (set B: 50 fields following correction of the  
 6           steady-state values), some fields were calibrated once and then underwent a localized  
 7           recalibration (set A: the 135 first fields calibrated), and some fields even underwent a second  
 8           round of calibration (set C: 15 fields), the impact this may have had on the final selection of  
 9           fields was evaluated. Summaries of statistics for these calibration groups are given in Table  
 10          TFIELD 5-5, while Appendix E of Hart et al. (Hart et al. 2009) contains the complete list of  
 11          fields.

12          Because the final selection process did not look at which set of fields the results were taken from,  
 13          the mix of fields should be similar to a random selection if the calibration processes were  
 14          producing equivalent results. The random selection of fields from set B can be modeled as a  
 15          binomial distribution with the *p*-value of 0.25 and *n* = 100. If the results are within the 95%  
 16          confidence interval for a random selection of fields, then there should be between 17 and 33  
 17          fields selected from the set B. The final results used 83 fields from sets A and C, and the  
 18          remaining 17 were selected from set B. This is within the confidence interval, so it is concluded  
 19          that the different processes had no impact on the selection of the final fields. The selection of  
 20          fields from set C versus those from set A can be modeled the same way, with a *p*-value of 0.10  
 21          and *n* = 83. The final selection included 10 from set C, which is within the confidence interval of  
 22          3 to 13 fields, and again the calibration process did not impact the field selection.

23          Because this mix of final fields is acceptable and came strictly from the cutoff values, and not  
 24          from any deliberate attempt to select from one group or another, all 100 fields meeting the  
 25          acceptance criteria are equally good and equally probable representations of the Culebra.

#### 26          **TFIELD-5.3.4 Selection of Best-Calibrated Fields**

27          The selection criteria for the "best" calibrated fields consisted of comparing the absolute error of  
 28          the modeled steady-state heads (sum of absolute values of residuals between model and data) to  
 29          a cutoff value, and comparing the absolute average error of the modeled transient responses (sum  
 30          of absolute values of errors at individual observation wells averaged through time) to a cutoff  
 31          value. The steady-state and transient criteria were evaluated separately, and only fields that were  
 32          less than the cutoff value for both sets of tests were selected as the final fields. The final cutoff

1 values used were the mean value of the errors taken across all 200 fields, and are presented in  
 2 Table TFIELD 5-6. The cutoffs were selected to choose approximately half of the fields. Using  
 3 the mean values resulted in a set of 102 fields, so the two fields with the largest sum of the two  
 4 metrics were discarded. In Figure TFIELD 5-14, the sum of the steady-state average errors was  
 5 graphed against the sum of the transient pumping tests' average errors, and the selected and  
 6 unselected fields are shown. The trend line shows graphically how PEST allows tradeoffs while  
 7 keeping the improvement in errors as balanced as possible. The final field IDs are presented in  
 8 Table TFIELD 5-7.

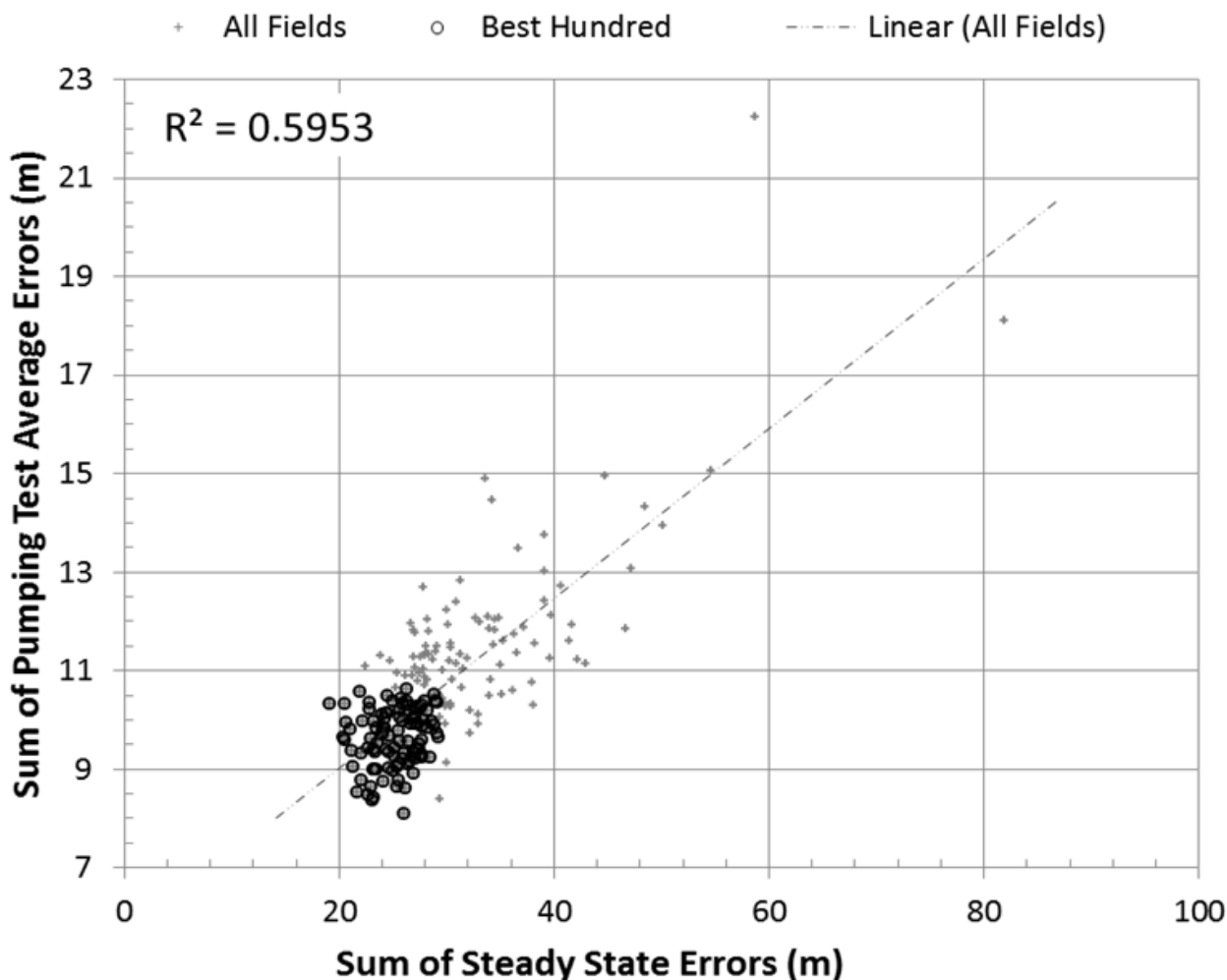
9 **Table TFIELD 5-6. Cutoff Values for Final Field Selection**

Test Type	Average Error Selection Cutoff
Steady State	0.699 m
Transient Pumping Response	0.164 m

10 **Table TFIELD 5-7. Final Selected Field Identifiers**

r001	r055	r207	r652
r002	r058	r256	r655
r004	r059	r260	r657
r006	r060	r273	r664
r007	r061	r276	r669
r009	r064	r279	r694
r010	r070	r298	r707
r012	r073	r327	r727
r013	r074	r328	r752
r017	r076	r361	r791
r024	r078	r431	r806
r027	r082	r440	r808
r028	r083	r465	r809
r029	r084	r486	r814
r032	r090	r489	r823
r034	r092	r506	r861
r037	r095	r508	r883
r038	r097	r511	r902
r040	r098	r515	r910
r041	r102	r522	r921
r045	r104	r568	r922
r051	r137	r571	r940
r052	r142	r631	r981
r053	r191	r634	r982
r054	r203	r640	r984

12



1  
2 **Figure TFIELD 5-14. Selection of Best Fields From All Fields by Weighted Sum of**  
3 **Steady-state Errors and Sum of Average Pumping Test Average**  
4 **Errors**

## 5 **TFIELD-5.4 Step 3 – Post-Calibration Analysis**

6 The post-calibration analysis consisted of performing statistical analyses on the selected fields,  
7 and examining the calibrated forward model outputs. The full results of the steady-state forward  
8 model outputs are presented in Appendix C of AP-114 Task 7 (Hart et al. 2009), pumping test  
9 results are presented in Appendix D, and tabular results are presented in Appendix E of the same  
10 report. Calibrated model inputs and outputs for the 100 selected fields are presented in  
11 Attachment A to Appendix TFIELD.

### 12 **TFIELD-5.4.1 Statistical Analysis of Resulting *T*, *A*, and *S* Fields**

13 Plots of mean and standard deviation of the final 100 fields are given in Section TFIELD-5.4.1.1.  
14 The bulk *T* of the final calibrated fields are also compared to the bulk *T* of the base fields, using  
15 membership in the high or low *T* categories. Similarly, Sections TFIELD-5.4.1.2 and TFIELD-  
16 5.4.1.3 show summary statistics regarding the calibrated *S* and *R* fields, respectively.

## 1 TFIELD-5.4.1.1 Final Transmissivity and Anisotropy Fields

2 The  $T$  values presented in this section are the effective  $T$  values ( $T_e$ ), which include  $A$ . Effective  
3 transmissivity was calculated as

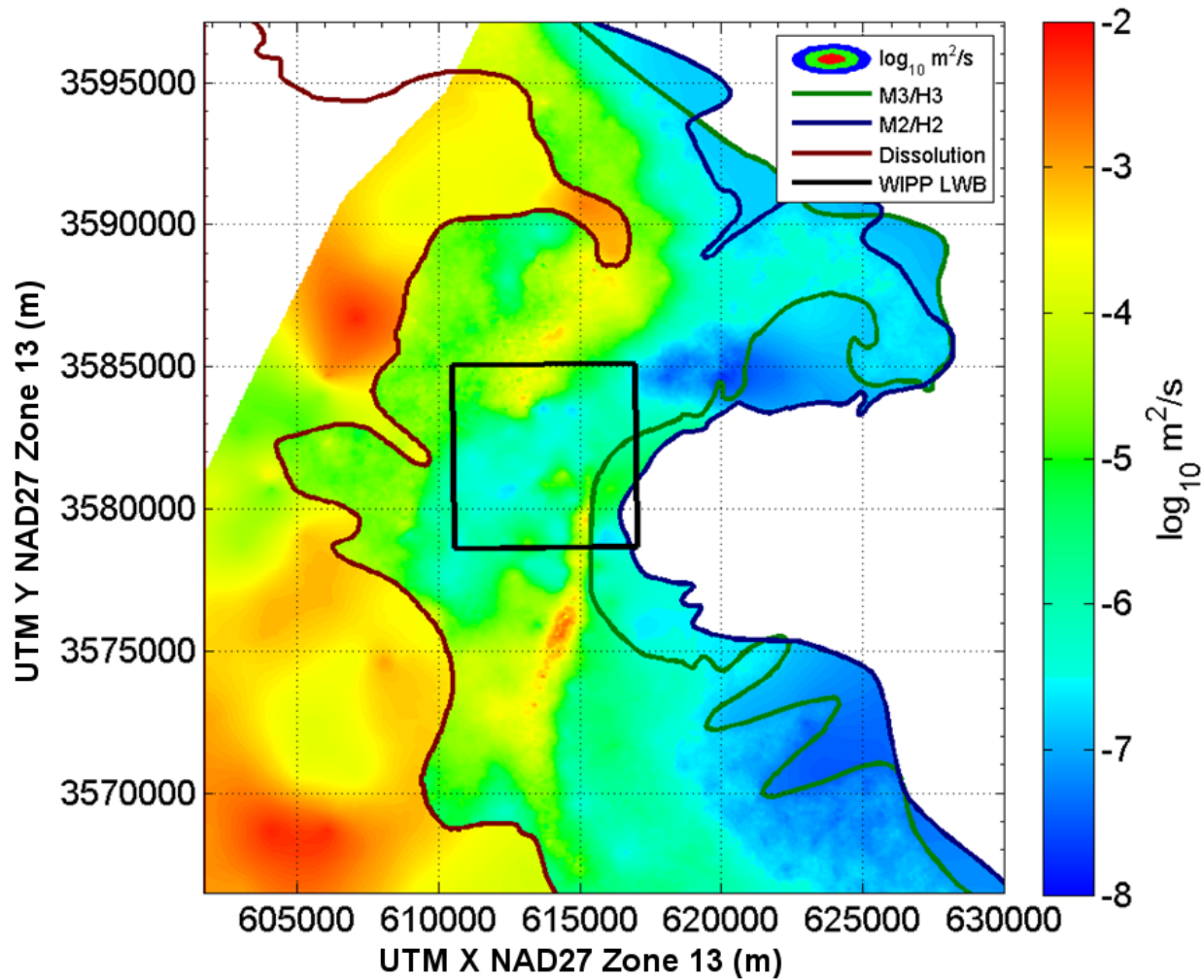
$$\log_{10} T_e = \log_{10} T_{EW} + \frac{1}{2} \log_{10} A \quad (\text{TFIELD 5.3})$$

5 which is the average of  $\log_{10} T$  in the north-south and east-west directions (see Equation TFIELD  
 6 5.1 in Section TFIELD-5.2.1.2). The bulk  $T_e$ , which is the average  $\log_{10} T_e$  value of all cells in a  
 7 given zone or zones, was calculated for the central and Salado dissolution region (zones 0-2) and  
 8 compared to the bulk  $T_e$  of the same zones from the base fields. The eastern, very low- $T$  region  
 9 (zone 3) was compared separately. The bulk  $T_e$  values are shown in Table TFIELD 5-8. The  
 10 mean effective  $T_e$  and the standard deviation of  $T_e$  are presented in map form in Figure TFIELD  
 11 5-15 and Figure TFIELD 5-16. The mean effective transmissivity map does not show the very  
 12 low  $T$  zone east of the halite margins to improve the colormap contrast across the area around the  
 13 WIPP site.

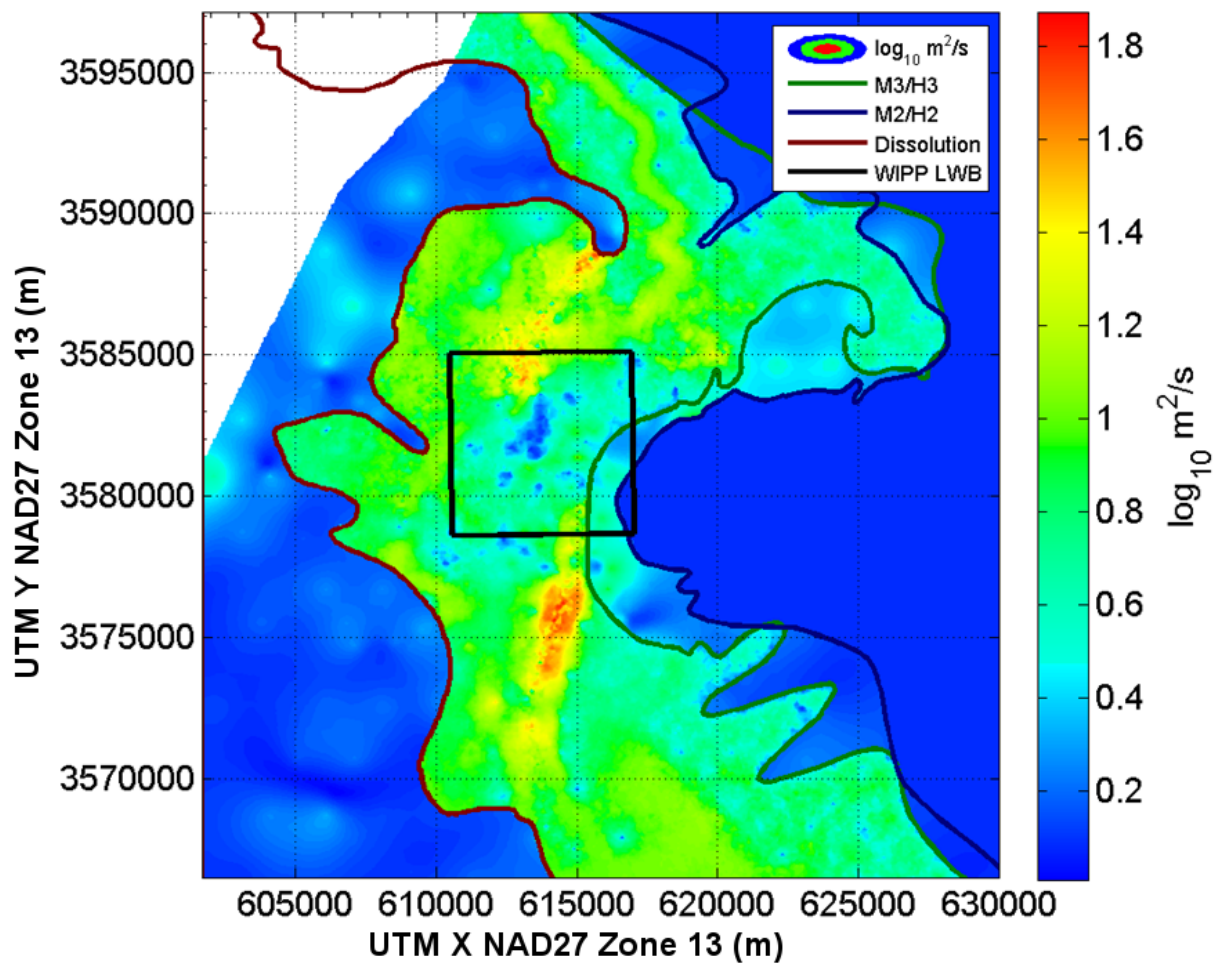
Because pilot point parameter values were essentially unconstrained for  $T$  (they were allowed to change across 18 orders of magnitude as shown in Table TFIELD 5-3), some areas in zones 0 and 1 could change from a low- $T$  zone into the range generally considered high- $T$  and vice versa. The defining value for high- $T$  was set in AP-114 Task 5 (Hart et al. 2008) to be the bulk transmissivity value of the base fields:  $-5.41 \log_{10} m^2/s$ . At each cell, the number of fields whose initial and final  $T$  values were in the high- $T$  zone was calculated, and the maps of those numbers for the base and calibrated fields are presented in Figure TFIELD 5-17 and Figure TFIELD 5-18, respectively. The total number of fields where transmissivity effectively changed zones is represented graphically in Figure TFIELD 5-19 and Figure TFIELD 5-20. In these figures, the white regions define areas where no fields changed groups. The two measures shown in these sets of maps provide an indication of how the geologically based conceptual model used to create the base fields was altered by the steady-state and transient hydraulic information.

**Table TFIELD 5-8. Bulk Log<sub>10</sub>  $T_e$  Values Comparison**

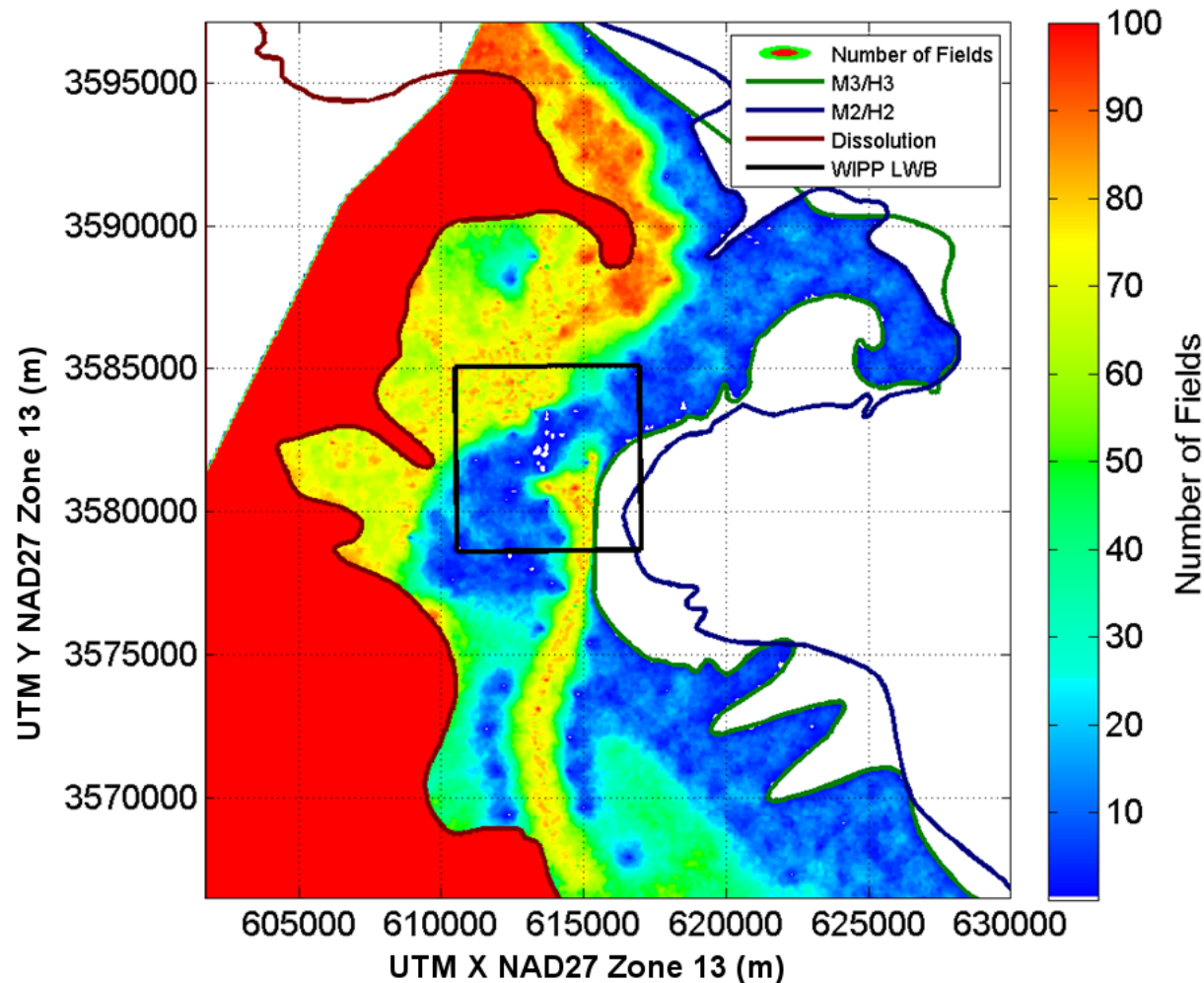
Base field bulk $\log_{10} T_e$ (Zones 0-2)	$-5.41 \log_{10} (m^2/s)$
Calibrated field bulk $\log_{10} T_e$ (Zones 0-2)	$-5.02 \log_{10} (m^2/s)$
Base field bulk $\log_{10} T_e$ (Zone 3)	$-11.74 \log_{10} (m^2/s)$
Calibrated field bulk $\log_{10} T_e$ (Zone 3)	$-10.47 \log_{10} (m^2/s)$



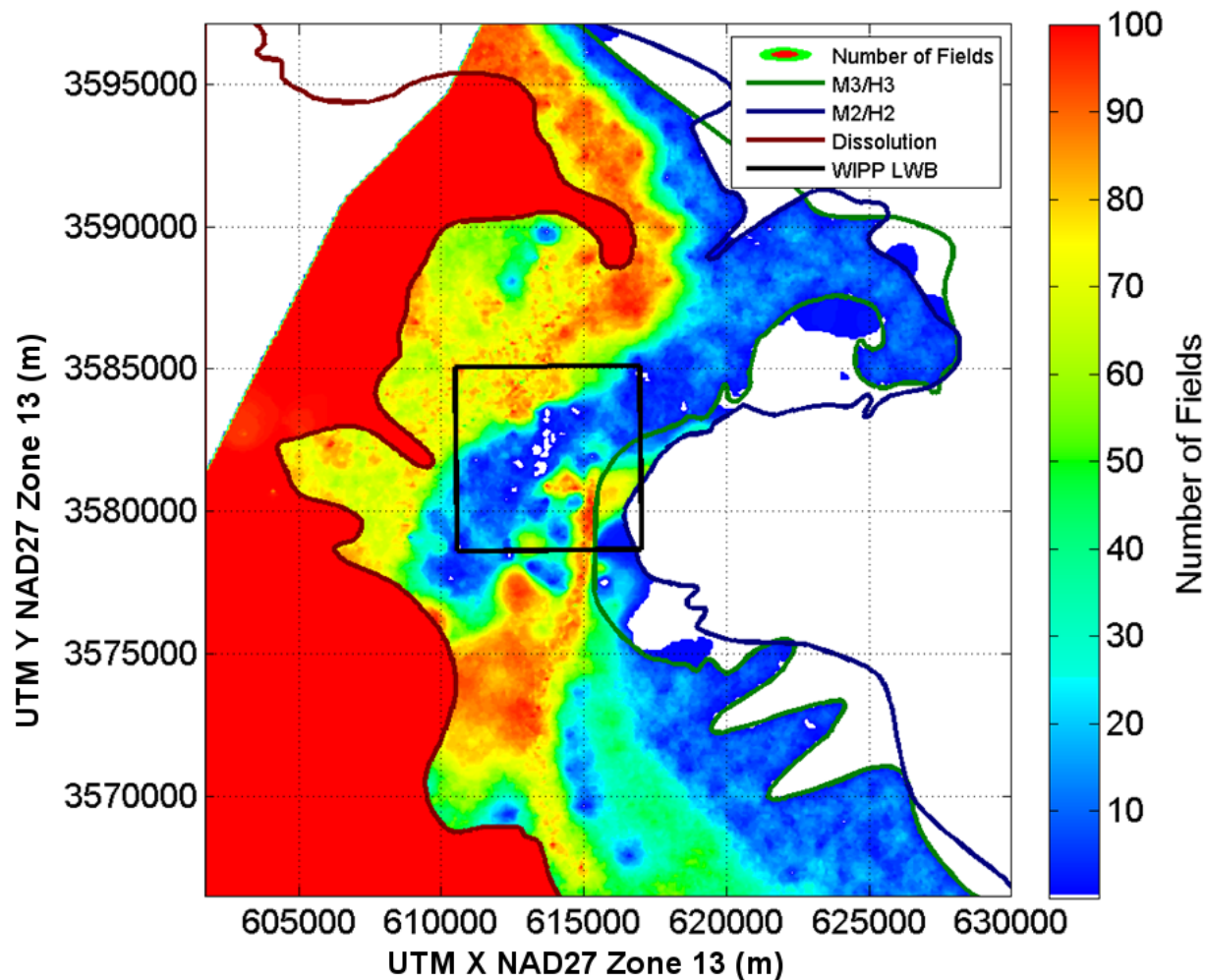
1  
2 **Figure TFIELD 5-15. Mean Effective Transmissivity ( $T_e$ ) for Zones 0-2 Across the 100**  
3 **Final Selected Fields. All 100 calibrated  $T_e$  fields are plotted in**  
4 **Appendix TFIELD Attachment A.**



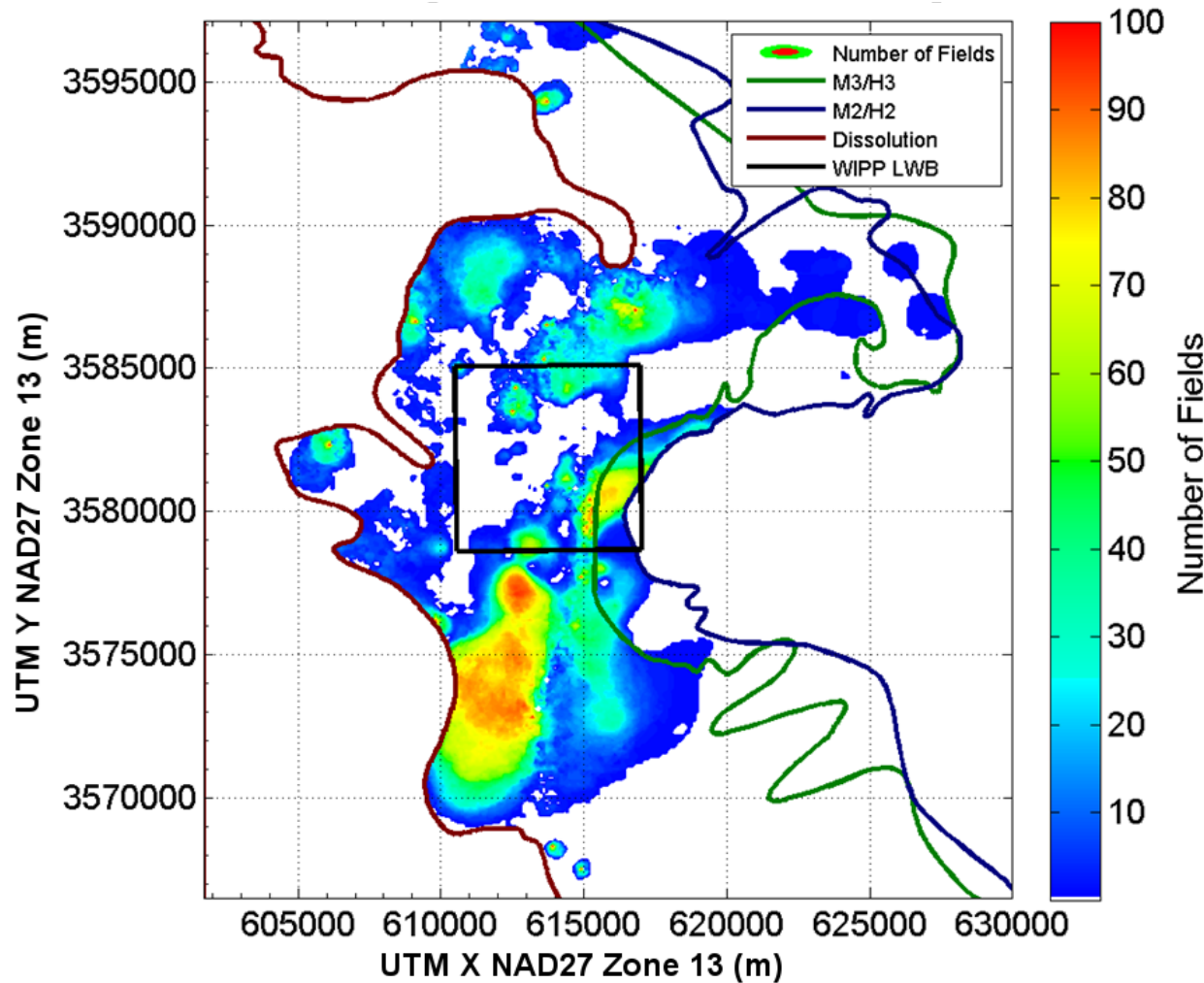
1  
2 **Figure TFIELD 5-16.** Standard Deviation of Effective Transmissivity ( $T_e$ ) for All  
3 Zones Across the 100 Final Selected Fields. All 100 calibrated  
4  $T_e$  fields are plotted in Appendix TFIELD Attachment A.

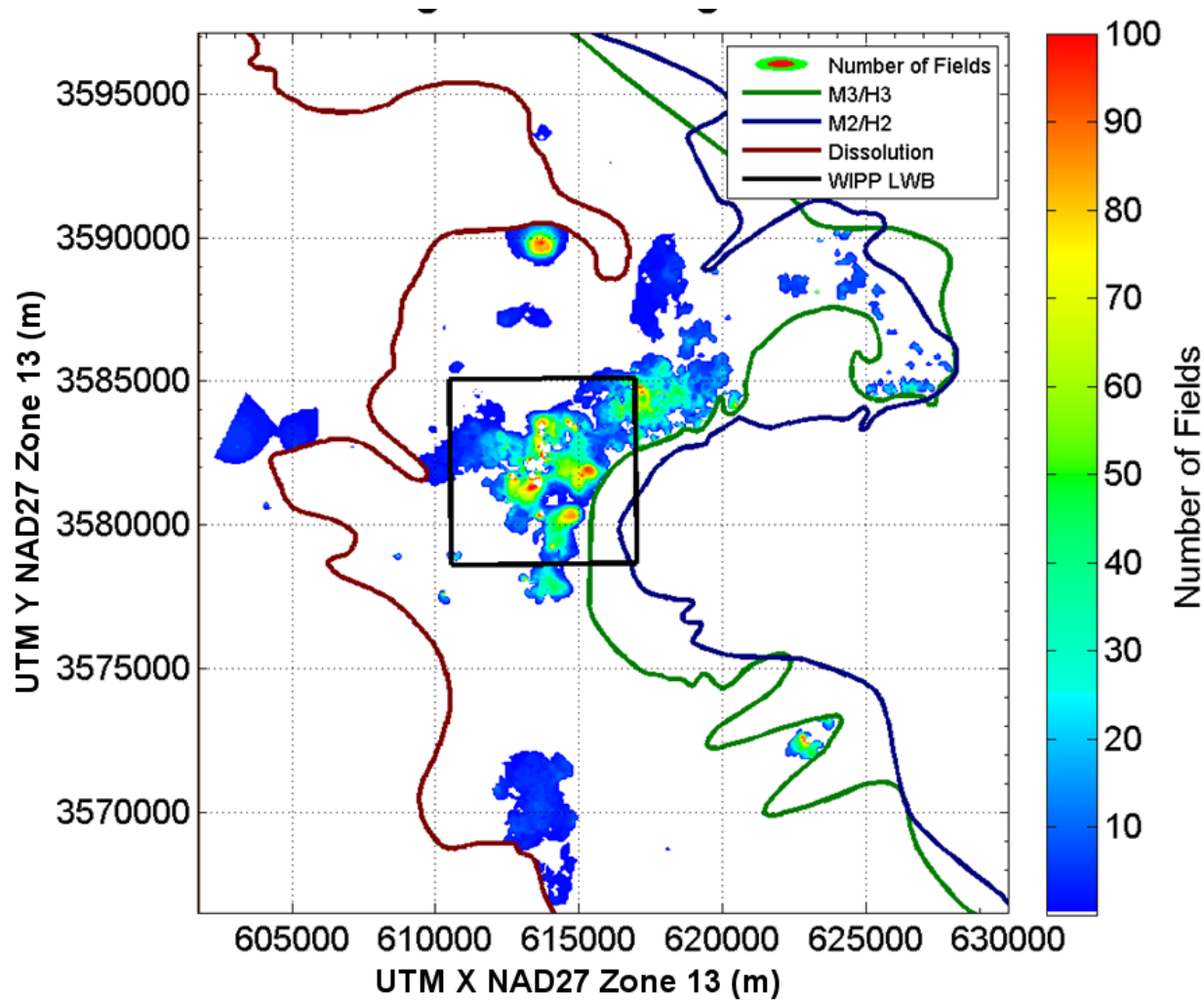


1  
2 **Figure TFIELD 5-17. High-*T* Zone Membership Calculated for the Base 100 *T* Fields**  
3 Corresponding to the 100 Selected Calibrated Fields



1  
2 **Figure TFIELD 5-18. High- $T$  Zone Membership Calculated for the Calibrated  $T$  Values**

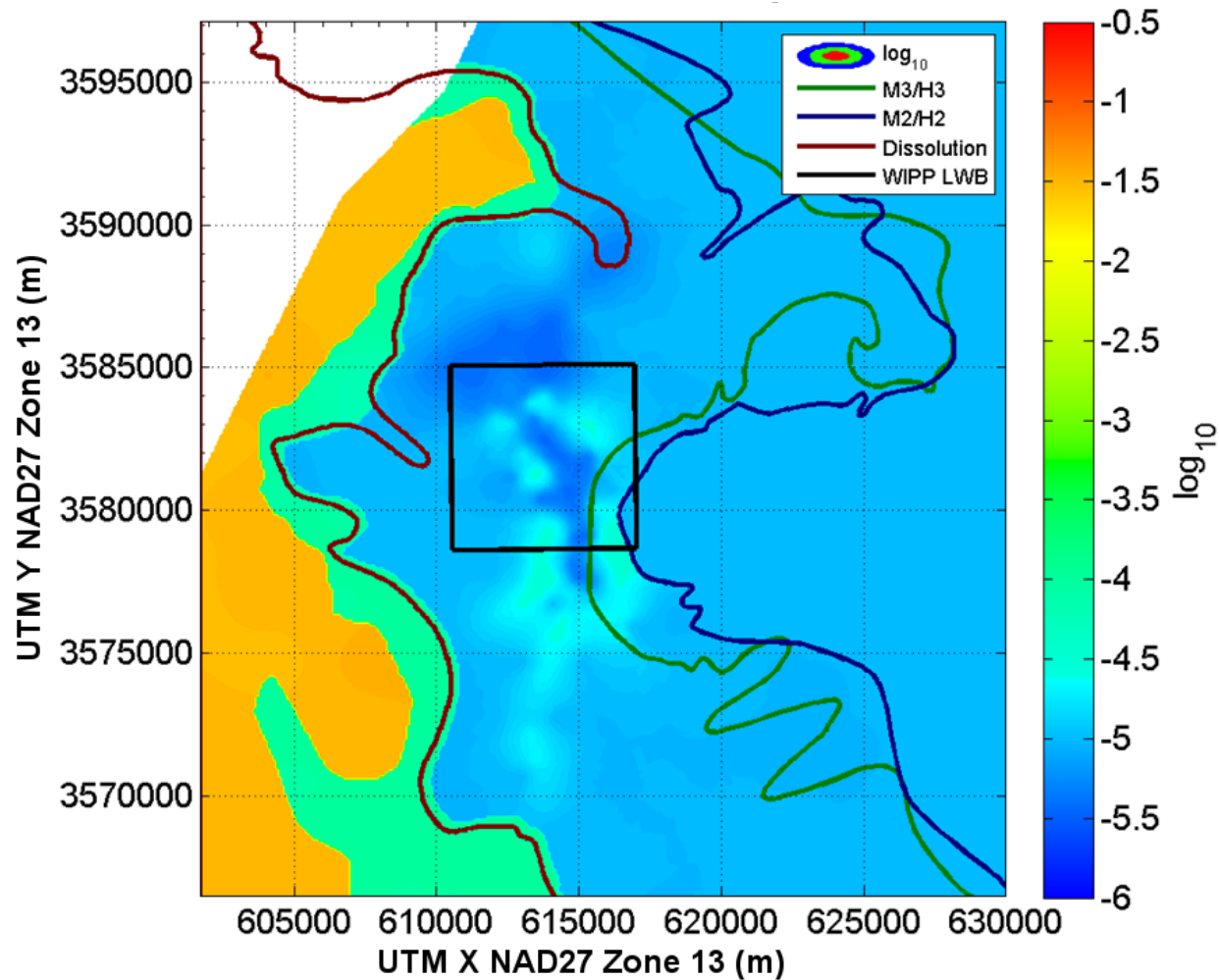




1  
2     **Figure TFIELD 5-20. Number of  $T$  Fields Where High  $T$  Became Low  $T$  Through  
3       PEST Calibration**

4     **TFIELD-5.4.1.2 Final Storativity Values**

5     The mean and standard deviation of the final  $S$  fields are presented in Figure TFIELD 5-21 and  
6     Figure TFIELD 5-22. The mean  $S$  fields indicate that the overall  $S$  values in the confined and  
7     transitional zones did not change much from their initial values. Figure TFIELD 5-22 highlights  
8     the area northwest of P-14 with a red dashed oval. This area has high variability in estimated  $S$   
9     across the 100 selected realizations. This may have some relation to the relatively poorer fits of  
10    the transient data for the WIPP-25 response to the P-14 pumping test in the model.



1  
2 **Figure TFIELD 5-21. Mean Storativity Values Across the 100 Final Calibrated Fields.**  
3 **Individual S fields are plotted in Appendix TFIELD Attachment**  
4 **A.**

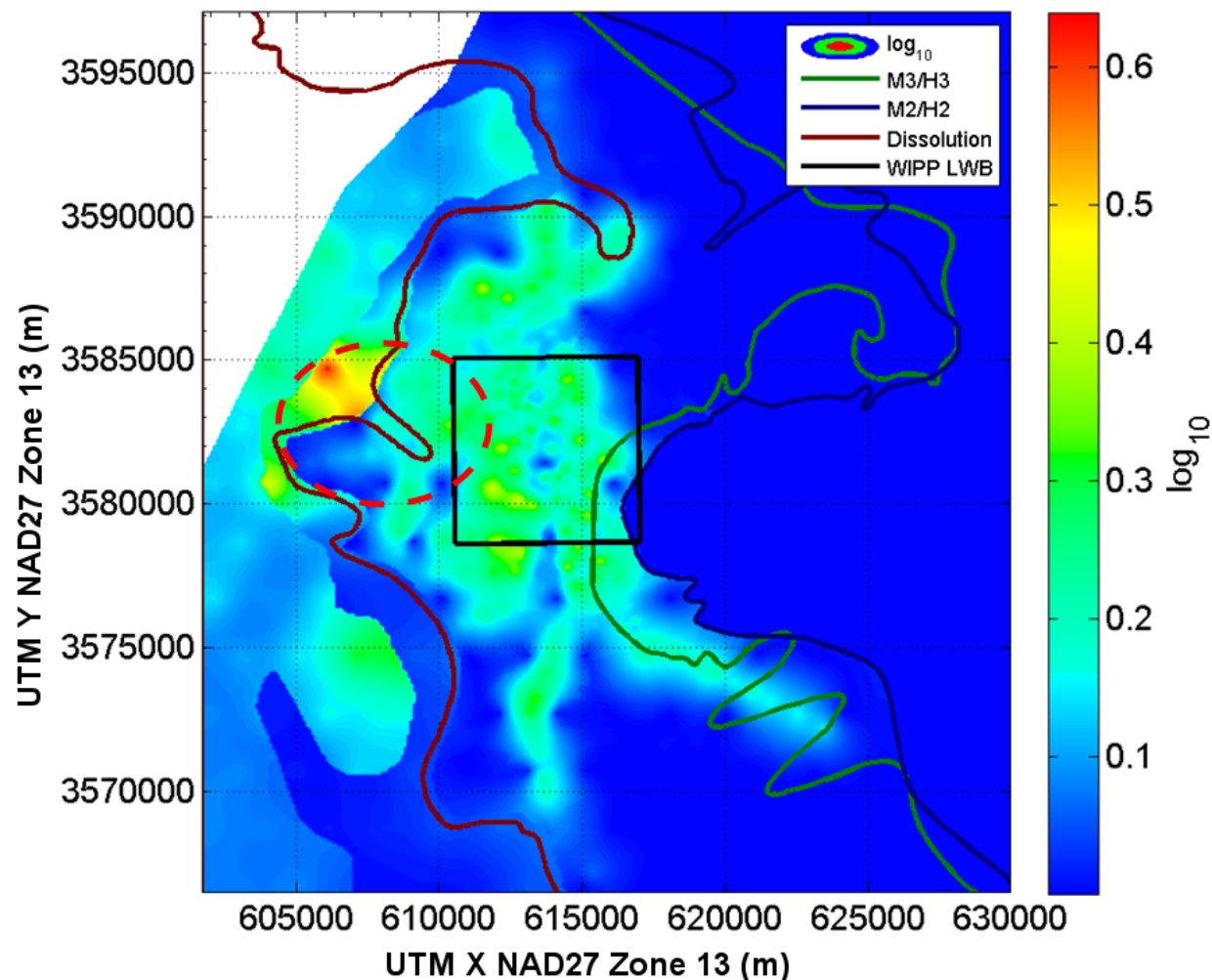
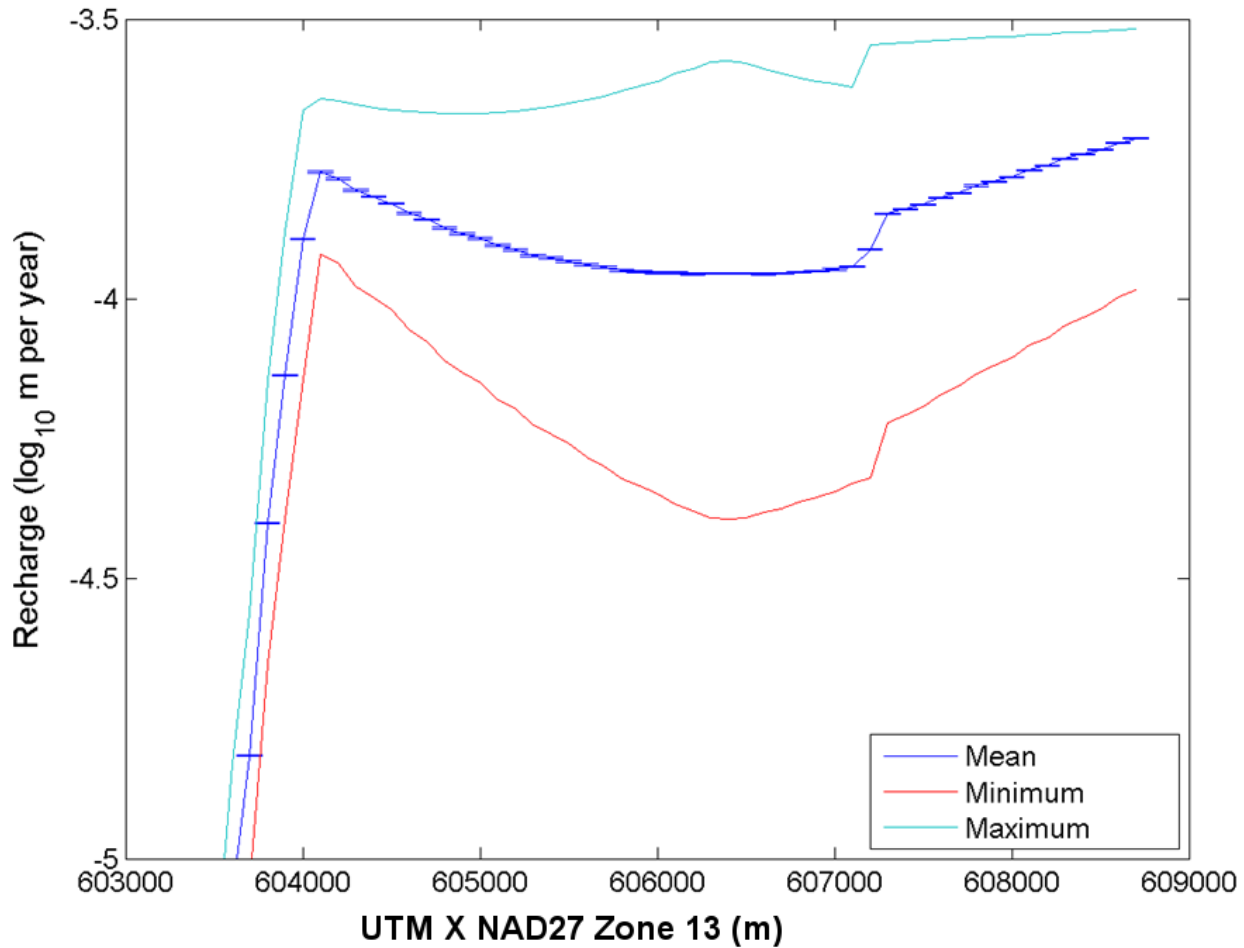


Figure TFIELD 5-22. Standard Deviation of Storativity Values Across the 100 Final Calibrated Fields. Red oval shows P-14 to WIPP-25 area of influence. Individual  $S$  fields are plotted in Appendix TFIELD Attachment A.

#### TFIELD-5.4.1.3 Final Recharge Values

The final recharge values were all less than the initial values of  $10^{-11}$  m/s ( $3.2 \times 10^{-4}$  meters per year (m/yr)). Compared to the other parameters, there was very little change in recharge. Because the recharge zone was linear, in addition to the cell-by-cell mapping, a view of the average, minimum and maximum recharge values is shown as a cross section in the cross-direction (across a row) as if looking from the south to the north through the domain in Figure TFIELD 5-23.



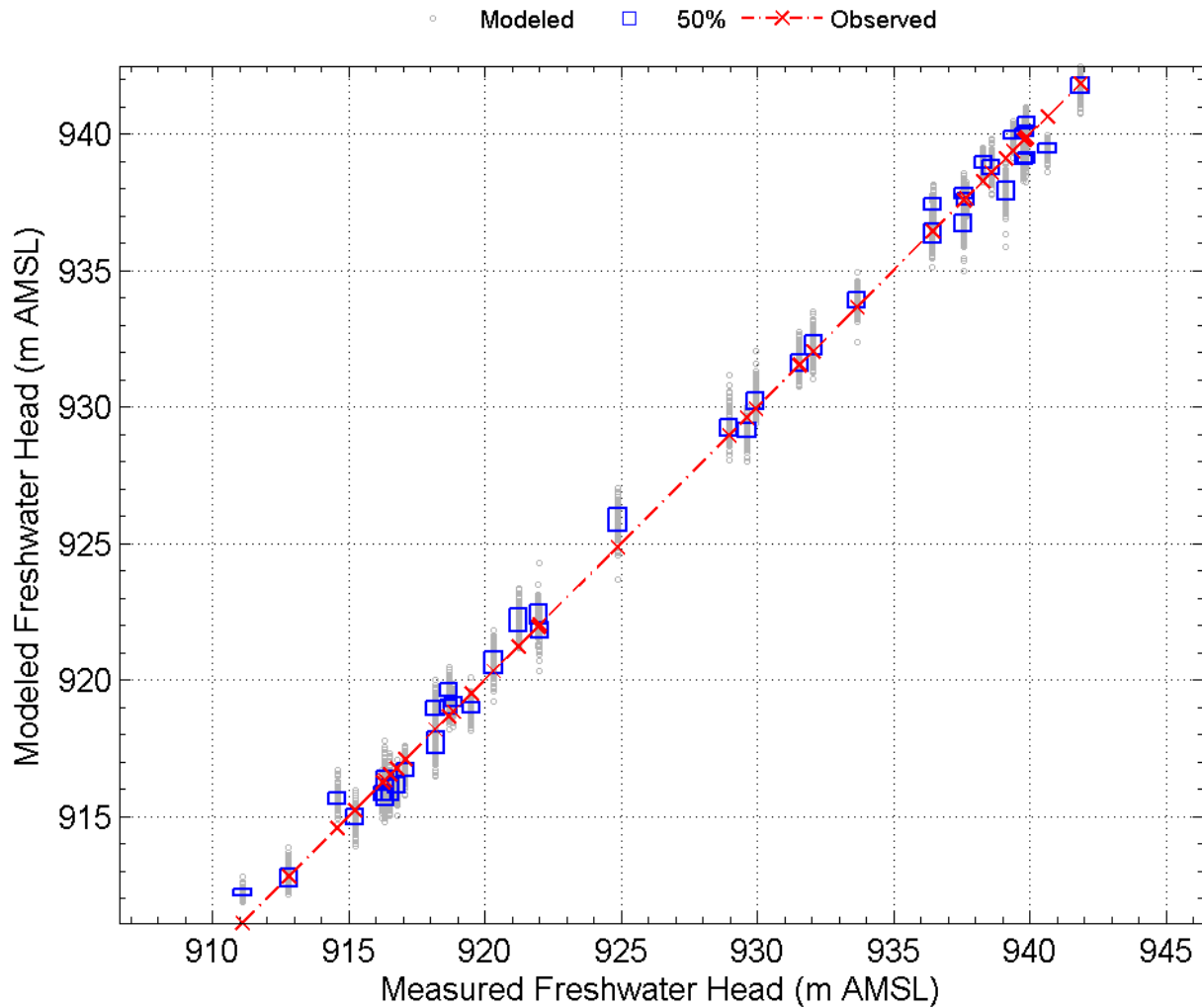
**Figure TFIELD 5-23.** Recharge as Viewed Through Columns From the South. The initial value was set at  $10^{-3.5}$  m/year. The sharp dropoff to the west is the transition to the single fixed-recharge point of  $10^{-11.5}$  m/year (interpreted as zero by REAL2MOD).

#### TFIELD-5.4.2 Forward Model Results Using the Calibrated Fields

The two main divisions of the results are the steady-state head results and the pumping test results. The results presented here only represent the 100 final selected fields, and therefore the maximum error is limited by the selection criteria described in Section TFIELD-5.3.4: an average steady-state error of less than 0.699 m and an average pumping test observation error of less than 0.164 m.

Figure TFIELD 5-24 shows the modeled steady-state head values plotted against the measured head values. The one-to-one correspondence line shows the ideal match, and the modeled results are presented as box-and-whisker plots at each observation well. Figure TFIELD 5-25 shows all 4,200 head errors across all 100 fields as a histogram of error values for steady-state head. Additional figures and tables summarizing steady-state calibration are presented in Appendix C of Hart et al. (Hart et al. 2009). The model-measurement misfit can be modeled as a zero-mean Gaussian distribution with a standard deviation of 0.10 m (McKenna and Wahi 2006). The measurement error distribution curve is included in Figure TFIELD 5-25.

1 Graphs for each of the transient pumping test results are presented in Appendix D of Hart et al.  
 2 (2009). The average value of the error in the final fields ranged from 0.12 m to 0.164 m across  
 3 all tests, with an average error of 0.15 m. The maximum error for a single observation well  
 4 ranged from 0.005 m to 2.5 m, with an average of 0.36 m as the maximum error at a given  
 5 observation well.



6  
 7 **Figure TFIELD 5-24.** Results for 42 Total Steady-state Head Measurements for the  
 8 100 Selected Fields (No SNL-6 or SNL-15). Observed heads are  
 9 red 'x's along the diagonal line.

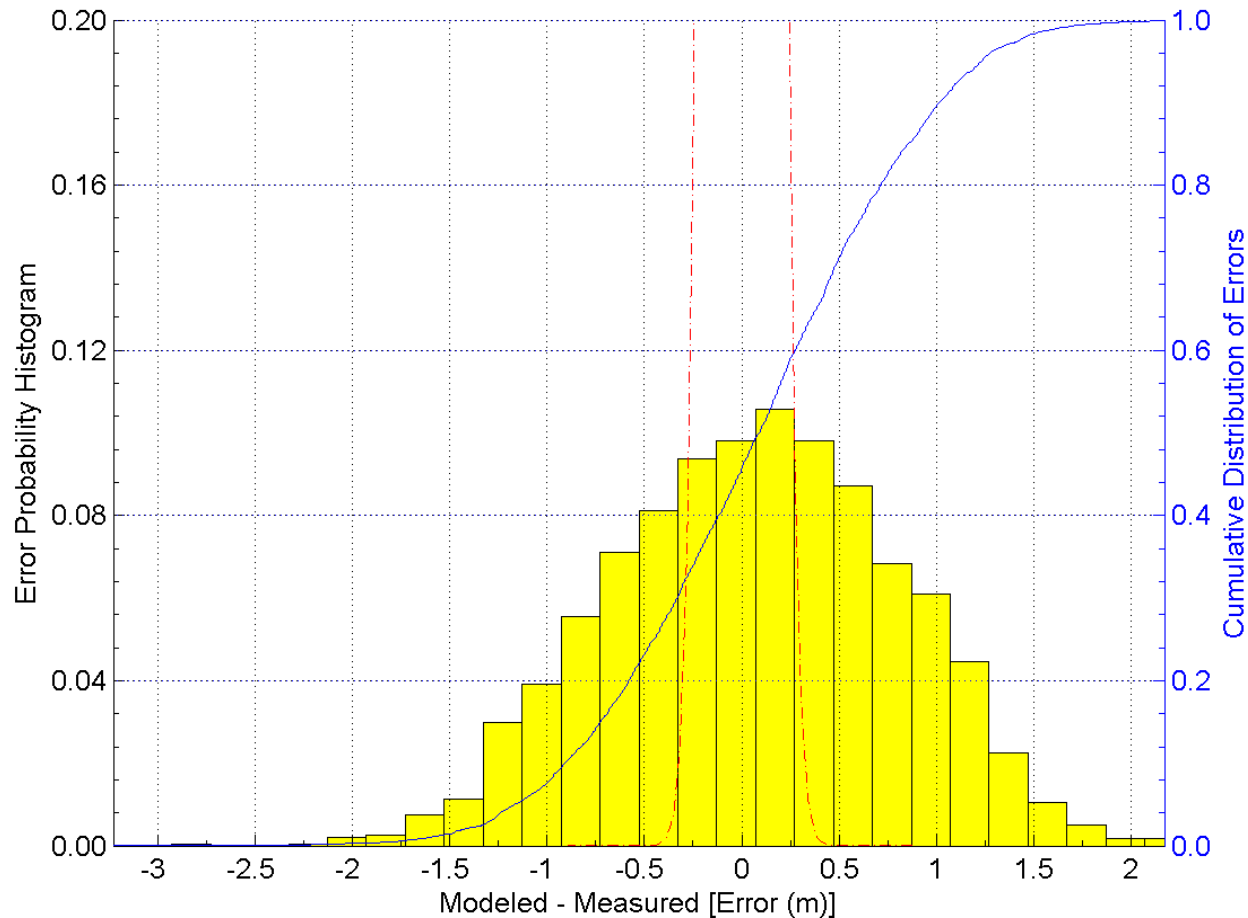


Figure TFIELD 5-25. Histogram of Steady-state Head Errors for the 100 Selected Fields (No SNL-6 or SNL-15). Red dashed line is the  $\pm 3\sigma$  section of the measurement error PDF. The slight skew to right is an artifact of the binning.

## 1 **TFIELD-6.0 Culebra T-Field Mining Modifications**

2 The work described in Section TFIELD-6.0 was completed under AP-144, Analysis Plan for the  
3 Calculation of Culebra Flow and Transport for CRA-2009 PABC (Kuhlman 2009). The  
4 modifications used for CRA-2009 PABC still apply to CRA 2014, and are therefore discussed  
5 here.

6 PA models two categories of mining-impacted transmissivity fields: partial mining with only  
7 mining outside the LWB, and full mining with regions both inside and outside the LWB mined.

8 The CRA-2009 PABC Culebra T-field mining modifications basically follow the procedure used  
9 in CRA-2004 PABC (Lowry and Kanney 2005), with two exceptions: 1) a new definition of the  
10 region containing minable potash is used, and 2) the new T-fields in Sections TFIELD-3.0  
11 through TFIELD-5.0 are used as inputs. The procedure for the mining modification portion of  
12 the analysis is summarized below:

- 13 1. Obtain the sampled values for the random mining modification factor (100 vectors  $\times$  3  
14 replicates);
- 15 2. Map potential areas of future potash mining onto the groundwater modeling domain for  
16 both full- and partial-mining scenarios;
- 17 3. Apply the mining modification factor to the 100 stochastically calibrated T-fields from  
18 AP-114 Task 7 (Hart et al. 2009), producing 600 mining-modified T-fields (100 vectors  $\times$   
19 2 mining scenarios  $\times$  3 replicates);
- 20 4. Perform steady-state flow simulations for each of the 600 mining-modified T-fields using  
21 MODFLOW-2000; and
- 22 5. Perform particle tracking using the new mining-affected flow-fields to determine  
23 advective travel times to the WIPP LWB.

## 24 **TFIELD-6.1 Overview**

25 Potash mining in the region surrounding the WIPP involves underground excavation in the  
26 McNutt Potash zone of the upper Salado Formation, which is located stratigraphically above the  
27 WIPP repository horizon but below the Culebra Member of the Rustler Formation (see Figure  
28 TFIELD 2-1). It is hypothesized that subsidence due to collapse of the underground voids  
29 created in the McNutt potash zone during mining will lead to increased permeability in the  
30 Rustler Formation, due to increased fracturing, similar to the Salado dissolution zone effects in  
31 Figure TFIELD 2-2. The purpose of the mining scenario calculations is to determine the impact  
32 of potash mining on groundwater flow directions and transport velocities in the Culebra. This  
33 analysis largely represents a re-application of the methods used in CRA-2004 PABC (Lowry and  
34 Kanney 2005), with a few minor exceptions:

- 1     1. The definition of the regions where minable potash is believed to exist has been updated,  
2     as obtained from the Bureau of Land Management (BLM) (Cranston 2009).
- 3     2. The configuration of the MODFLOW model that mining modifications are being applied  
4     to has changed (see Sections TFIELD-3.0 through TFIELD-5.0).
- 5     3. The way the mining-modified areas interact with specified head areas of the flow model  
6     has changed, due to the change in the boundary conditions (there were no specified head  
7     areas inside the CRA-2004 PABC MODFLOW model).

8     This section describes the CRA-2009 PABC effort in characterizing mining effects in the  
9     Culebra and highlights the differences and additions relative to past calculations (Ramsey and  
10    Wallace 1996; Lowry 2003a, Lowry 2003b, and Lowry 2004). The reader is encouraged to  
11    review the past documents for further background information. There have been no changes to  
12    the mining modifications procedure or data for CRA-2014 since CRA-2009 PABC.

13    Starting with the 100 calibrated T-fields from Section TFIELD-5.0, T-fields are modified to  
14    reflect the effects of mining by multiplying the transmissivity value in cells that lie within  
15    designated mining zones by a random factor uniformly sampled between 1 and 1000. The range  
16    of this factor is set by the U.S. Environmental Protection Agency (EPA) in regulation 40 CFR  
17    194.32(b) (U.S. EPA 1996). The scaling factor for each T-field is provided by Latin hypercube  
18    sampling (Kirchner 2010).

19    A forward steady-state flow simulation is run for each new T-field under each mining scenario  
20    (full and partial) across three replicates of mining factors, resulting in 600 simulations. Particle  
21    tracking is performed on both the 100 original and 600 modified flow-fields to compare the flow  
22    path and groundwater travel time from a point above the center of the WIPP disposal panels to  
23    the LWB. Cumulative distribution functions (CDFs) are produced for each mining scenario and  
24    compared to the undisturbed scenario. The CDFs indicate the probability a conservative tracer  
25    (i.e., a marked water particle) would reach the WIPP LWB during a given interval of time,  
26    flowing in the Culebra under a natural gradient. In addition to comparing travel times, particle-  
27    tracking directions are also examined to determine the effect on the regional flow direction in the  
28    WIPP area due to mining.

## 29    **TFIELD-6.2 Model Domain, Boundary, and Initial Conditions**

30    The eastern limit of the MODFLOW model domain used in the CRA-2009 PABC analysis (Hart  
31    et al. 2008) was extended eastward, compared to the MODFLOW domain used in the CRA-2004  
32    PABC analysis. This change was made to locate the boundary in an area where halite is present  
33    in all of the non-dolomite members of the Rustler Formation, simplifying the specification of the  
34    eastern model boundary condition. See Section TFIELD-3.1 for CRA-2009 PABC MODFLOW  
35    model construction details.

### 36    **TFIELD-6.2.1 Boundary and Initial Conditions**

37    Like the model domain and discretization, the boundary and initial conditions used in CRA-2009  
38    PABC are described fully in AP-114 Task 7 (Hart et al. 2009). Regional flow rates within the

1 flow model are controlled by the boundary conditions and the hydraulic conductivity  
2 distribution. The regional gradient across the domain was approximately

3 
$$(943.9 \text{ m} - 911.6 \text{ m})/30.7 \text{ km} = 0.00105 \quad (\text{TFIELD 6.1})$$

4 The gradient across the model domain was computed by averaging the constant heads along the  
5 northernmost portion of the northern boundary (row 1, columns 1-140, 943.9 m), subtracting the  
6 average heads along the entire southern boundary (911.6 m), and dividing by the north-south  
7 model domain extent (30.7 km). It was assumed that mining impacts would not significantly  
8 change this regional gradient and thus the specified initial conditions for the mining scenarios are  
9 identical to those in AP-114 Task 7 (Hart et al. 2009). In addition, the CCA, CRA-2004, and  
10 CRA-2004 PABC all used this same conceptualization (keeping the outer boundary conditions  
11 fixed between the mining and non-mining scenarios). The same conceptualization was  
12 maintained in the CRA-2009 PABC model to facilitate comparisons between the different  
13 models.

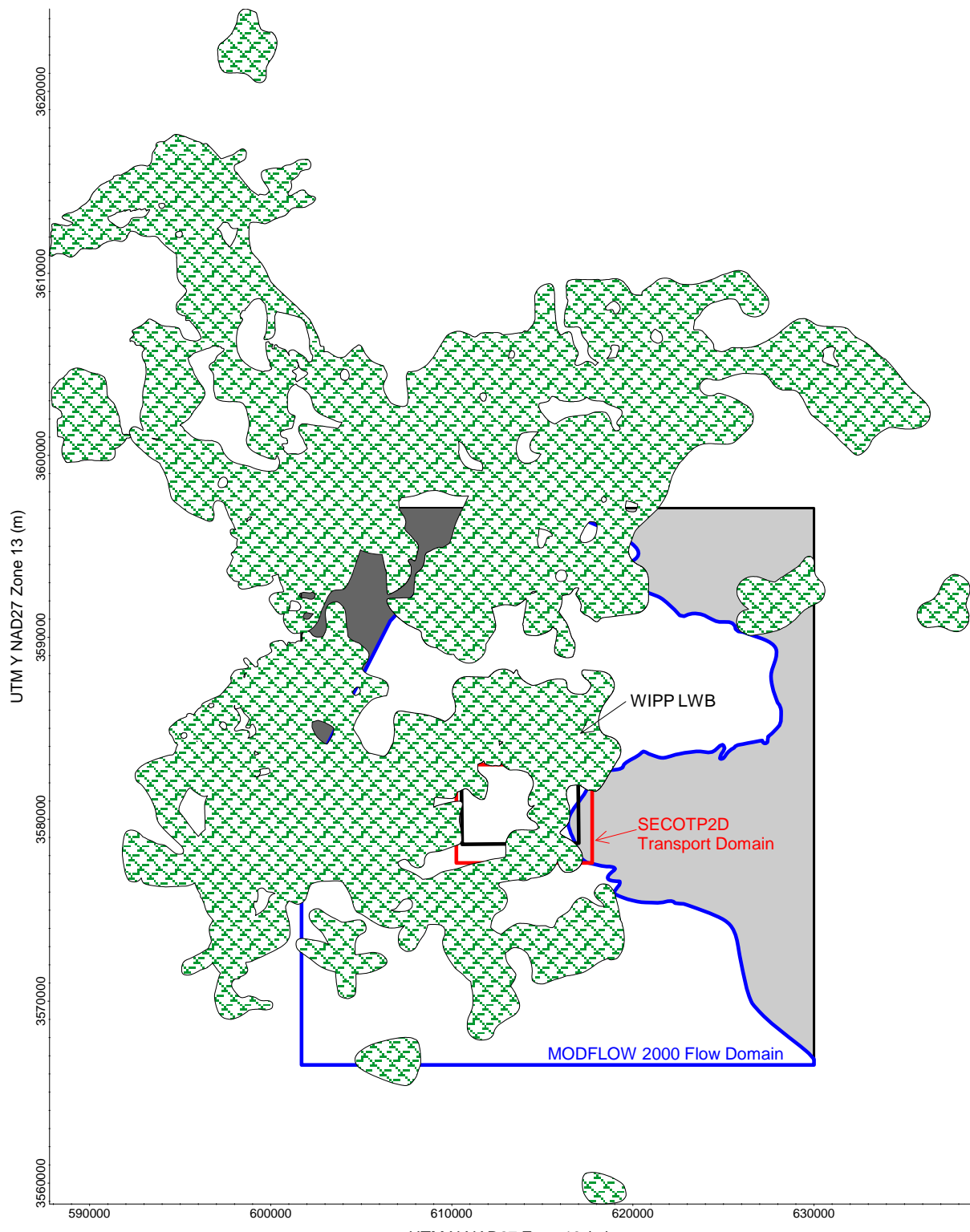


**Figure TFIELD 6-1. Comparison of Minable Potash Area to the Flow and Transport Modeling Domains. Green hatches represent minable potash area (Cranston 2009).**

## 1 TFIELD-6.2.2 Determination of Potential Mining Areas

The 2009 version of the BLM map delineating distribution of minable potash ore was obtained from BLM as an ESRI shapefile (Cranston 2009), plotted in Figure TFIELD 6-1. The process to convert this shapefile to a grid of integers corresponding to Culebra MODFLOW model cells (indicating whether a model cell was affected by mining or not) is explained in Appendix 1 of Kuhlman (Kuhlman 2010).

7 Since the potash-mining horizon is located in the Salado Formation below the Culebra, the areas  
8 disturbed by mining activities in the Culebra are larger than mined areas in the Salado due to  
9 angle-of-draw effects. Subsidence effects will not propagate up vertically, but instead will  
10 propagate up and out at 45° angles between horizontal and vertical. Based on an average distance  
11 from the McNutt potash zone to the Culebra, a 253-m-wide collar was added to the mining-  
12 impacted areas (consistent with that done previously; see Ramsey and Wallace (Ramsey and  
13 Wallace 1996) and Bertram (Bertram 1995). This was considered a conservative estimate of the  
14 angle-of-draw effects. To accommodate the angle of draw, the mining zone boundaries, as  
15 overlaid on the current model grid, were extended outward three cells (300 m) in the  $x$ - and  $y$ -  
16 directions, and two cells (283 m) in the diagonal directions (see Figure TFIELD 6-2 for an  
17 illustration of the mining-expansion stencil).

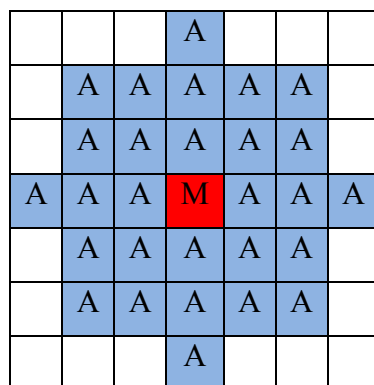
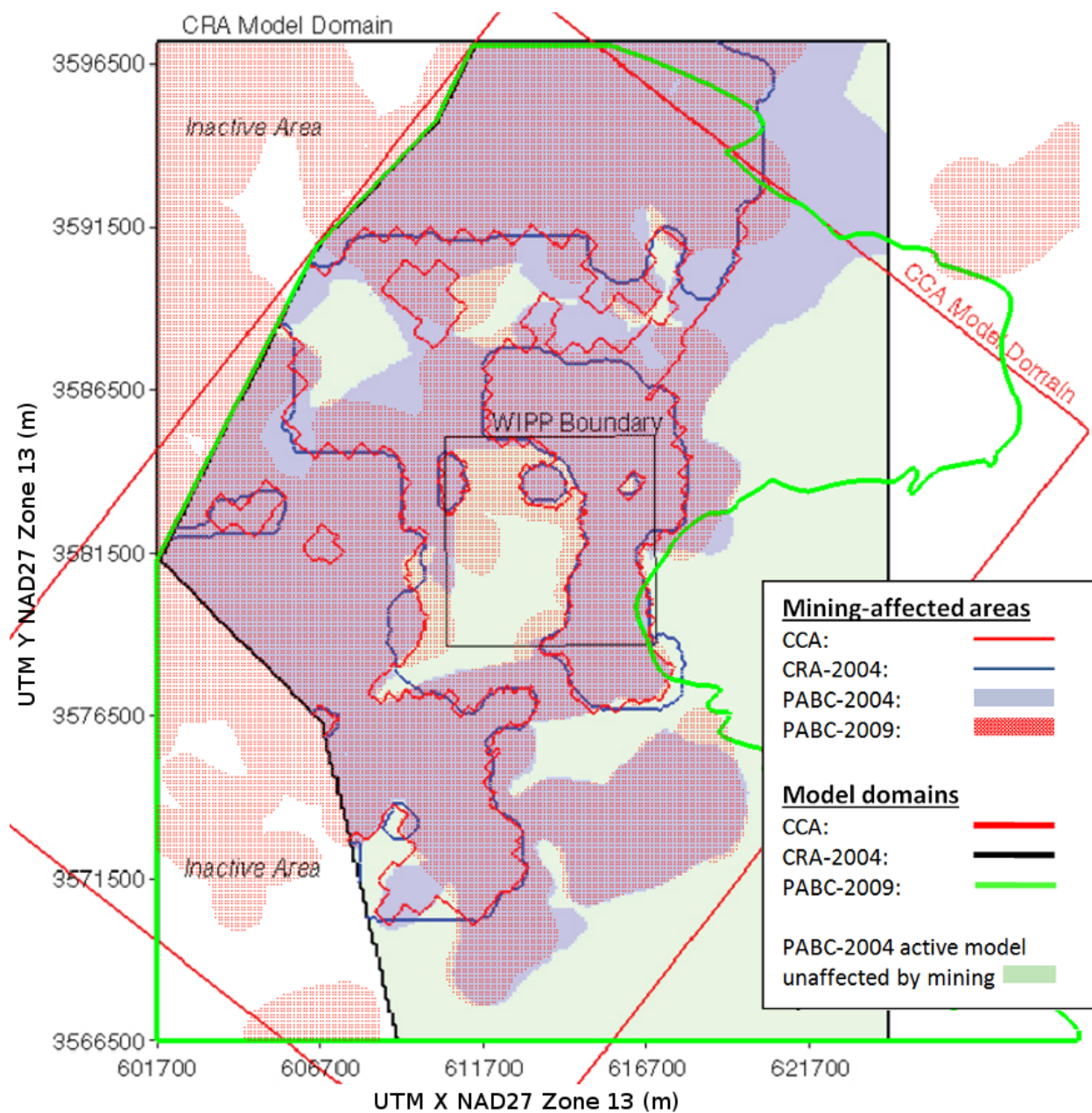


**Figure TFIELD 6-2. Stencil Used to Model Cells Affected by Mining-related Subsidence (Blue Cells with A) Due to Mining in Red "M" Cell, Using 45° Angle of Draw**

21 Figure TFIELD 6-3 shows the CRA-2009 PABC modeling domain and mining zones for the  
22 full-mining case in comparison to the 1996 CCA and the CRA-2004 delineations. The  
23 comparison of the current and previous partial-mining cases is shown in Figure TFIELD 6-4. A  
24 close-up of the WIPP site and the distribution of minable potash is shown in Figure TFIELD 6-5,  
25 which illustrates how the definition inside the WIPP LWB has changed significantly since CRA-  
26 2004 PABC. For CRA-2004 PABC, the closest minable potash was approximately 1,230 m from  
27 the center of the WIPP panels in the southeast direction; for CRA-2009 PABC, this distance was  
28 reduced to approximately 670 m (in a more easterly direction).

29 The output of this mining-area delineation was a mining effects indicator field. A value of 1  
30 means the model cell lies within a potential mining-affected zone, and a value of 0 means that it  
31 is outside a potential mining-affected zone.



1  
2 **Figure TFIELD 6-3. Definitions of Mining-affected Areas in Full-mining Scenario**  
3 **Between Current and Previous Models. Base image is Figure 3.2**  
4 **from Lowry and Kanney (2005). CRA-2009 PABC mining area**  
5 **(red stippled area) and model domain (green line) definitions are**  
6 **current definitions used in CRA-2014.**

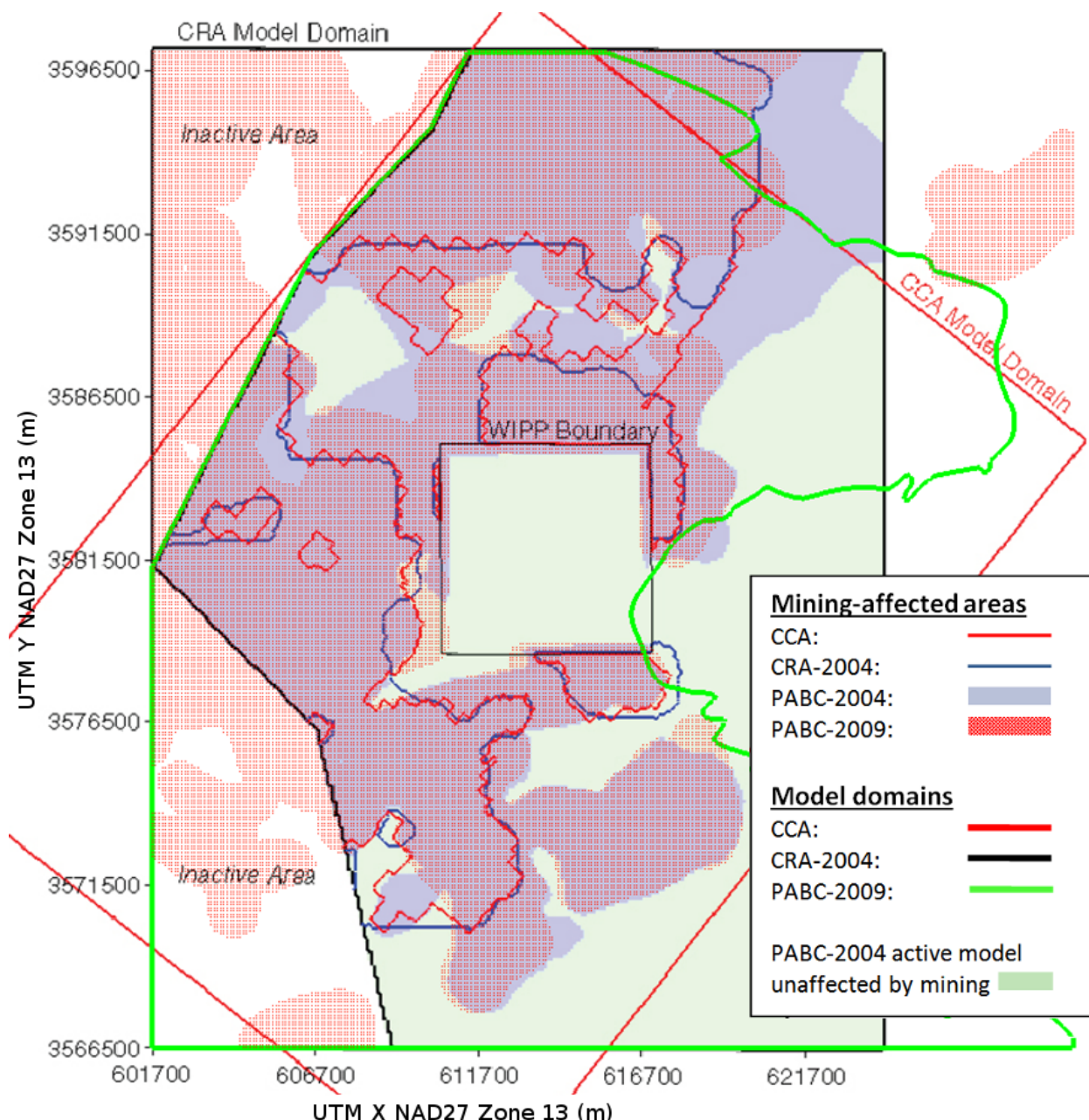
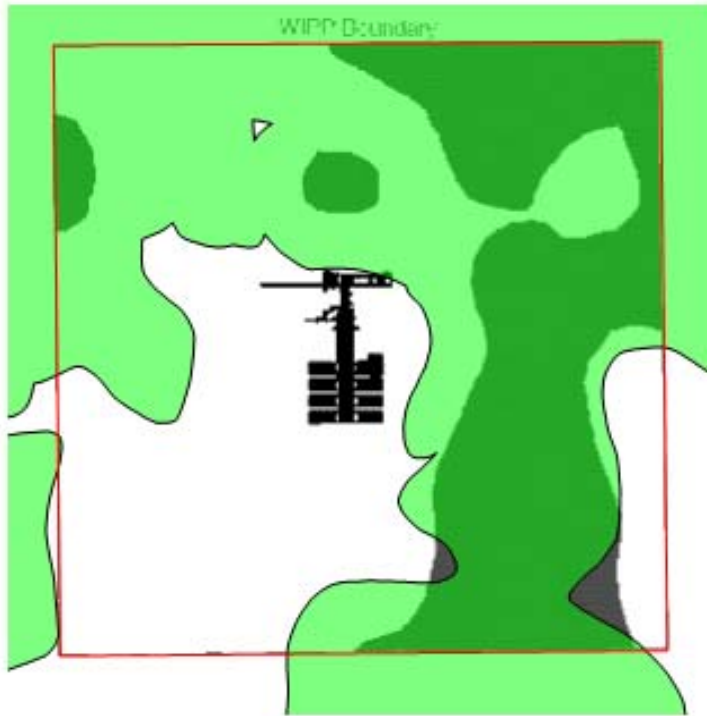


**Figure TFIELD 6-4. Definitions of Partial-mining-affected Areas Between Current and Previous Applications. Base image is Figure 3.3 from Lowry and Kanney (2005). CRA-2009 PABC mining area (red stippled area) and model domain (green line) definitions are current definitions used in CRA-2014.**



1  
 2 **Figure TFIELD 6-5. Comparison of Minable Potash Distribution Inside the WIPP**  
 3 **LWB for CRA-2004 PABC (Dark Gray) and CRA-2009**  
 4 **PABC (Translucent Green). The WIPP repository plan is**  
 5 **shown for comparison, from Figure 3.6 of Lowry and**  
 6 **Kanney (2005).**

### 7 **TFIELD-6.2.3 Use of Mining Zones in Forward Simulations**

8 The calibration process in Section TFIELD-5.0 produced 100 sets of  $T$ ,  $A$ ,  $S$ , and  $R$  fields that  
 9 each minimize the error between observed and model-calculated head distributions. To simulate  
 10 the effects of mining, the field of  $T$  values from each realization was multiplied by its own  
 11 unique mining scaling factor in areas of potential mining, and MODFLOW was re-run with these  
 12 mining-modified  $T$ -fields to produce the mining-affected head and flow distributions. The other  
 13 parameter fields ( $S$ ,  $A$ , and  $R$ ) were not modified in the process. The cell-by-cell flow budget  
 14 files were used in particle tracking and radionuclide transport calculations. Three different sets of  
 15 mining factors were used, each set forming a replicate (given here as R1, R2, and R3). Thus, for  
 16 each mining scenario (full and partial), three sets of 100 mining-altered  $T$ -fields and related cell-  
 17 by-cell flow budgets were produced.

### 18 **TFIELD-6.2.4 Particle-Tracking Simulations**

19 In each realization, a single conservative particle was tracked from the UTM NAD27 coordinate  
 20  $x = 6,135,975$  m,  $y = 35,813,852$  m (i.e., the Culebra location of monitoring well C-2737,  
 21 directly above the center of the WIPP waste panels) to the LWB for each combination of  $T$ -field,  
 22 replicate, and mining scenario using the SNL-developed particle-tracking code DTRKMF. Two  
 23 main outputs were generated from the suite of particle tracks. First, plots were constructed

1 showing the individual tracks for all 100 T-fields in each scenario for each replicate (six plots  
2 total). This allows visual comparison of the prevailing flow directions for the full- and partial-  
3 mining scenarios and the qualitative comparison of the variability of the tracking direction.  
4 Secondly, CDFs were constructed for each replicate and scenario, which describe the probability  
5 that a water particle will cross the LWB in a given amount of time. The six plots and the CDFs  
6 are presented in Section TFIELD-6.3.

## 7 **TFIELD-6.3 Particle-Tracking Results**

8 Particle tracks were computed using DTRKMF (Rudeen 2003), which uses the binary cell-by-  
9 cell flow budget files produced by MODFLOW-2000. In flow calculations, the full 7.75 m  
10 thickness of the Culebra is used, while for transport and particle-tracking purposes the thickness  
11 is reduced to 4.0 m to focus all flow through the lower, more permeable portion of the Culebra  
12 (Holt 1997). A value of 16% porosity was used for the particle-tracking calculations (parameter  
13 DPOROS). Porosity directly affects transport, but is not needed for the calibration of the flow  
14 model.

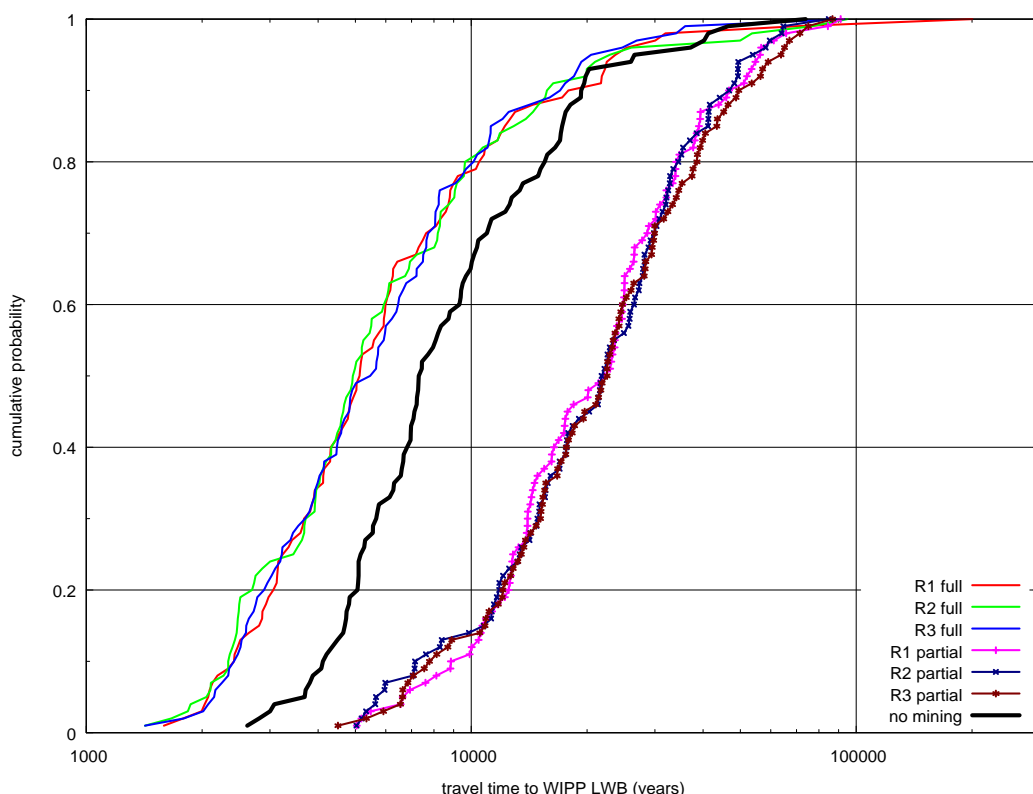
15 Particle tracking was performed to allow plotting and quantitative comparison between the two  
16 mining scenarios and the non-mining scenario, which was not used in the PA SECOTP2D  
17 radionuclide transport calculations. The particle-tracking results illustrate the advective pathway  
18 taken by a marked water particle. They do not take into consideration retardation, dispersion, or  
19 molecular diffusion, which may be accounted for in PA by radionuclide transport. The particle  
20 tracks also allow easier comparison of the 600 results (each a 1D trace) in a single plot, in  
21 contrast to showing 600 plots of concentrations (each a 2D field) produced from SECOTP2D.

### 22 **TFIELD-6.3.1 Particle Travel Times**

23 Compared to the non-mining scenario (results already given in AP-114 Task 7 (Hart et al.  
24 2009)), the travel times for the partial-mining scenarios are longer, while travel times for the full-  
25 mining scenarios are shorter. The median travel time across all three replicates for the full-  
26 mining scenario is approximately 0.689 times the median travel time of the non-mined scenario  
27 (see Table TFIELD 6-1, Figure TFIELD 6-6, and Figure TFIELD 6-7 for summary statistics and  
28 comparison to CRA-2004 PABC results). All advective particle travel times are plotted, but it  
29 should be noted that the regulatory limit for radionuclide transport modeling is 10,000 years,  
30 taking into consideration retardation, diffusion, and dispersion (which do not apply to particle  
31 track modeling). The median travel time across all three replicates for the partial-mining scenario  
32 is 3.034 times greater than for the non-mining scenario. For CRA-2004 PABC, travel times in  
33 both the full- and partial-mining scenarios were slower (longer) than for the non-mining  
34 scenario. The CDFs for the full-, partial-, and non-mining scenarios are shown in Figure TFIELD  
35 6-6. Travel times from CRA-2009 PABC for particles in the non-mining scenario are closer to  
36 CCA travel times than those from CRA-2004 PABC (Figure TFIELD 6-7).

1      **Table TFIELD 6-1. Particle-tracking Travel-time Statistics from Center of the WIPP**  
 2      **Panels to the WIPP LWB (Years). Global statistics for full and**  
 3      **partial mining include 300 realizations, while no mining only**  
 4      **includes 100 realizations.**

		CRA-2009 PABC			CRA-2004 PABC		
Replicate	Statistic	Full	Partial	No Mining	Full	Partial	No Mining
R1	Median	5,138	22,581	N/A	64,026	117,815	
	Max	200,260	91,119		2,175,165	2,727,191	
	Min	1,591	5,042		2,130	5,185	
R2	Median	4,956	21,999	N/A	80,801	148,489	
	Max	94,852	84,929		2,059,263	1,667,084	N/A
	Min	1,421	5,037		2,463	4,855	
R3	Median	5,560	22,537	N/A	74,315	118,919	
	Max	93,172	86,758		1,779,512	3,128,693	
	Min	1,421	4,505		2,507	3,314	
Global	Median	5,084	22,376	7,374	70,170	131,705	18,289
	Max	200,260	91,119	73,912	2,175,165	3,128,693	101,205
	Min	1,421	4,505	2,618	2,130	3,314	3,111



6      **Figure TFIELD 6-6. CDF of Advective Particle Travel Times From the Center of the**  
 7      **WIPP Waste Panels To the WIPP LWB for Full, Partial, and**  
 8      **Non-mining Scenarios**

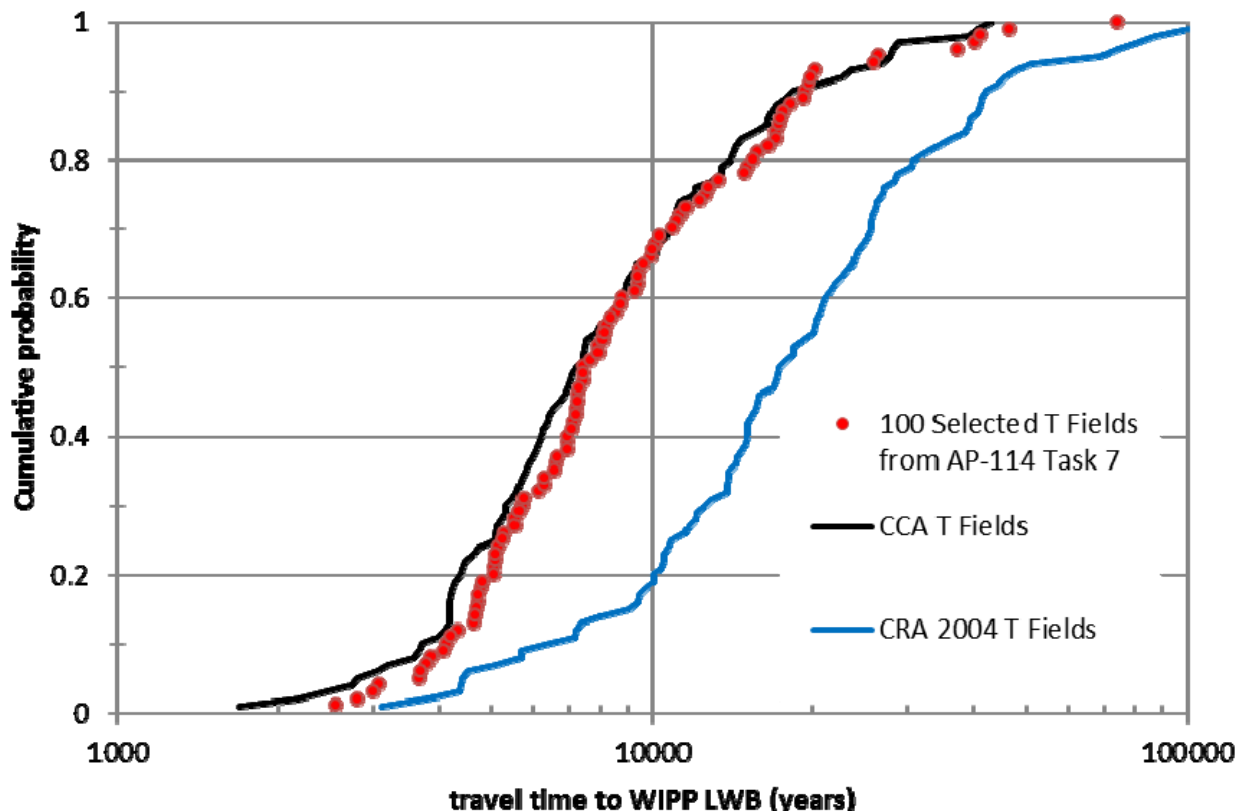


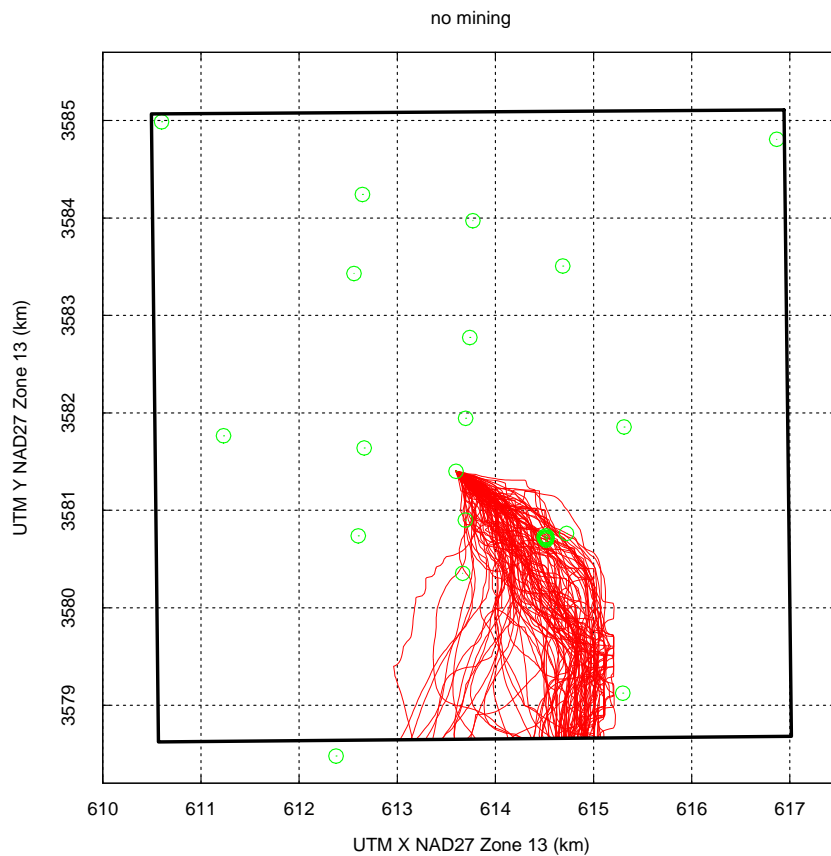
**Figure TFIELD 6-7. Comparison of Advective Particle Travel Time CDFs for Non-mining Scenarios of CRA-2009 PABC, CRA-2004 PABC, and CCA. Travel times are from the center of the WIPP waste panels to the WIPP LWB.**

### TFIELD-6.3.2 Flow Directions

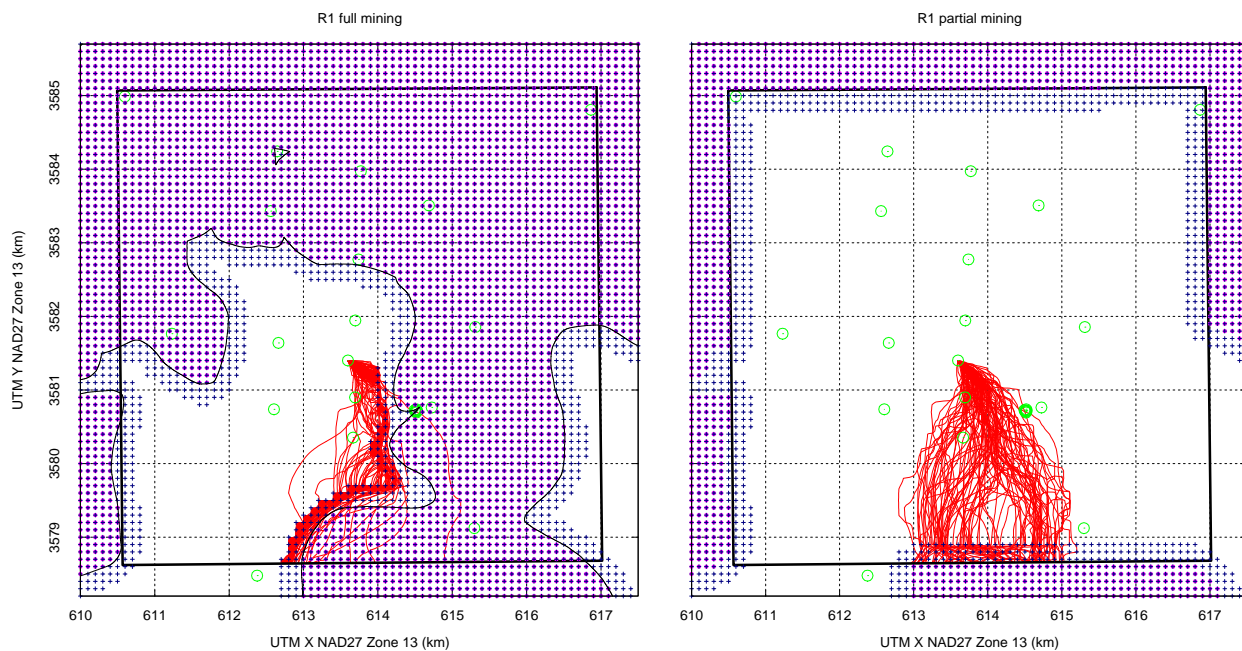
The particle track directions for the non-, full-, and partial-mining scenarios for CRA-2009 PABC are illustrated in Figure TFIELD 6-8 to Figure TFIELD 6-11. Figure TFIELD 6-13 shows the non-mining case particle tracks all the way to the edge of the MODFLOW model domain, rather than only to the WIPP LWB. Like past mining scenario calculations (i.e., CRA-2004 PABC), there is a strong similarity between the three replicates (R1, R2, and R3) for each scenario (full or partial mining), although the travel directions for the CRA-2009 PABC are different than for the CRA-2004 PABC (Lowry and Kanney 2005). A larger amount of minable ore exists inside the WIPP LWB, especially the ore immediately to the east of the particle release point. This leads to different effects of full mining on travel times compared to CRA-2004 PABC.

The high- $T$  pathway in the southeastern portion of the WIPP site (Figure TFIELD 5-15) was more accurately represented in CRA-2009 PABC results, compared to CRA-2004 PABC results. This difference in the underlying flow field calibration is another source of difference between CRA-2004 PABC and CRA-2009 PABC particle-tracking results.

1 In CRA-2009 PABC, nearly all particles immediately go east to this boundary and then move  
 2 south along it towards to the edge of the LWB at approximately  $x = 612.75$  km (see Figure  
 3 TFIELD 6-9 and Figure TFIELD 6-12). This is in contrast to the partial-mining scenario where  
 4 the tracking directions are more similar to the non-mining scenario, but more evenly distributed  
 5 spatially along the southern boundary. In the non-mining scenario, most of the particles exit near  
 6 the high-transmissivity zone at approximately  $x = 615$  km.



7  
 8 **Figure TFIELD 6-8. 100 Particle Tracks for Non-mining Scenario. Black box is the**  
 9 **WIPP LWB, green circles are Culebra monitoring well locations.**



1 **Figure TFIELD 6-9. 100 Particle Tracks Each for R1 Full and Partial Mining**  
2 **Scenarios. Small magenta squares and blue crosses indicate**  
3 **centers of MODFLOW cells located within potash and mining-**  
4 **affected areas, respectively; thin black line is minable potash.**

5

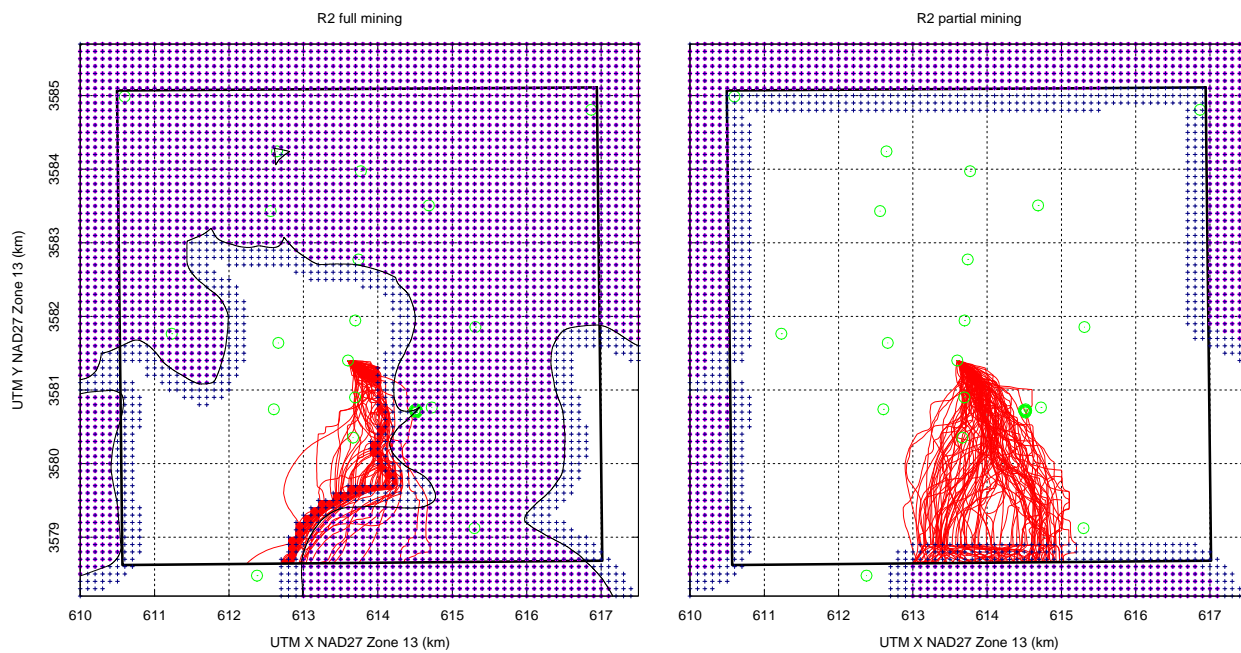
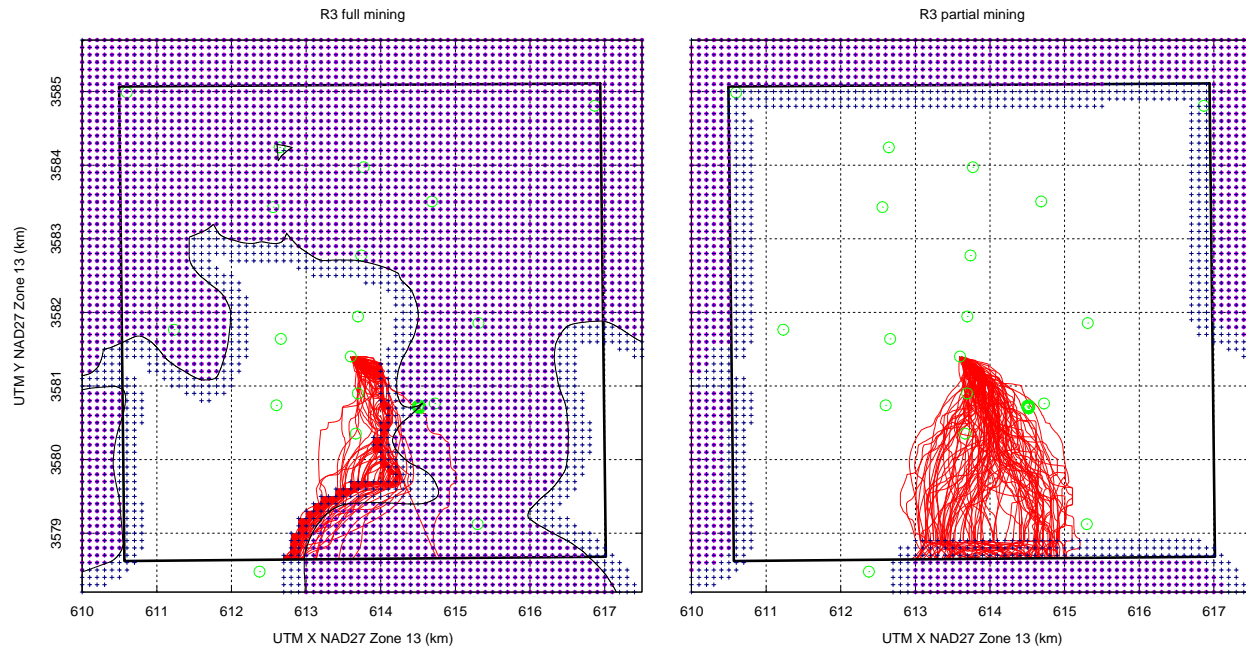
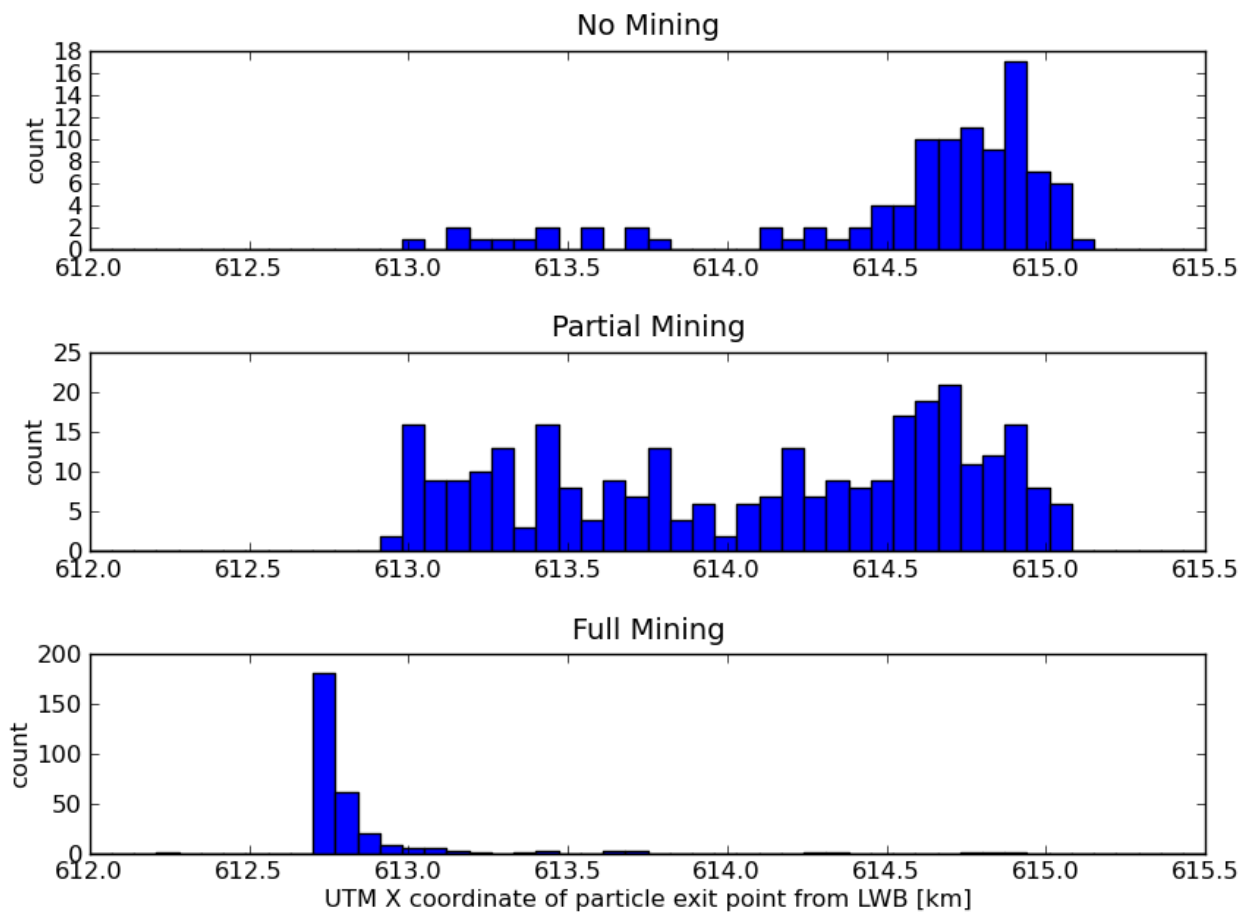


**Figure TFIELD 6-10.** 100 Particle Tracks Each for R2 Full- and Partial-mining Scenarios. Small magenta squares and blue crosses indicate centers of MODFLOW cells located within potash and mining-affected areas, respectively; thin black line is minable potash.



1 **Figure TFIELD 6-11. 100 Particle Tracks Each for R3 Full- and Partial-mining**  
 2 **Scenarios. Small magenta squares and blue crosses indicate**  
 3 **centers of MODFLOW cells located within potash and mining-**  
 4 **affected areas, respectively; thin black line is minable potash.**

5 High- $T$  areas corresponding to the mining-affected zones create preferential pathways through  
 6 the system (e.g., see oranges and yellows in Figure TFIELD 6-14). These preferential pathways  
 7 result in higher velocities and flow rates through the mining zone and therefore relatively slower  
 8 velocities in the non-mined areas. In the partial-mining scenario, where there is no mining inside  
 9 the WIPP LWB, the preferential pathway goes “around” the LWB, rather than through it (similar  
 10 to behavior seen in both mining scenarios for CRA-2004 PABC). In the full-mining scenario, the  
 11 potentially mined regions are closer to the release point than in CRA-2004 PABC (see Figure  
 12 TFIELD 6-5 for comparison), giving the particles a high- $T$  pathway from the release point to the  
 13 LWB, resulting in shorter travel times than the non-mined scenario. This behavior is different  
 14 from that predicted with the CRA-2004 PABC model. A comparison of the median, maximum,  
 15 and minimum travel times for each scenario is presented in Table TFIELD 6-1.



1 **Figure TFIELD 6-12. Histograms of Particle  $x$ -coordinates at Exit Point From LWB.**  
2 Full- and partial-mining include all three replicates (note  
3 different vertical scales between plots; no mining contains 100  
4 particles while mining scenarios each include 300 particles).  
5

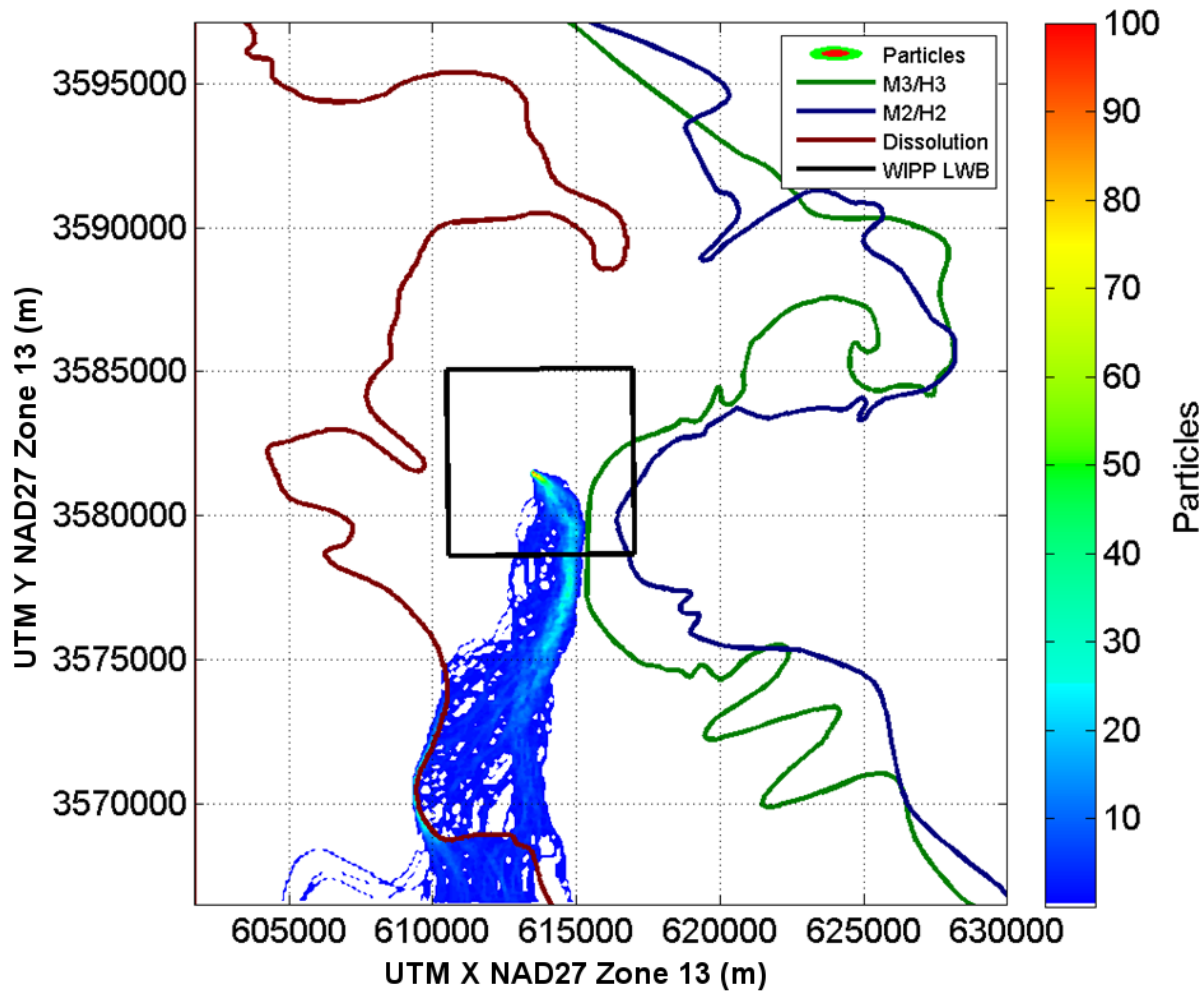
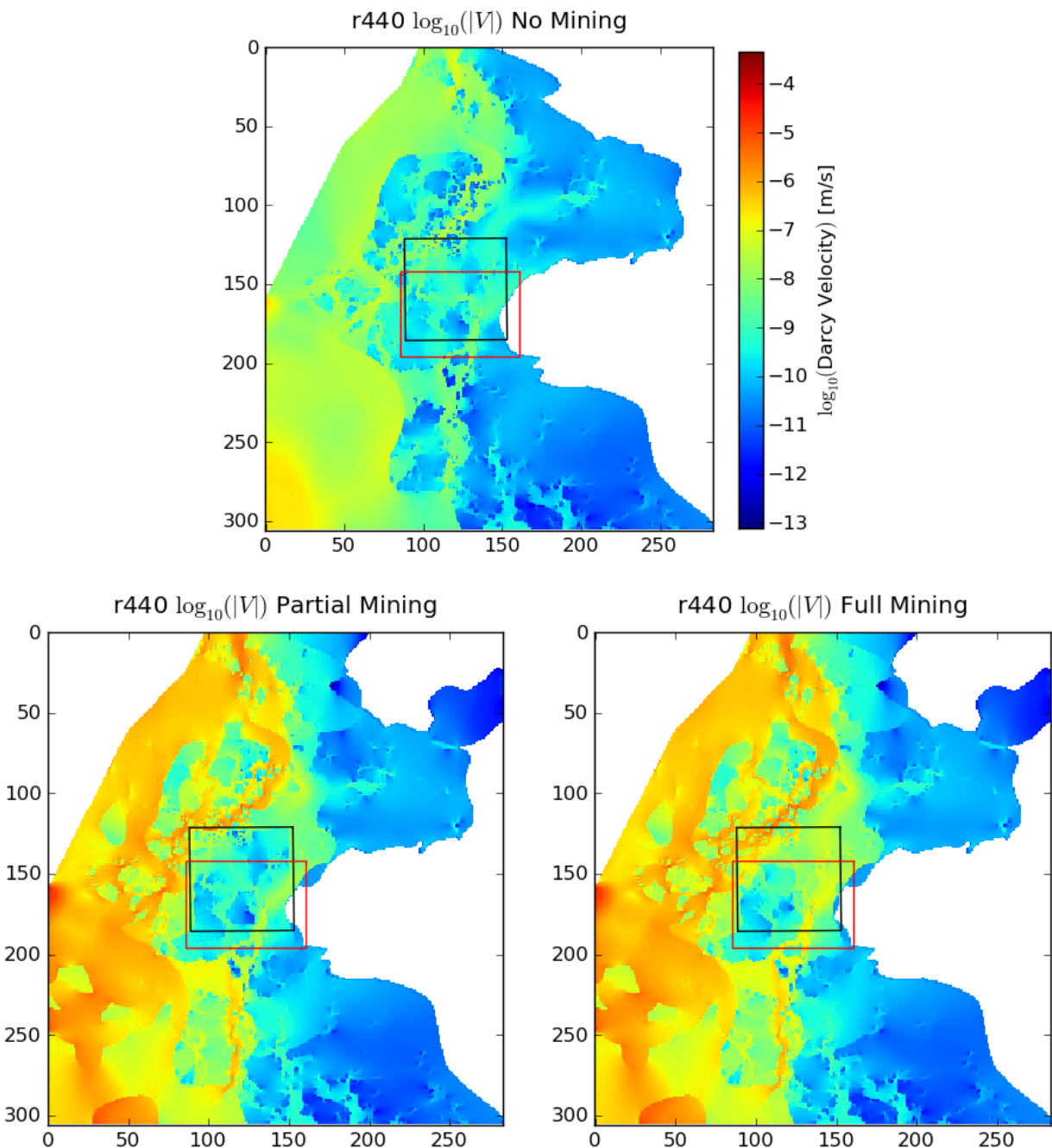


**Figure TFIELD 6-13. Particle Counts in Each Cell Across All 100 Selected Realizations for Non-mining Scenario**



1      **Figure TFIELD 6-14. Magnitude of Darcy Flux for a Single Realization (r440) for**  
2      **No, Partial, and Full-mining Scenarios Using Cell-based**  
3      **Coordinates. LWB (black) and SECOTP2D transport model**  
4      **domains (red) shown for reference.**

### 5      TFIELD-6.3.3 Particle Speeds

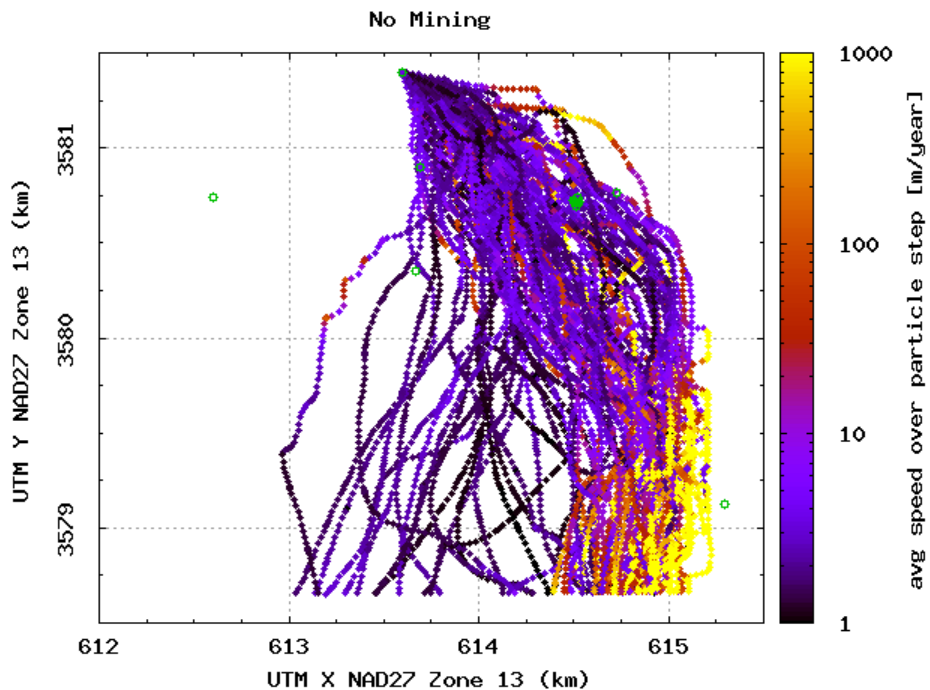
6      Instantaneous speeds (the magnitude of particle velocities) were calculated from the DTRKMF  
7      particle locations and times using backwards finite differences,

$$1 \quad v(t_{i+1}) = \frac{\sqrt{[x(t_i) - x(t_{i+1})]^2 + [y(t_i) - y(t_{i+1})]^2}}{t_{i+1} - t_i} \quad (\text{TFIELD 6.2})$$

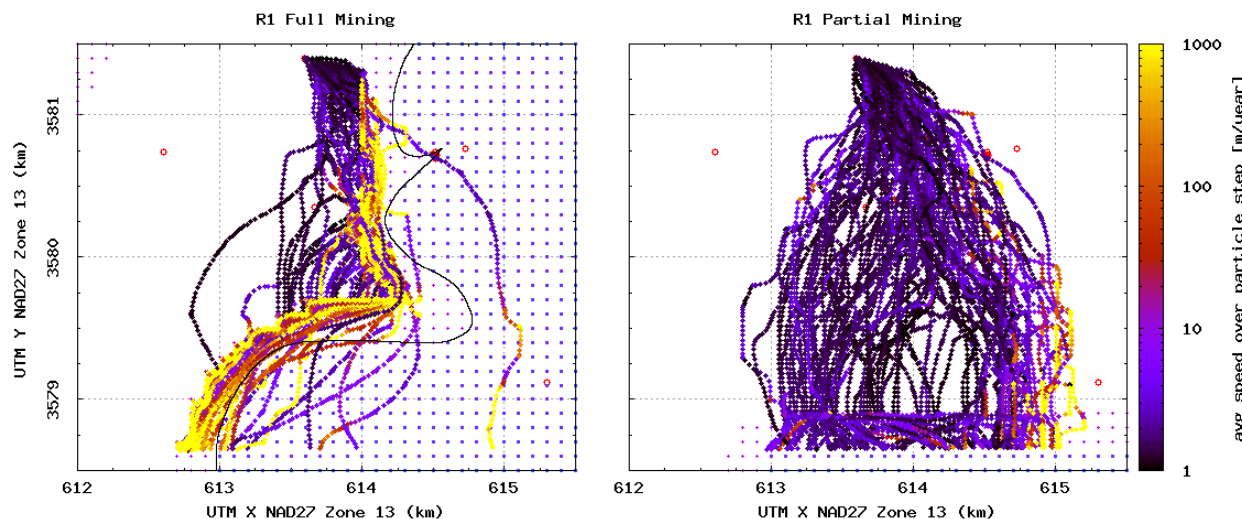
2 where a subscript  $i$  indicates the previous time step (a record or line in the DTRKMF output file)  
 3 and a subscript  $i+1$  is the current time step. This approach assumes a straight line connects the  
 4 locations at the beginning and ends of the step, so it is potentially underestimating speeds, but  
 5 step sizes are small and error should be minimal. These values should be used for qualitative  
 6 comparisons between realizations and scenarios, rather than quantitative estimates of true  
 7 particle velocities.

8 In Figure TFIELD 6-15 through Figure TFIELD 6-18, the color of the diamond indicates the  
 9 particle velocity; the dots are located at the midpoint of the step, e.g.,  
 10  $x_{\text{midpt}} = \frac{1}{2}[x(t_i) + x(t_{i+1})]$ ,  $y_{\text{midpt}} = \frac{1}{2}[y(t_i) + y(t_{i+1})]$ . In the no-mining case (Figure TFIELD 6-15),  
 11 the highest particle velocities are in the southeastern portion of the particle swarm, corresponding  
 12 to the high-transmissivity pathway (Hart et al. 2009) exiting the LWB at approximately  
 13  $x = 614,750$  m (Figure TFIELD 6-12). This high- $T$  pathway has been observed in multi-well  
 14 pumping tests, and was intentionally included in the soft data used to create the base T-fields  
 15 (Section TFIELD-4.2.3). This high- $T$  pathway was not as prevalent in the CRA-2004 PABC  
 16 model calibration results.

17 The effects of the full-mining scenario are clearly evident in the left halves of Figure TFIELD  
 18 6-16 through Figure TFIELD 6-18. High particle velocities (yellows and oranges) are found  
 19 along the margin of the mining-affected areas, where particles enter the increased- $T$  region. For  
 20 comparison, in the partial-mining scenario the particles are relatively slowed down and more  
 21 evenly distributed in the region between the release point and the southern WIPP LWB, with the  
 22 only high velocities found in the high- $T$  pathway in the southeast, similar to the no-mining  
 23 scenario (Figure TFIELD 6-15).



1  
2 **Figure TFIELD 6-15. Particle Speeds for Non-mining Scenario Computed from**  
3 **DTRKMF Results. Open symbols are Culebra well locations.**



4 **Figure TFIELD 6-16. Particle Speeds for R1, Computed From DTRKMF Results.**  
5 **Open symbols are Culebra well locations.**

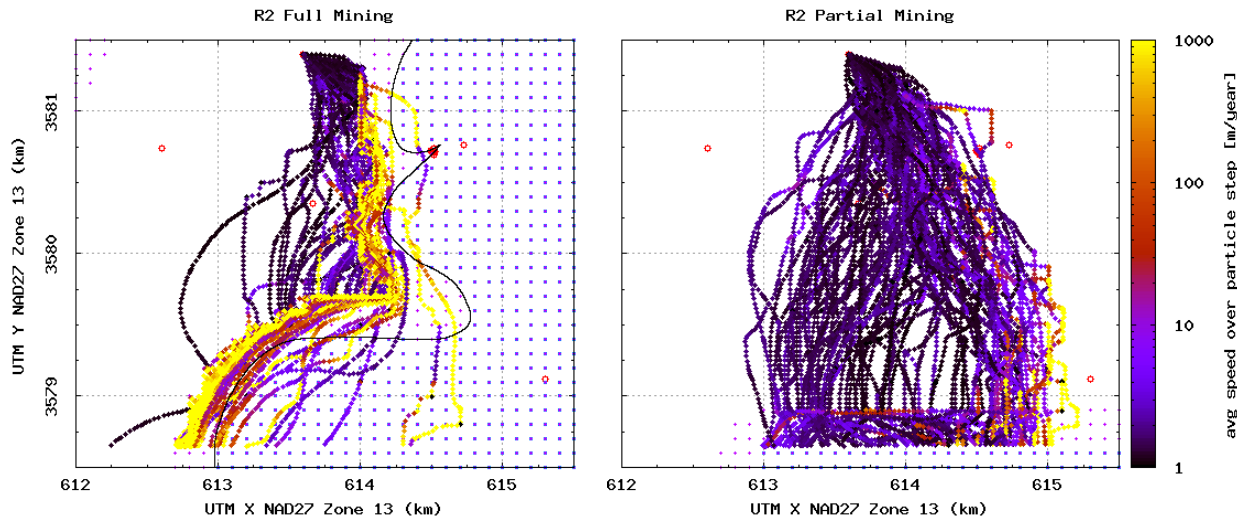


**Figure TFIELD 6-17. Particle Speeds for R2, Computed From DTRKMF Results.**  
**Open symbols are Culebra well locations.**

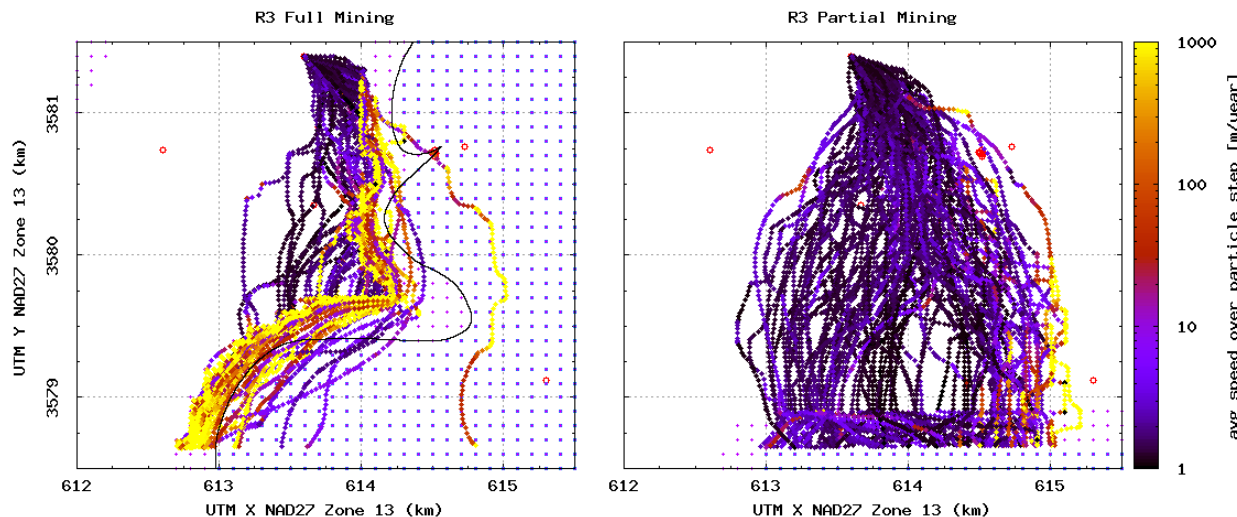
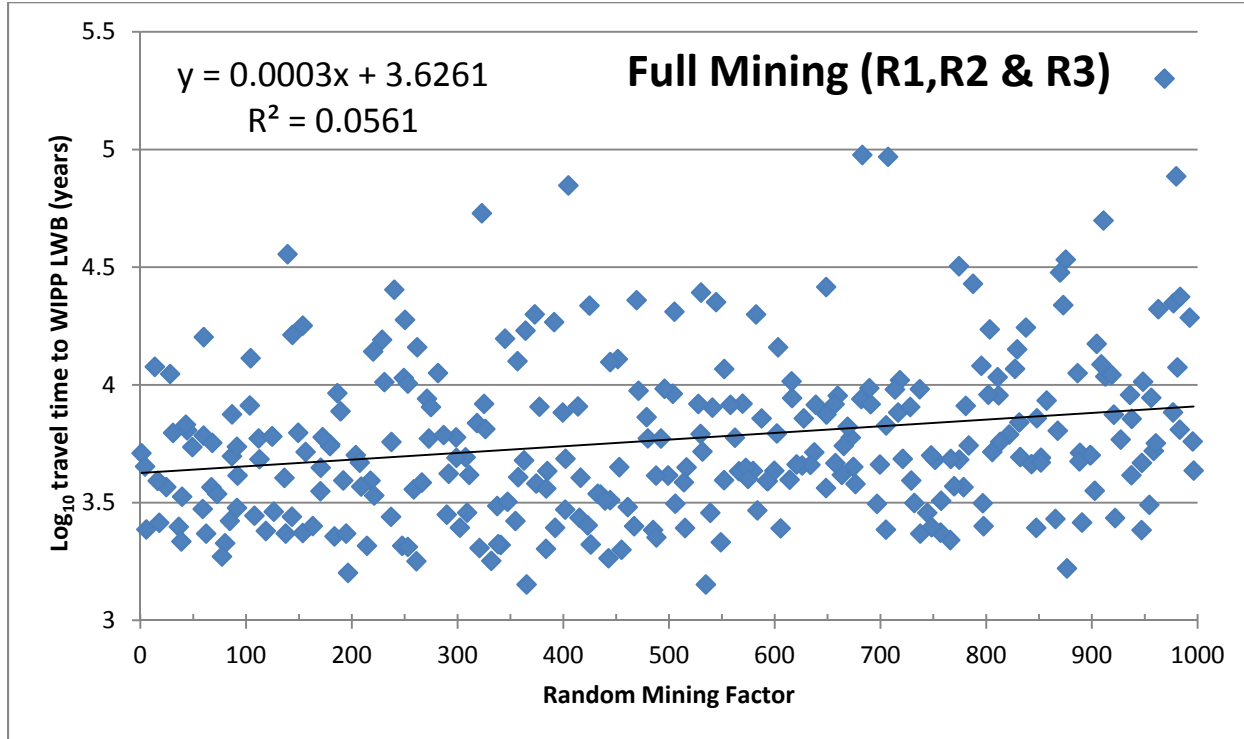


**Figure TFIELD 6-18. Particle Speeds for R3, Computed from DTRKMF Results.**  
**Open symbols are Culebra well locations.**

## TFIELD-6.3.4 Particle-Tracking Discussion

6 Correlation analysis for the CRA-2009 PABC particle-tracking calculations shows that travel  
7 time and the random mining factor have weak positive correlation with the full-mining (Figure  
8 TFIELD 6-19) or partial-mining (Figure TFIELD 6-20) scenarios. Larger mining factors are  
9 weakly correlated with longer travel times. This is similar to what was observed for CRA-2004  
10 PABC (Lowry and Kanney 2005). The high scatter in Figure TFIELD 6-19 and Figure TFIELD  
11 6-20 indicates that the transmissivity spatial distribution plays the more significant role in  
12 determining the travel time than the mining factor does. See Appendix 1 of Kuhlman (Kuhlman  
13 2010) for a cross-sectional comparison of transmissivity for each mining type, showing that the  
14 variability in the transmissivity due to calibration is on the same order as that due to mining for a

1 single realization. The mining factor plays a weak but slightly larger role in explaining the  
 2 observed variance for the partial-mining realizations (Figure TFIELD 6-20) than the full-mining  
 3 realizations (Figure TFIELD 6-19), based on the larger (but still relatively small)  $R^2$  value for the  
 4 straight-line fit of  $\log_{10}$  travel times to mining factors.



5  
 6 **Figure TFIELD 6-19. Correlation of Mining Factor and Travel Time to the WIPP**  
 7 **LWB for Full-mining Scenario (All Replicates)**

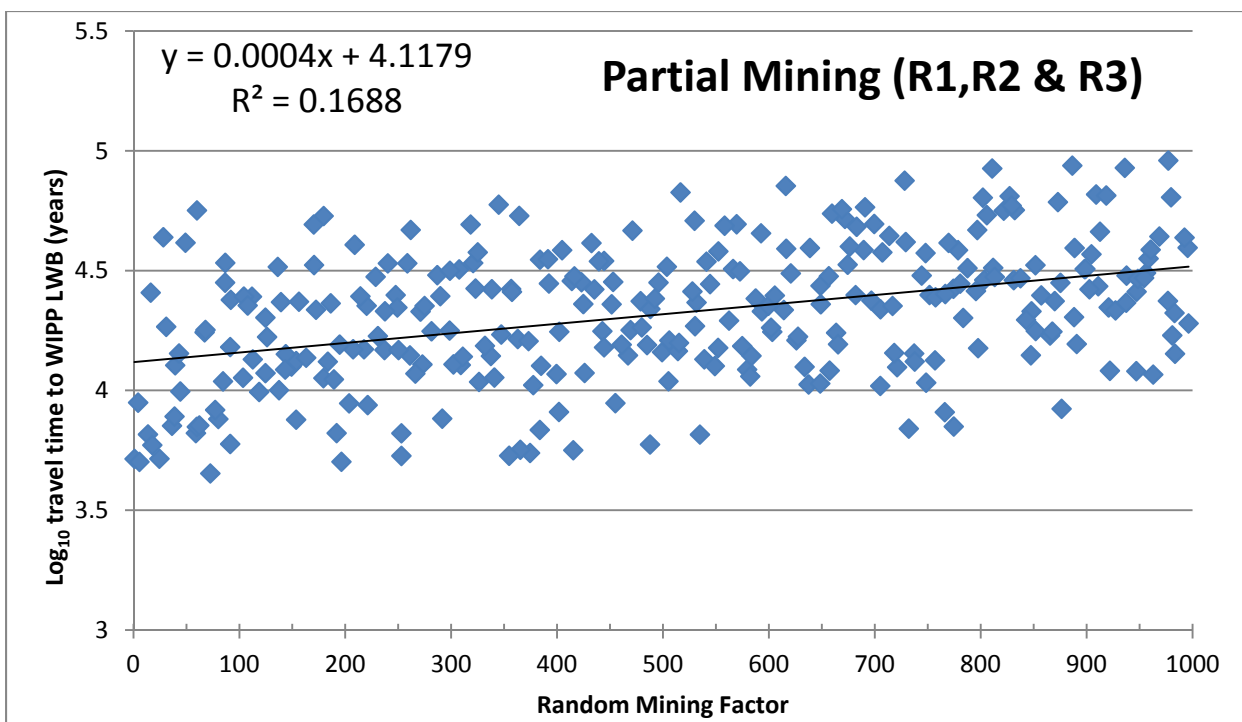


**Figure TFIELD 6-20. Correlation of Mining Factor and Travel Time to the WIPP LWB for Partial-mining Scenario (All Replicates)**

#### TFIELD-6.4 Mining Modification Summary

The 100 transmissivity fields resulting from calibration to both steady-state and transient observed freshwater heads in the Culebra (Section TFIELD-5.1) were modified to account for potential effects due to mining potash from the Salado Formation above the repository. A definition of the areal extent of minable potash was obtained from the BLM (Cranston 2009) and used to define areas where Culebra transmissivity was increased by a randomly sampled mining factor ( $1 \leq MI\_NP\_FACT \leq 1000$ ). Two mining scenarios were developed: a full-mining scenario with all minable potash removed and a partial-mining scenario with only potash outside the WIPP LWB removed.

The mining-modified transmissivities were inputs to a MODFLOW flow model, which produced budget files used by DTRKMF to compute advective particle tracks from a release point at the center of the WIPP waste panels (C-2737) to the edge of the WIPP LWB. Results show that for the partial-mining scenario, the median particle travel time of 22,376 years is 3.03 times greater than for the non-mining scenario (7,374 years); the median particle travel time for the partial-mining scenario in CRA-2004 PABC was 7.06 times greater than for the non-mining scenario. In contrast to the CRA-2004 PABC, the full-mining scenario decreased median travel time to 5,084 years, a factor of 1.45 *faster* than for the non-mining scenario; the median particle travel time for the full-mining scenario in CRA-2004 PABC was 3.84 times *slower* than for the non-mining scenario. For the partial-mining scenario, the increase in transmissivity due to mining increases the relative flow rate through the mining zones, with a corresponding decrease in flow through the non-mining zones. This decrease in flow through the non-mining zones produces longer travel times for the partial-mining scenario. For the full-mining scenario, the potash definition

1 from BLM (Cranston 2009) locates minable potash ore much closer to the C-2737 release point  
2 than in CRA-2004 PABC (see Figure TFIELD 6-5). This new shortened distance from the  
3 release point to the nearest minable potash (in the full-mining scenario) reverses the slowing-  
4 down trend observed in the CRA-2004 PABC analysis.

5 As in the CRA-2004 PABC calculations, a very weak positive correlation was found between the  
6 travel times and the random mining factor (the higher the random mining factor, the longer the  
7 particle travel time – see Figure TFIELD 6-19 and Figure TFIELD 6-20). As the mining factor is  
8 increased, the flow through the non-mining areas (including the C-2737 particle release location)  
9 is decreased, producing longer travel times and the positive correlation. Most of the advective  
10 particle travel time variability is due to differences in the base T-fields and their subsequent  
11 calibration, and not the random mining factor.

## 1 TFIELD-7.0 Summary

2 Observed Culebra transmissivities ( $T$ ) have been related to four deterministic factors: the  
3 thickness of overburden above the Culebra, the presence or absence of dissolution of the upper  
4 Salado, the presence of gypsum cements, and the presence or absence of halite in units above and  
5 below the Culebra. Culebra  $T$  is also related to the occurrence of open, interconnected fractures  
6 that cannot be mapped as easily as the other three factors and therefore must be treated  
7 stochastically. A linear-regression model for Culebra  $T$  has been developed based on these  
8 factors that provided an excellent match to the observed data, and can be tested through the  
9 collection of additional data. This model was used to create 1000 stochastic realizations of the  
10 distribution of Culebra  $T$  (base T-fields) in the vicinity of the WIPP site.

11 A MODFLOW-2000 modeling domain was defined extending 30.7 km north-south and 28.4 km  
12 east-west, roughly centered on the WIPP site. This domain was discretized into 87,188 uniform  
13 100-m square two-dimensional finite-difference cells. An inactive portion of the northwest  
14 corner of the domain is used to represent a no-flow boundary along the axis of Nash Draw. A  
15 low-permeability constant-head portion of the eastern section of the domain is used to represent  
16 the lithostatic pressure portion of the Culebra sandwiched above and below by Rustler halite  
17 units. Freshwater head observations in 42 monitoring wells from May 2007 were used as steady-  
18 state calibration targets. Drawdown observations in 62 observation wells, in response to 9 unique  
19 pumping tests, were used as transient calibration targets. A subset consisting of 100 of the 200  
20 calibrated Culebra model realizations were selected based on their ability to simulate these  
21 observed heads.

22 The EPA requires that the potential effects of future potash mining be taken into account when  
23 evaluating the performance of the WIPP disposal system. Accordingly,  $T$  in the areas within the  
24 model domain where current or future mining might affect the Culebra were scaled by a random  
25 multiplier between 1 and 1,000 obtained from Latin hypercube sampling. A single multiplier was  
26 used for each T-field, applied first to the areas outside the WIPP LWB that might be mined to  
27 create a partial-mining T-field, and then to all areas (both inside and outside the WIPP LWB) to  
28 create a full-mining T-field. Three statistically similar replicates of mining multipliers were  
29 generated, leading to a total of 600 unique T-fields (100 calibrated realizations, 2 mining  
30 scenarios, and 3 replicates). The MODFLOW-2000 flow budgets were used from each  
31 realization as input for both advective particle tracking (DTRKMF) summarized here and  
32 radionuclide solute transport (SECOTP2D) used in WIPP PA.

33 The non-mined travel times from the center of the WIPP waste panels to the WIPP LWB are  
34 similar to those computed for the CCA and therefore faster than those computed for CRA-2004  
35 PABC. The decrease in travel time to the LWB can be attributed to the presence of a consistent  
36 high-transmissivity pathway leaving the south-east portion of the LWB. The presence of this  
37 pathway is supported by observed drawdown data from the SNL-14 pumping test.

38 In the partial-mining case, particle tracks show increased travel times from the center of the  
39 WIPP waste panels to the WIPP LWB, compared to the non-mining scenario. In the full-mining  
40 case, particle tracks showed decreased travel times to the WIPP LWB, due to the close proximity  
41 of minable potash to the center of the WIPP waste panels.

## 1 **TFIELD-8.0 References**

2 (\*Indicates a reference that has not been previously submitted.)

3 Beauheim, R.L. 1987a. *Analysis of Pumping Tests of the Culebra Dolomite Conducted at the H-3 Hydropad at the Waste Isolation Pilot Plant (WIPP) Site*. Albuquerque, NM: Sandia National Laboratories. SAND86-2311.

6 Beauheim, R.L. 1987b. *Interpretation of the WIPP-13 Multipad Pumping Test of the Culebra Dolomite at the Waste Isolation Pilot Plant (WIPP) Site*. Albuquerque, NM: Sandia National Laboratories. SAND87-2456.

9 Beauheim, R.L. 1989. *Interpretation of H-11b4 Hydraulic Tests and the H-11 Multipad Pumping Test of the Culebra Dolomite at the Waste Isolation Pilot Plant (WIPP) Site*. Albuquerque, NM: Sandia National Laboratories. SAND89-0536.

12 Beauheim, R.L. 2007. *Diffusivity mapping of fracture interconnections*. In *Proceedings of the 2007 US EPA/NGWA Fractured Rock Conference*. Westerville, OH, 2007. National Ground Water Association.

15 Beauheim, R.L. 2008. *Analysis Plan for Evaluation and Recalibration of Culebra Transmissivity Fields AP-114, Revision 1*. Carlsbad, NM: Sandia National Laboratories.

17 Beauheim, R.L. 2009. *Changes to Culebra T-Field Calibration Procedures under AP-114 Task 7*. Carlsbad, NM: Sandia National Laboratories. ERMS 551437.

19 Beauheim, R.L. and R.M. Holt. 1990. *Geological and Hydrological Studies of Evaporites in the Northern Delaware Basins for the Waste Isolation Pilot Plant (WIPP)*. In D.W. Powers, R.M. Holt, R.L. Beauheim and N. Rempe, eds. Guidebook 14. Geological Society of America (Dallas Geological Society). pp.45-78.

23 Beauheim, R.L. and G.J. Ruskauff. 1998. *Analysis of Hydraulic Tests of the Culebra and Magenta Dolomites and Dewey Lake Redbeds Conducted at the Waste Isolation Pilot Plant Site*. Albuquerque, NM: Sandia National Laboratories. SAND98-0049.

26 Bertram, S.G. 1995. *Record of FEP Screening Work, FEP ID#NS-11: Subsidence Associated with Mining Inside or Outside the Controlled Area*. Carlsbad, NM: Sandia National Laboratories. ERMS 230761.

29 Bowman, D.O. and R.M. Roberts. 2008. *Analysis Report for AP-070, Analysis of Hydraulic Tests Performed in IMC-461, SNL-6, H-11b2, H-15, and C-2737*. Carlsbad, NM: Sandia National Laboratories. ERMS 539221.

32 Burgess, A., T. Doe, T. Lowenstein, and J.A. Thies. 2008. *Waste Isolation Pilot Plant Culebra Hydrogeology Conceptual Model Peer Review Final Report*. Carlsbad, NM: U.S. Department of Energy. ERMS 551513.

35 Chavez, M. 2006. *NP 19-1 Software Requirements, Revision 12*. Carlsbad, NM: Sandia National Laboratories.

1 Clayton, D.J., R.C. Camphouse, J.W. Garner, A.E. Ismail, T.B. Kirchner, K.L. Kuhlman, and  
2 M.B. Nemer. 2010. *Summary Report of the CRA-2009 Performance Assessment Baseline*  
3 *Calculation*. Carlsbad, NM: Sandia National Laboratories. ERMS 553039.

4 Cranston, C.C. 2009. *Minable Potash Ore*. Carlsbad, NM: Bureau of Land Management.  
5 ERMS 551120.

6 Currie, J.B. and S.O. Nwachukwu. 1974. *Evidence on incipient fracture porosity in reservoir*  
7 *rocks at depth*. *Bulletin of Canadian Petroleum Geology*. 22, pp.42-58.

8 Deutsch, C.V. and A.G. Journel. 1998. *GSLIB: Geostatistical Software Library and User's*  
9 *Guide*. 2nd ed. New York: Oxford University Press.

10 Doherty, J. 2000. *PEST Manual*. Brisbane, Australia: Watermark Numerical Computing.

11 Harbaugh, A.W., E.R. Banta, M.C. Hill, and M.G. McDonald 2000. MODFLOW 2000: *The*  
12 *U.S. Geological Survey Modular Ground-Water Model User Guide*. Reston, VA: U.S.  
13 Geological Survey. OFR 00-92.

14 Hart, D.B., R.L. Beauheim, and S.A. McKenna. 2009. *Analysis Report for Task 7 of AP-114:*  
15 *Calibration of Culebra Transmissivity Fields*. Carlsbad, NM: Sandia National Laboratories.  
16 ERMS 552391.

17 Hart, D.B., R.M. Holt, and S.A. McKenna. 2008. *Analysis Report for Task 5 of AP-114:*  
18 *Generation of Revised Base Transmissivity Fields*. Carlsbad, NM: Sandia National Laboratories.  
19 ERMS 549597.

20 Holt, R.M. 1997. *Conceptual Model for Transport Processes in the Culebra Dolomite Member*  
21 *of the Rustler Formation*. Albuquerque, NM: Sandia National Laboratories. SAND97-0194.

22 Holt, R.M., R.L. Beauheim, and D.W. Powers. 2005. Predicting fractured zones in the Culebra  
23 Dolomite. In B. Faybushenko, P.A. Witherspoon and J. Gale, eds. *Dynamics of Fluids and*  
24 *Transport in Fractured Rock*. American Geophysical Union. pp.103-16.

25 Holt, R.M. and D.W. Powers. 1988. *Facies variability and post-depositional alteration within*  
26 *the Rustler Formation in the vicinity of the Waste Isolation Pilot Plant*, southeastern New  
27 Mexico. Carlsbad, NM: Department of Energy. WIPP-DOE-88-004.

28 Holt, R.M. and L. Yarbrough. 2002. *Analysis Report, Task 2 of AP-088, Estimating Base*  
29 *Transmissivity Fields*. Carlsbad, NM: Sandia National Laboratories. ERMS 523889.

30 Johnson, P.B. 2009a. *Potentiometric Surface, Adjusted to Equivalent Freshwater Heads, of the*  
31 *Culebra Dolomite Member of the Rustler Formation near the WIPP Site, Revision 1*. Carlsbad,  
32 NM: Sandia National Laboratories. ERMS 548746.

1 Johnson, P.B. 2009b. *Routine Calculations Report In Support of Task 6 of AP-114: Potentiometric Surface, Adjusted to Equivalent Freshwater Heads, of the Culebra Dolomite member of the Rustler Formation near the WIPP Site, Revision 2*. Carlsbad, NM: Sandia National Laboratories. ERMS 551116.

5 Kirchner, T.B. 2010. *Generation of the LHS Samples for the AP-145 (PABC09) PA Calculations*. Carlsbad, NM: Sandia National Laboratories. ERMS 552905.

7 Kuhlman, K.L. 2009. *AP-144 Analysis Plan for the Calculation of Culebra Flow and Transport for CRA2009PABC*. Carlsbad, NM: Sandia National Laboratories. ERMS 551676.

9 Kuhlman, K.L. 2010. *Analysis Report for the CRA-2009 PABC Culebra Flow and Transport Calculations (AP-144)*. Carlsbad, NM: Sandia National Laboratories. ERMS 552951.

11 Leigh, C.D., J.F. Kanney, L.H. Brush, J.W. Garner, G.R. Kirkes, T. Lowry, M.B. Nemer, J.S. Stein, E.D. Vugrin, S. Wagner, and T.B. Kirchner. 2004. *2004 Compliance Recertification Application Performance Assessment Baseline Calculation, Revision 0*. Carlsbad, NM: Sandia National Laboratories. ERMS 541521.

15 Lowry, T.L. 2003a. Analysis Report, Task 5 of AP-088: Evaluation of Mining Scenarios. Carlsbad, NM: Sandia National Laboratories. ERMS 531138.

17 Lowry, T.L. 2003b. *Analysis Report, Tasks 2 & 3 of AP-100: Grid Size Conversion and Generation of SECOTP2D Input*. Carlsbad, NM: Sandia National Laboratories. ERMS 531137.

19 Lowry, T.S. 2004. *Analysis Report for Inclusion of Omitted Areas in Mining Transmissivity Calculations in Response to EPA Comment G-11*. Carlsbad, NM: Sandia National Laboratories. ERMS 538218.

22 Lowry, T.S. and J.F. Kanney. 2005. *Analysis Report for the CRA-2004 PABC Culebra Flow and Transport Calculations*. Carlsbad, NM: Sandia National Laboratories. ERMS 541508.

24 McKenna, S.A. and D.B. Hart. 2003. *Analysis report for Task 4 of AP-088: Conditioning of Base T Fields to Transient Heads*. Carlsbad, NM: Sandia National Laboratories. ERMS 531124.

26 McKenna, S.A. and A. Wahi. 2006. *Local Hydraulic Gradient Estimator Analysis of Long-Term Monitoring Networks*. *Ground Water*. 44(5), pp.723-31.

28 Mehl, S.W. 2001. MODFLOW-2000, *The US Geological Survey Modular Ground-Water Model User Guide to the Link-AMG (LMG) Package for Solving Matrix Equations using an Algebraic Multigrid Solver*. USGS (US Geological Survey). OFR 01-177.

31 Powers, D.W. 2002a. *Analysis report Task 1 of AP-088, Construction of geologic contour maps*. Carlsbad, NM: Sandia National Laboratories. ERMS 522085.

33 Powers, D.W. 2002b. *Addendum to Analysis Report, Task 1 of AP-088, Construction of Geologic Contour Maps*. Carlsbad, NM: Sandia National Laboratories. ERMS 523886.

1 Powers, D.W. 2003. *Addendum 2 to Analysis report Task 1 of AP-088, Construction of geologic*  
2 *contour maps*. Carlsbad, NM: Sandia National Laboratories. ERMS 522085.

3 Powers, D.W. 2006. *Analysis Report Task 1B of AP-114: Identify possible area of recharge to*  
4 *the Culebra west and south of WIPP*. Carlsbad, NM: Sandia National Laboratories. ERMS  
5 547094.

6 Powers, D.W. 2007a. *Analysis Report for Task 1A of AP-114: Refinement of Rustler Halite*  
7 *Margins Within the Culebra Modeling Domain*. Carlsbad, NM: Sandia National Laboratories.  
8 ERMS 547559.

9 Powers, D.W. 2007b. *Analysis Report for Task 1A of AP-114: refinement of Rustler Halite*  
10 *margins within the Culebra modeling domain*. Carlsbad, NM: Sandia National Laboratories.  
11 ERMS 547559.

12 Powers, D.W. 2009. *Basic Data Report for Drillhole SNL-8 (C-3150) (Waste Isolation Pilot*  
13 *Plant)*. DOE/WIPP 05-3324. Carlsbad, NM: U.S. Department of Energy.

14 Powers, D.W. and R.M. Holt. 1995. *Regional geological processes affecting Rustler*  
15 *hydrogeology. IT Corporation for Westinghouse Electric Corporation*.

16 Powers, D.W. and R.M. Holt. 1999. *The Los Medanos Member of the Permian Rustler*  
17 *Formation. New Mexico Geology*. 21(4), pp.97-103.

18 Powers, D.W. and R.M. Holt. 2000. *The salt that wasn't there: mudflat facies equivalents to*  
19 *halite of the Permian Rustler Formation, southeastern New Mexico*. *Journal of Sedimentary*  
20 *Research*, 70(1), pp.29-36.

21 Powers, D.W., R.M. Holt, R.L. Beauheim, and S.A. McKenna. 2003. *Geologic factors related*  
22 *to the transmissivity of the Culebra Dolomite Member, Permian Rustler Formation, Delaware*  
23 *Basin, southeastern New Mexico*. In K.S. Johnson and J.T. Neal, eds. *Evaporite Karst and*  
24 *engineering/environmental problems in the United States*. 109th ed. Oklahoma Geological  
25 Survey. pp.211-18.

26 Powers, D.W., R.M. Holt, R.L. Beauheim, and R.G. Richardson. 2006. *Advances in*  
27 *depositional models of the Permian Rustler Formation, southeastern New Mexico*. In *Caves &*  
28 *Karst of Southeastern New Mexico*. Fifty-seventh Annual Field Conference Guidebook ed. NM  
29 Geological Society. pp.267-76.

30 Powers, D.W. and D. Owsley. 2003. *A field survey of evaporite karst along NM 128*  
31 *realignment routes*. In K.S. Johnson and J.T. Neal, eds. *Evaporite karst and engineering /*  
32 *environmental problems in the United States*. 109th ed. Oklahoma Geological Survey. pp.233-  
33 40.

34 Ramsey, J.L. and M. Wallace. 1996. *Analysis Package for the Culebra Flow and Transport*  
35 *Calculations (Task 3) of the Performance Assessment Analyses Supporting the Compliance*  
36 *Certification Application*. Carlsbad, NM: Sandia National Laboratories. ERMS 240516.

1    Roberts, R.M. 2006. *Analysis Report for AP-070, Analysis of Culebra Pumping Tests*  
2    *Performed Between December 2003 and August 2005*. Carlsbad, NM: Sandia National  
3    Laboratories. ERMS 543901.

4    Roberts, R.M. 2007. *Analysis Report for AP-070, Analysis of Culebra Hydraulic Tests*  
5    *Performed Between June 2006 and September 2007*. Carlsbad, NM: Sandia National  
6    Laboratories. ERMS 547418.

7    Rudeen, D.K. 2003. *User's Manual for DTRKMF Version 1.00*. Carlsbad, NM: Sandia National  
8    Laboratories. ERMS 523246.

9    Toll, N.J. and P.B. Johnson. 2006a. *Routine Calculations Report In Support of Task 6 of AP-*  
10   *114, SNL-14 August 2005 Pumping Test Observation Well Data Processing, Summary of Files*.  
11   Carlsbad, NM: Sandia National Laboratories. ERMS 543371.

12   Toll, N.J. and P.B. Johnson. 2006b. *Routine Calculations Report In Support of Task 6 of AP-*  
13   *114, WIPP-11 February 2005 Pumping Test Observation Well Data Processing - Summary of*  
14   *Files*. Carlsbad, NM: Sandia National Laboratories. ERMS 543651.

15   U.S. Department of Energy (DOE). 1996. *Title 40 CFR Part 191 Compliance Certification*  
16   *Application for the Waste Isolation Pilot*. Carlsbad, NM: U.S. Department of Energy Waste  
17   Isolation Pilot Plant, Carlsbad Area Office. DOE/CAO-1996-2184.

18   U.S. Department of Energy (DOE). 2004. *Title 40 CFR Part 191 Subparts B and C Compliance*  
19   *Recertification Application for the Waste Isolation Pilot Plant*. Carlsbad, NM: US Department of  
20   Energy Carlsbad Field Office. DOE/WIPP 2004-3231.

21   U.S. Department of Energy (DOE). 2009. *Title 40 CFR Part 191 Subparts B and C Compliance*  
22   *Recertification Application for the Waste Isolation Pilot Plant*. Carlsbad, NM: US Department of  
23   Energy Carlsbad Field Office. DOE/WIPP 2009-3424.\*

24   U.S. Environmental Protection Agency (EPA). 1996. *40 CFR Part 194: Criteria for the*  
25   *Certification and Recertification of the Waste Isolation Pilot Plant's Compliance with 40 CFR*  
26   *Part 191 Disposal Regulations; Final Rule.*, 1996. Federal Register Vol 61, 5223-5245.